Progress in Oceanography 199 (2021) 102697

Contents lists available at ScienceDirect

Progress in Oceanography

journal homepage: www.elsevier.com/locate/pocean

Advective pathways and transit times of the Red Sea Overflow Water in the Arabian Sea from Lagrangian simulations

Viviane V. Menezes

Woods Hole Oceanographic Institution, Department of Physical Oceanography, Woods Hole, MA, United States of America

ARTICLE INFO

Keywords:
Salinity
Northwest Indian Ocean
Parcels toolbox
Trajectories
Oxygen
Particles

ABSTRACT

The present study investigates the advective pathways and transit times of virtual particles released in the Red Sea outflow area as a proxy for the poorly understood spreading of the Red Sea Overflow Water (RSOW) in the Arabian Sea. This work uses the Parcels toolbox, a Lagrangian framework, to simulate tens of thousands of trajectories under different initial conditions. Six different Lagrangian simulations are performed at isobaric and isopycnal surfaces within the RSOW layer. All simulations are based on the eddy-rich GLORYS12 reanalysis that merges almost all in-situ (temperature–salinity) and satellite observations collected over the last two decades into a dynamical framework. This study shows that GLORYS12 reproduces relatively well the climatological seasonal cycle of the RSOW to the Gulf of Aden and essential characteristics of the exchange at the Strait of Bab al-Mandab. Statistical comparisons between synthetic trajectories and RAFOS floats in the Gulf of Aden corroborate the quality of GLORYS12 velocity fields used for the Lagrangian simulations. Six main advective pathways are uncovered (by order of preference): Southwest, Northwest, Socotra Passage, Central, Eastern, and Southern. Trajectories from Argo floats give observational support for some of these paths. Although most particles are exported out of the Arabian Sea off Somalia, the simulations reveal robust connectivity of the RSOW to the Arabian Sea interior and its eastern boundary. The fact that particles have long trajectories in the interior increases the potential of RSOW mixing with the fresher and oxygen-poor ambient waters. Thus, these pathways may have profound implications for the salt and oxygen budgets in the Arabian Sea and beyond since the RSOW is also part of the global overturning circulation and exported out of the Indian Ocean via the Agulhas Current. Transit time distributions indicate that it takes about six months for outflow-originated particles to spread over the entire Gulf of Aden and one to three years to be exported along the western boundary, toward Somalia (Socotra Passage and Southwest pathways) and off the Yemeni–Omani coast (Northwest Pathway). In contrast, reaching the eastern boundary takes much longer. North of 14° N, the most frequent time is around 10–15 years, and about 20–25 years at the southeastern Arabian Sea. Hence, the RSOW can often carry oxygen to the western boundary but not to the eastern basin. This may contribute to the eastern shift of the Arabian Sea Oxygen Minimum Zone, a subject that deserves investigation.

1. Introduction

The Red Sea Water or Red Sea Overflow Water (RSOW) is one of the most important sources of salt for the oceanic intermediate layer (e.g., Beal et al., 2000; Clowes and Deacon, 1935; Han and McCreary, 2001; Rochford, 1964; Wyrtki, 1971) and a source of oxygen for the oxygen-poor Arabian Sea, although the importance of the latter is still under debate (e.g., Beal et al., 2000; Fine et al., 2008; McCreary et al., 2013; Olson et al., 1993; Premchand et al., 1986; Sarma, 2002; Schmidt et al., 2020; Wyrtki, 1971). This highly saline water, with salinity around 40, enters the Gulf of Aden through the shallow (sill depth of 137 m) and narrow (minimum width of about 25 km) Strait of Bab al-Mandab (Fig. 1) (Bower et al., 2000, 2005; Murray and Johns, 1997). The Red Sea outflow transport has a pronounced seasonal cycle associated with the monsoonal wind regime, with minimum transport in summer (≈0.05 Sv) and maximum (≈0.7 Sv) in winter (Murray and Johns, 1997)— hereafter, boreal seasons.

In the Gulf of Aden, the RSOW mixes with fresher ambient waters, diluting by a factor of about 2.5 and reaching neutrally buoyant depths of 400–800 m (Bower et al., 2000, 2005). In the Gulf, the main equilibrated RSOW has salinity around 37.5 and temperature of 17.9 °C, with the salinity maximum centered at the isopycnal (σ_θ) of 27.2 kg/m^3 (Bower et al., 2000). A secondary equilibrium level occurs at a deeper isopycnic (27.6σ_θ, 1000–1200 m), with similar salinity but cooler temperatures (Bower et al., 2005). The multiple equilibrium

---

E-mail address: vmenezes@whoi.edu.

https://doi.org/10.1016/j.pocean.2021.102697
Received 16 December 2020; Received in revised form 16 August 2021; Accepted 17 October 2021

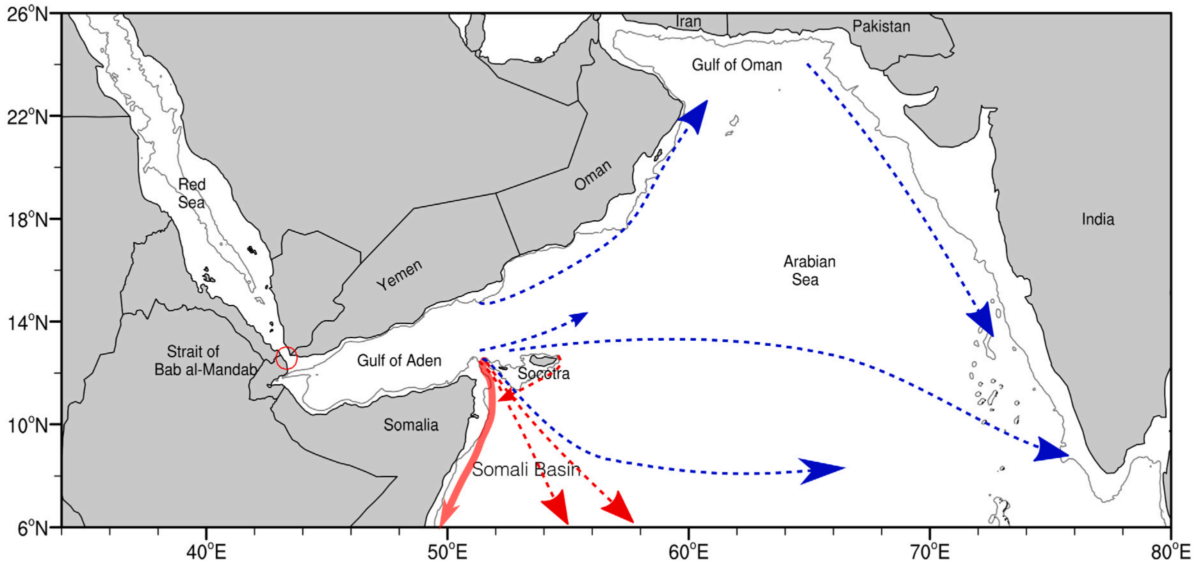

Fig. 1. Potential RSOW pathways in the Arabian Sea from the literature. The only widely accepted pathway shown in the map is the southward path hugging the Somali continental slope in the western boundary. Red is used for potential pathways advecting RSOW southward in the western Arabian Sea, and blue to pathways that advect water toward the east or along the eastern boundary. The gray contour is the 700 m isobath from 2-minute gridded global relief data (ETOPO2) version 2 (NGDC, 2006). (For interpretation of the references to color in this figure legend, the reader is referred to the web version of this article.)

levels are likely due to different mixing histories (by turbulent entrainment) along the two bathymetric channels where the RSOW descent into the Gulf of Aden (Bower et al., 2005, and references therein).

The dilute RSOW (salinity around 36) is then exported from the Gulf of Aden to the Arabian Sea at mid-depths (500–1500 m), forming a subsurface salinity maximum in the open ocean (Beal et al., 2000; Premchand et al., 1986; Rochford, 1964; You, 1998; Wyrtki, 1971). Predominantly, the RSOW spreads within the isopycnal layer of 27–27.6 kg/m^3 over a distance of several thousand kilometers in the Arabian Sea and beyond (Beal et al., 2000; L'Hégaret et al., 2021).

Despite the potential impacts on the Arabian Sea salt and oxygen budgets, the RSOW advective spreading pathways and transit times are still mostly unknown in the northwest Indian Ocean (e.g., L'Hégaret et al., 2021; McCreary et al., 2013; Schmidt et al., 2020). In the Gulf of Aden, deep-reaching mesoscale eddies dominate the RSOW spreading pathways (Bower and Furey, 2012), but in the Arabian Sea, the picture is fragmented and often conflicting, as described below.

1.1. *The obscure RSOW spreading in the Arabian Sea*

In situ observations indicate that the preferred spreading route is along the western boundary off Somalia (Beal et al., 2000, 2003; Bruce and Volkmann, 1969; Chowdary et al., 2005; Clowes and Deacon, 1935; de Marez et al., 2019; Fischer et al., 1996; Gamsakhurdiya et al., 1991; Premchand et al., 1986; Quadfasel and Schott, 1982, 1983; Rochford, 1964; Shapiro and Meschanov, 1991; Schott and Fischer, 2000; Schott and McCreary, 2001; Stramma et al., 2002; Swallow and Bruce, 1966; Warren et al., 1966; You, 1998). Wintertime measurements by Schott and Fischer (2000) show a relatively strong southwestward undercurrent (400–1000 m; about 30 cm/s) that advects the RSOW from the Gulf of Aden via the Socotra Passage (Guardafui Channel) located between the Africa mainland and Socotra island (Fig. 1). This undercurrent lies beneath a shallow branch of the Somali Current that flows northeastward after bifurcating near the continental slope around 8°–10° N (Schott and Fischer, 2000; Stramma et al., 2002; Schott and McCreary, 2001). In winter, the Socotra Undercurrent connects to the coastal Somali Undercurrent, which advects RSOW further south (Bruce and Volkmann, 1969; Esenkov and Olson, 2002; Quadfasel and Schott, 1983; Schott and Fischer, 2000; Schott and McCreary, 2001; Warren et al., 1966). Schott and Fischer (2000) conjecture that the Socotra Passage is the main route to the RSOW export out of the Gulf of Aden because, in winter, the Red Sea outflow transport is maximum, and the undercurrents are predominantly southward.

Because the monsoonal regime also affects the mid-depth circulation in the Arabian Sea, with undercurrents reversing seasonally (Schott and McCreary, 2001), it has been speculated that the (south-oriented) RSOW tongue along the Somali slope is likely a wintertime feature (e.g. Beal et al., 2000; Gamsakhurdiya et al., 1991). The tongue would be weak in summer when undercurrents are mostly northward with the development of the deep-reaching anticyclonic Great Whirl (Beal and Donohue, 2013; Esenkov and Olson, 2002; Fischer et al., 1996). However, there is an indication that the RSOW tongue is present offshore Somalia in summer but north-oriented (Quadfasel and Schott, 1982). In summer, rather than in the Socotra Passage, RSOW signature was measured east of the island, underneath the Socotra Gyre (Fischer et al., 1996). This route may be another path out of the Gulf of Aden. More recent measurements from an Argo float in the same region (Carton et al., 2012) offer additional support for the route east of Socotra.

After crossing the Socotra Passage, the RSOW pathway may split into multiple branches in the Somali Basin (Fig. 1). Besides the branch hugging the Somali slope, another one, farther offshore, appears in the diagrams of Rochford (1964) and Shapiro and Meschanov (1991). However, in situ observations supporting this offshore (southward) branch are contradictory. For instance, wintertime measurements from Schott and Fischer (2000) south of the Socotra near 53° E do not show it but this offshore branch appears in the measurements from Warren et al. (1966) and Fischer et al. (1996) (also around 53° E but summer). A third branch, also originating in the Somali Basin, would advect the RSOW across the Arabian Sea toward India in summer (Gamsakhurdiya et al., 1991; Shapiro and Meschanov, 1991). Rochford (1964) also described a possible cross-basin pathway but slightly northward than the ones from Gamsakhurdiya et al. (1991) and Shapiro and Meschanov (1991). Rochford's cross-basin path would connect the north of Socotra to India's southern tip (compare the dashed blue paths south of 14° N in Fig. 1). Despite these early descriptions, Beal et al. (2000) did not find conclusive evidence for an eastward pathway, although summertime hydrographic measurements from Beal et al. (2003) and He et al. (2020) show patches of RSOW at 8° N near 60° E and 73° E and Chowdary et al. (2005) describe RSOW between 12°–16° N and 63°–71° E based on Argo floats. This evidence suggests an eastward export of RSOW to the Arabian Sea interior. The occurrence of isolated patches or lenses of RSOW (sometimes referred to as Reddies), especially in the central Arabian Sea, seems common. The mechanisms sustaining these patches in the Arabian Sea are not clear to date (Beal et al., 2000; de Marez et al., 2020; Gamsakhurdiya et al., 1991; Meschanov and Shapiro, 1998; Shapiro and Meschanov, 1991; Shapiro et al., 1994) although submesoscale dynamics may play a significant role in their formation in the Gulf of Aden (e.g., Morvan et al., 2020).

In addition to the pathways east and west of Socotra, another export route for the RSOW is likely the mouth of the Gulf of Aden, although its importance is still uncertain. Several observational studies show the RSOW high-saline fingerprint at intermediate depths in this region (Al Saafani and Shenoi, 2007; Beal et al., 2000; Carton et al., 2012; de Marez et al., 2019, 2020; Premchand et al., 1986; Sastry and D'Souza, 1972; Schott and Fischer, 2000; Shapiro and Meschanov, 1991; Rochford, 1964; Warren et al., 1966). However, Schott and Fischer (2000) suggest the RSOW export via the Gulf's mouth is occasional, and Shapiro and Meschanov (1991) find it hard to trace this route north of 17°–18° N based solely on salinity observations. Along these lines, some studies argue that the RSOW would not spread north of 17°–18° N, although historical observations are scarce in this region (Chowdary et al., 2005; Premchand et al., 1986; Rochford, 1964; Sastry and D'Souza, 1972; Shenoi et al., 1993; Varma et al., 1980). Based on the much more extensive Argo dataset, L'Hégaret et al. (2021) also rarely detected RSOW signal north of 20° N, perhaps because the RSOW loses its signature along the way due to isopycnal mixing with fresher Arabian Sea waters. Recently, Schmidt et al. (2020) performed a set of Lagrangian particle tracking simulations by advecting virtual particles into a high-resolution numerical model that assimilates in situ and satellite observations. The aim was to investigate the ventilation of the Arabian Sea Oxygen Minimum Zone (ASOMZ) located in the northeastern Arabian Sea (300–1000 m). In contrast with the salinity-based identification, the simulations revealed a pronounced northeastward RSOW pathway along the Yemeni–Omani slope as farther as 22°–24° N (Fig. 1), with a high probability of RSOW reaching the western coast of India.

Despite the pathway toward the east being unknown, several studies (Babu et al., 1980; Beal et al., 2003; Shankar et al., 2005; Shenoi et al., 2005; Varkey et al., 1979; Vimal Kumar et al., 2008; You, 1998) describe the RSOW fingerprint in the eastern boundary, hugging the Indian slope, with signal decaying offshore and decreasing equatorward. Based on the observational pattern, which seems to indicate advection from north to south, Shankar et al. (2005) propose two possible pathways for RSOW to arrive in the eastern boundary (Fig. 1). One possibility would be northward along the Yemeni–Omani slope, then westward along the slope off Iran and Pakistan, and southward off India's west coast, similar to the pathway found by Schmidt et al. (2020) for the RSOW to ventilate the ASOMZ. Another possibility would be a deep, open-ocean, cross-basin flow connecting the western Arabian Sea to the northern portion of the Indian slope.

1.2. Lagrangian Approach

Traditionally, the RSOW spreading has been investigated based on in situ observations by tracing its salty/spicy signature (e.g., Beal et al., 2000; L'Hégaret et al., 2021). Unfortunately, in situ observations are not homogeneous in time and space over the entire Arabian Sea, which may explain why a clear picture of the RSOW spreading pattern is still missing. Here, a different approach is employed. The present study uses Lagrangian particle tracking simulations to investigate the preferred advective pathways and transit times of the RSOW spreading in the Arabian Sea. In this approach, large sets of virtual passive particles are integrated in time within three-dimensional, time-evolving velocity fields commonly from Ocean General Circulation Models (OGCMs) (van Sebille et al., 2018).

A growing number of studies have been using this technique to study pathways, timescales, and connectivity between oceanic regions, as recently reviewed by van Sebille et al. (2018). For instance, Durgadoo et al. (2017) investigated the water mass sources for the Agulhas Current (that include the RSOW) using Lagrangian simulations, Schmidt et al. (2020) used it to study the ASOMZ ventilation, and Sheehan et al. (2020) to characterize the Persian Gulf Water route from the Gulf of Oman to the Bay of Bengal.

Lagrangian simulations have also been widely used to study pathways of other overflow waters around the globe, for example, the Iceland–Scotland Overflow Water (Zou et al., 2017, 2020), Mediterranean Overflow Water (Burkholder and Lozier, 2011), Denmark Strait Overflow Water (Saberi et al., 2020), and overflow waters of subpolar origin in the North Atlantic (Lozier et al., 2012), to cite a few studies. In none of these Lagrangian studies, the underlying OGCMs (with horizontal resolutions between 1/12° and 1/10°) resolve overflow dynamics whose processes (e.g., mixing driven by frictional processes at the bottom boundary layer, entrainment of ambient water, hydraulic control at narrow straits and sills) occur at scales much smaller than the model grid-scale (Colombo et al., 2020; Fox-Kemper et al., 2019; Ilicak et al., 2008; Legg et al., 2009). The overflows are rather parameterized in OGCMs. Legg et al. (2009) give a nice overview of the challenges involved in these parametrizations for readers interested in this subject.

A common issue is that the modeled overflow waters do not have the same spiciness/density as in nature (e.g., Colombo et al., 2020; Marzocchi et al., 2015; Zou et al., 2020), especially in OGCMs that use z-level vertical coordinate schemes (Colombo et al., 2020; Legg et al., 2009). Despite the limitations, the Lagrangian trajectories simulated from such OGCMS can be useful for understanding the overflow waters spreading pattern in basin-scale, which is not feasible based on sparse observational records alone. This approach is strongly increasing the understanding of the North Atlantic overflow waters pathways (e.g., Zou et al., 2020), but has not been explored in the case of RSOW spreading in the Arabian Sea and its path to the east yet.

1.3. This study

In the present study, the Lagrangian simulations are based on the state-of-art and high spatial resolution (1/12°) Mercator Global Ocean Reanalysis (GLORYS12) version 1 (GLOBAL_REANALYSIS_PHY_001_030) (Fernandez and Lellouche, 2018; Lellouche et al., 2018) distributed by the Copernicus Marine Environment Monitoring Service (CMEMS). GLORYS12 compiles most satellite and in-situ observations collected in the Arabian Sea in the last 25-years, including Argo floats. GLORYS12 suffers from the same issues as the above-cited models in terms of overflow water mass properties as later described but has the advantage of being constrained by observations, especially Argo floats and satellite altimetry sea surface height (SSH) data. The assimilation of SSH data improves the representation of mesoscale eddies in GLORYS12, which is essential for the RSOW spreading pathways in the Gulf of Aden (e.g., Bower and Furey, 2012).

In the Lagrangian simulations, the virtual particles were released in the Red Sea outflow region at the RSOW layer as a proxy indicator for the RSOW. A series of experiments of differing complexity were performed to characterize the RSOW preferred pathways and transit times quantitatively. Experiments were designed to identify the typical RSOW pathways in a climatological sense, evaluate how the eddy field impacts the probability distributions (and time scales) and the effects of the intermediate circulation seasonal variability.

The paper begins by presenting GLORYS12 climatological (Eulerian) fields to assure the readers that despite the overflow parametrization, GLORYS12 reproduces typical characteristics of RSOW in the Gulf of Aden as described in the literature. Then, a comparison between Lagrangian simulations based on GLORYS12 and trajectories from RAFOS (SOund Fixing And Ranging spelled backward) floats from the Red Sea Outflow Experiment (REDSOX) in the Gulf of Aden are presented (Bower and Furey, 2012; Furey et al., 2005). This comparison aimed to evaluate the statistical skill of GLORYS12 in reproducing the mid-depth circulation. Last, Argo trajectories are presented as observational support for some RSOW pathways identified in the Lagrangian simulations.

1.4. Manuscript organization

The paper is organized as follows: Sections 2 and 3 describe the datasets and the particle tracking Lagrangian experiments, respectively; Section 4.1 takes a brief look at how GLORYS12 reanalysis represents typical climatological characteristics of the RSOW in the Gulf of Aden; Section 4.2 presents an evaluation of GLORYS12 synthetic trajectories and temperature and salinity (T–S) properties against in situ observation from the REDSOX experiment. Section 4.3 examines the probabilities of particle positions in the Arabian Sea, the RSOW spreading and transit times; Section 4.4 investigates the connectivity, preferred pathways, and salinity dilution, and Section 4.5 offers observational evidence from Argo trajectories. Section 5 discusses the preferred advective pathways in light of the occurrence of RSOW reported in the literature. Section 6 provides a summary and conclusion.

2. Data

2.1. GLORYS12 reanalysis

Daily-average fields of zonal (u) and meridional (v) velocities, (potential) temperature, and (practical) salinity from the eddy-rich GLORYS12 version 1 (Drévillon et al., 2018; Fernandez and Lellouche, 2018; Lellouche et al., 2018) were used for the Lagrangian simulations: Velocity fields for computing particle positions and temperature–salinity fields to determine the water properties along the trajectories as described in Section 3.1.

GLORYS12 spans the satellite altimetry era (Jan-1993 to the present), with occasional updates. In this study, the GLORYS12 fields span from 1-Jan-1993 to 25-Dec-2018. The fields have horizontal grid resolution of $1/12^\circ \times 1/12^\circ$ (approximately 8 km in the Arabian Sea) in 50 unevenly-spaced vertical levels (z-coordinates) from the sea surface to the seafloor. Vertical resolution decreases from the mixed layer (22 levels in the upper 100 m, spaced by 1–2 m) to the abyssal oceans ($\approx$ 450 m) (Lellouche et al., 2018). The GLORYS12 fields are interpolated from the native Arakawa C-grid to an A-grid before public availability. In the RSOW layer within the Arabian Sea, the vertical resolution is around 100 m (541.1 m, 643.6 m, and 763.3 m).

GLORYS12 is based on the LIM2/NEMO 3.1 machinery (Louvain-la-Neuve Sea Ice Model/Nucleus for European Modeling of the Ocean). The oceanic component is forced by the European Centre for Medium-Range Weather Forecasts (ERA)-Interim atmospheric reanalysis, with correction for precipitation and radiative fluxes. The initial oceanic conditions are derived from the Met Office Hadley Centre database (EN.4.2.0). Internal-tide-driven mixing is parameterized, as the oceanic component does not explicitly represent tides (Lellouche et al., 2018). At Gibraltar and Bab al-Mandab straits, a relaxation toward the EN.4.2.0 decadal climatology is applied to minimize spurious mixing (i.e., excessive and non-physical) over topographic constraints (Drévillon et al., 2018; Lellouche et al., 2018), which is a common issue in OGCMs using z-coordinates such as NEMO (Colombo et al., 2020; Legg et al., 2009). The relaxation toward the climatology is centered at 12° N–46° E and applied only below 500 m with relaxation terms increasing linearly between 500 and 700 m and then constant toward the seafloor. The time scale is 50 days, with time increasing to infinity 5° away from the area center (Lellouche et al., 2018).

GLORYS12 is constrained by along-track SSH from multiple satellite altimetry missions, satellite-based sea surface temperature (SST) from AVHRR sensors (Advanced Very High-Resolution Radiometer), in situ vertical profiles of temperature and salinity from the CORA (Coriolis Ocean Dataset for Reanalysis) dataset version 5.1 (which includes Argo floats and CTD (Conductivity–Temperature–Depth) observations), and sea ice concentration. Ocean bottom topography is from ETOPO1 (1-arcmin global relief model) for the deep ocean, with GEBCO8 (General Bathymetric Chart of the Oceans) used for coastal areas and continental shelves. Observations are assimilated using a three-dimensional variational (3D-VAR) approach, with correction for the slowly-evolving large-scale biases in temperature and salinity (Artana et al., 2019; Drévillon et al., 2018; Fernandez and Lellouche, 2018). Drévillon et al. (2018) describe the many improvements implemented in GLORYS12 components for readers interested in this subject as well as a global assessment of the GLORYS12 performance against in-situ and satellite observations. The latter authors show that in the Arabian Sea at 800 m depth (RSOW layer), the mean salinity difference to the WOA13 (World Ocean Atlas 2013) is ± 0.05. In the Arabian Sea, data from this reanalysis have also been recently analyzed by Sheehan et al. (2020) and de Marez et al. (2020).

Because RSOW spreads along isopycnals (27–27.6 kg/m^3) (e.g., Beal et al., 2000; L'Hégaret et al., 2021), several experiments described in Section 3.1 were performed on isopycnal surfaces. To generate the appropriate Eulerian fields for running these simulations, potential density anomaly fields referenced to the sea surface were first calculated from potential temperature and practical salinity using the Gibbs-SeaWater (GSW) Oceanographic Toolbox (IOC et al., 2010; McDougall and Barker, 2011). Then, the GLORYS12 daily fields were mapped from the original z-coordinates to σ_θ-coordinates (with a vertical resolution of 0.1 kg/m^3) using linear interpolation.

Additionally, for comparison with temperature from the RAFOS floats described below, the GLORYS12 potential temperature was converted to in situ temperature using the GLORYS12 salinity fields and the GSW toolbox. GSW was also used to convert to conservative temperature and absolute salinity when appropriate.

2.2. REDSOX experiment

For evaluating the particle tracking simulations based on GLORYS12, in situ Lagrangian observations of temperature, pressure, position, zonal, and meridional velocities obtained from 49 acoustically tracked isobaric RAFOS floats in the Gulf of Aden were used (Fig. 2a). GLORYS12 did not assimilate these observations.

The RAFOS system is composed of neutrally buoyant subsurface floats equipped with hydrophones that listen for timed acoustic signals transmitted by moored sound sources. These acoustic signals are used to determine the float position (by triangulation) at each time step (Rossby et al., 1986). To calculate positions, the float needs to listen from at least two different sound sources. As described in Rossby et al. (1986), the position determination depends on sound source power level, ambient noise, and acoustic propagation considerations such as the depth of the float in relation to the sound source channel axis. Unlike an Argo, a RAFOS is not a vertical profiler float and stays submerged at a pre-defined pressure (or density surface) for the whole mission length. At the end of its mission, the float drops its weight and rises to the sea surface to transmit all stored data via satellite.

The floats used here belong to the REDSOX experiment that took place between February 2001 and March 2003 (Furey et al., 2005). For tracking the floats, Furey et al. (2005) deployed four sound source moorings in the first of the two project cruises (REDSOX-1; 5-Feb to 15-Mar 2001). Three of these moorings were deployed in the western Gulf and one in the eastern. An additional sound source mooring was added to the east in the second cruise (REDSOX-2; 21-Aug to 12-Sep 2001). Sound sources used in the REDSOX had a higher frequency (780 Hz) than the ones used in open-ocean applications (260 Hz) (Furey et al., 2005). Thus, they had a much lower range since low-frequency sound waves travel further than high-frequency waves. The combination of fewer sound sources in the eastern (the second was deployed about 6-months later) and the lower range of the REDSOX sound sources

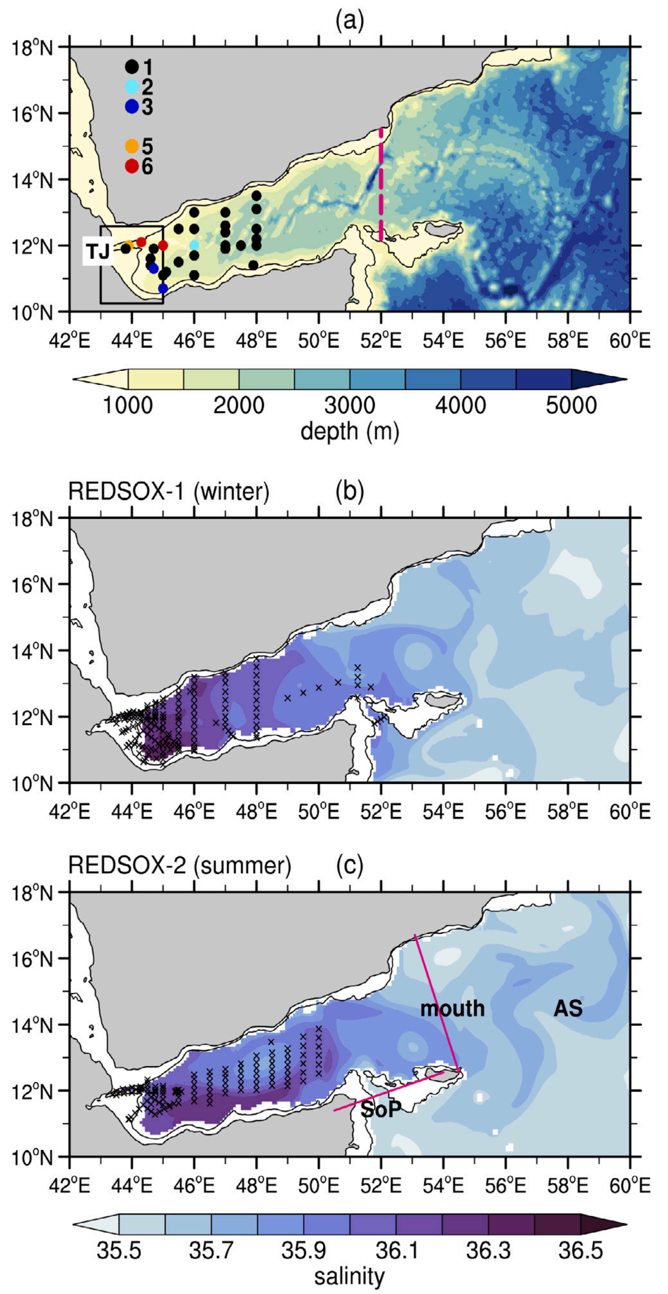

Fig. 2. REDSOX Experiment. (a) Location and number of RAFOS deployments between 2001 and 2003. Dot's color indicates the number of floats released in the respective position. Color shading shows the ETOPO2 bottom topography, the pink dashed line, the maximum range of sound sources, and the black box (10° N–12.6° N; 43° E–45° E) the region where virtual particles were released in the EXP-RSOW experiments. TJ stands for Tadjoura Rift (about 12° N; 43° E). (b) and (c) show the CTD stations during the REDSOX-1 campaign in winter (17-Feb to 12-Mar-2001) and REDSOX-2 in summer (21-Aug to 12-Sep-2001), respectively. Blue–Purple shading indicates the GLORYS12 Eulerian mean salinity fields over the respective cruise periods at 763 m. SoP stands for Socotra Passage between Africa and the Socotra island and AS to the Arabian Sea. The black contours in the maps are the 700 m isobath. (For interpretation of the references to color in this figure legend, the reader is referred to the web version of this article.)

made float tracking in the eastern Gulf much more difficult than in the western. In consequence, the maximum longitude for trajectories was 50° E–52° E. Also, it was impossible to track any float in the Socotra Passage because the acoustical signals transmitted by the sources could not reach so far. Nevertheless, Furey et al. (2005) and Bower and Furey (2012) show that eight floats (16.3% of the total) from the REDSOX experiment reached the Arabian Sea (east of 52° E). Two of these floats resurfaced (to transmit the data) in the Somali Basin around 8° N-52° E and six to the northeast, along the Yemeni coast, although by unknown pathways (Furey et al., 2005; Bower and Furey, 2012).

Although isobaric floats drift approximately at the same pressure level as they are released, small vertical displacements may happen in regions of strong horizontal density gradients (Lankhorst and Zenk, 2006), which also happened in REDSOX as described in Furey et al. (2005). The RAFOS dataset used here has been extensively analyzed by Bower et al. (2005), Bower and Furey (2012) and Furey et al. (2005), and the readers are referred to those papers and report for further information about REDSOX data.

The floats recorded pressure and temperature data twice a day and position fix every six hours. No salinity observations were collected. Each float was tracked for one year (Bower and Furey, 2012; Furey et al., 2005). At the end of the respective one-year mission, each float rose to the sea surface and transmitted the entire record via Argos satellite system (Furey et al., 2005; Wooding et al., 2005). The floats were ballasted for 650 dbar but were, on average, 73.7 dbar heavier than planned (Furey et al., 2005). Thus, they drifted with currents around 724 dbar. The closest GLORYS12 vertical level is at 763 m.

Most floats (34) were released during the two REDSOX cruises. The rest of the floats were initially anchored to the seafloor and released every 2-months. Fig. 2a shows the number of RAFOS deployments at each location.

Besides the RAFOS-derived observations, GLORYS12 was also compared against the CTD observations collected during the REDSOX cruises (Figs. 2b and 2c, respectively). These observations were analyzed by Bower et al. (2002), Bower et al. (2005), and Bower and Furey (2012). During the winter REDSOX-1 cruise, 163 CTD stations were occupied in the Gulf of Aden and 123 in the REDSOX-2. Vertical profiles of conservative temperature, σ_θ, and absolute salinity were derived for each station from in situ temperature, practical salinity, and pressure measurements using the GSW toolbox. For comparison between GLORYS12 and CTD observations, the reanalysis fields were bi-linearly interpolated to the station positions, and the CTD profiles (linearly) interpolated from the original 1-m resolution to the model vertical levels. These CTD observations have not been assimilated in GLORYS12 as they are not part of CORA.

2.3. *Ancillary data*

In addition to the RAFOS floats described above, trajectories derived from Argo floats were used as ancillary data. Unlike RAFOS, Argo floats drift at a programmed parking depth over days and ascend to the sea surface at the end of the drifting cycle to measure vertical profiles of temperature, salinity, and pressure. Argo can be considered as a semi-Lagrangian float. In Argo, positions are obtained from satellites (no acoustical tracking) when the float is at the surface. Depending on the satellite system used (e.g., Argos), a float may need to stay for a few hours at the surface to transmit the collected data. Because of that, there is potential contamination of deep velocities estimated from such trajectories, an issue nonexistent in RAFOS floats that stay submerged at a pressure or density level over the entire mission period. Also, positions along the Argo trajectories are obtained every few days — exact number depends on how the floats are programmed, but the standard cycle is ten days. Thus, the Argo trajectories have much lower resolution than RAFOS.

The number of Argo floats deployed in the Arabian Sea since 2002 is relatively small, especially in the western basin. In the CORIOLIS Argo global database (http://www.coriolis.eu.org/), there are 307 floats in the region between 8° *N*–26° *N* and 42° E-80° *N* (mostly with parking depths between 900–1200 m). However, only 263 floats have trajectories of more than 100-days of data, which is the subset used here. Thirty-two of these floats were launched inside the Gulf of Aden, and several of these have been individually analyzed by, e.g., Carton et al. (2012).

For readers interested on the Argo space–time distribution, L'Hégaret et al. (2021) and de Marez et al. (2019) present a detailed description for the Arabian Sea. While the Argo vertical temperature and salinity profiles were assimilated in GLORYS12, their trajectories were not.

3. Methods

3.1. Lagrangian particle tracking simulations

The present study used Parcels (Probably A Really Computationally Efficient Lagrangian Simulator) (Delandmeter and van Sebille, 2019; Lange and van Sebille, 2017) to perform the particle tracking simulations. Briefly, virtual (passive) particles were released in a set of initial positions at time t and integrated forward in time using the following equation for each particle i:

$$\mathbf{X}_i(t+\Delta t) = \mathbf{X}_i(t) + \int_t^{t+\Delta t} \mathbf{v}(\mathbf{x},\tau)\, d\tau \tag{1}$$

where $\mathbf{X}_i$ is the spatial position of a virtual particle i, and $\mathbf{v}(\mathbf{x},\tau)$ is the Eulerian velocity field (here, from GLORYS12) interpolated at the particle position using the scheme described by Delandmeter and van Sebille (2019) for A-grid. The Eulerian velocity field $\mathbf{v}(\mathbf{x},\tau)$ is equal to the Lagrangian velocity field $d\mathbf{X}/dt$ when evaluated at $\mathbf{X}(t) = \mathbf{x}$ (van Sebille et al., 2018). Here, the integration was done through a fourth-order Runge–Kutta scheme with a time step of 10-min (other time steps produced similar results). At every time step, temperature and salinity data were assigned for each particle i by linearly interpolating the GLORYS12 temperature and salinity fields to the particle position.

Two goals guided the setup of the numerical experiments in this study. The first one was to assess the statistical skill of GLORYS12 to capture the Gulf of Aden circulation at the RSOW layer as measured by REDSOX RAFOS floats. The second goal was to investigate the typical advective pathways and transit times of the RSOW spreading in the Arabian Sea using particles as a proxy indicator for the RSOW, including the effects of the intermediate circulation seasonal variability and the mesoscale eddy field.

In total, six numerical experiments were performed, as shown in Table 1. Experiments 1–3 are related to the REDSOX and prefixed as EXP-RAFOS. The first experiment (EXP-RAFOS) was tailored to be similar as possible to the in situ floats. The particle's initial positions were taken from the 49 RAFOS (Fig. 2a), except at the Tadjoura rift at the mouth of the Red Sea (42.5° E–43.3° E) in which the GLORYS12 fields are undefined near the RAFOS pressure level (see, e.g., the salinity fields in Fig. 2b–c). To circumvent that, their initial positions were displaced to the closest GLORYS12 valid grid point ($\leq$16.7 km distance). In this experiment, the particles were released at three vertical levels within the RSOW layer: 541 m, 644 m, and 763 m to verify which of those vertical levels better reproduced the RAFOS statistical characteristics. Since the REDSOX floats were almost isobaric, EXP-RAFOS did not consider vertical motions such as upwelling and downwelling; thus, the virtual particles drifted for their entire lifespan at the vertical surface they were released. The synthetic trajectory data (position, time, temperature, and salinity) were recorded every 6-hours, mimicking the REDSOX characteristics. Zonal and meridional velocities along the trajectories were estimated based on position and time data. The releasing time and tracking period were as in the REDSOX (see Furey et al., 2005, their Table 1).

EXP-RAFOS-SIGMA was identical to EXP-RAFOS except virtual particles followed isopycnal surfaces similar to the observed RSOW. The particles were released at 27, 27.3, and 27.6 kg/m^3 surfaces (top, core, and bottom of the RSOW layer; Table 1). EXP-RAFOS-REP consisted of having multiple realizations of the EXP-RAFOS experiment over the REDSOX period (2001–2003) to increase the statistical significance (see discussion in van Sebille et al., 2018). In this case, 49 particles were released every day for two years (2001 and 2002) at 763 m, totaling about 10^4 particles and 731 repetitions of EXP-RAFOS (Table 1). The 763 m depth was chosen for this experiment because EXP-RAFOS statistics at this level were the best compared to RAFOS as described in Section 4.2. Each virtual particle in the EXP-RAFOS-REP was tracked by 1-year as in the REDSOX.

Experiments 4–6 are related to the second objective of this study and are prefixed as EXP-RSOW (Table 1). All of them are centennial simulations. The first two EXP-RSOW experiments use daily velocity, temperature, and salinity fields of a climatological year. The aim was to minimize interannual variability and highlight the typical RSOW spreading patterns. For that, the GLORYS12 fields were averaged over 25 years for each day of an idealized year. This procedure was executed for each vertical level (z or σ). There is no jump between the first and last days of this idealized year (not shown), and it contains both the seasonal cycle and sub-seasonal variability. This approach is in the spirit of what is done for normal-year atmospheric forcing fields, as described in Large and Yeager (2004) and Large and Yeager (2009) and similar to one of Schmidt et al. (2020) Lagrangian simulations. These daily normal-year data were then repeated multiple times over the simulation period.

In experiment 6, the original GLORYS12 fields were used as a control run to evaluate whether more energetic mesoscale eddy fields would impact the probabilities and transit time statistics. The initial conditions for this experiment are based on the year 1993. Investigation of the interannual variability in initial conditions is left for a future study. The particles were released in the first year of the reanalysis and integrated over the simulation period (100-yr). Hence, particles in this experiment were subject to interannual variability in mid-depth circulation while in the Arabian Sea. The GLORYS12 spans a relatively short period (25-years), which is insufficient for particles spreading all over the Arabian Sea. To circumvent this issue, a technique known as "recycling" was employed (e.g., Gary et al., 2014; van Sebille et al., 2012, and references therein). It consists of repeating (looping) the Eulerian fields sequentially over the simulation period, here a hundred years. van Sebille et al. (2012) used this technique to extend their Eulerian model outputs from 27 to 300 years.

Notice that the normal-year daily-mean fields used in experiments 4–5 are rich in mesoscale eddies (Fig. 3a) since 25-years is short to fade out these features in eddy-rich regions such as the Gulf of Aden and the Arabian Sea. Therefore, the simulations based on these fields also include mesoscale effects, although the strength of the eddies is reduced when compared with GLORYS12 original fields used in experiment 6 (Fig. 3b).

In the EXP-RSOW experiments, instead of using the RAFOS positions that spread over the entire Gulf of Aden, the virtual particles were released in the westernmost area of the Gulf of Aden (box in Fig. 2a) as a proxy indicator to evaluate the RSOW spreading pattern due to intermediate-level circulation. Specifically, 183 particles (one particle per valid horizontal grid point, $\approx$8 km apart) were released every 5-days for one year at three vertical levels, with each particle tracked for 100 years—similar to Durgadoo et al. (2017). The particles were released at a 5-day interval instead of daily as in EXP-RAFOS to minimize the computational time since the EXP-RSOW experiments are centennial simulations. The total of particles per vertical level was in the order of 10^4 (Table 1). The synthetic trajectory data were recorded daily. In these simulations, the amount of particles at each releasing time is constant year-round. Thus, the simulations do not consider the known seasonal variation of the Red Sea outflow transport to the Gulf of Aden. This setup was chosen because the present study aimed to evaluate the spreading pattern and time scales associated with the Gulf of Aden/Arabian Sea intermediate circulation.

No vertical advection was considered in the EXP-RSOW experiments. This approach was adopted after a careful analysis of synthetic trajectories from a preliminary short-term experiment (3-years) that took into account vertical advection. There are no native vertical

Table 1

Lagrangian particle tracking simulations. The left columns identify the experiment number. The central part gives information about the particles released in each experiment (position, time, and vertical level). The right side shows the tracking period and the number of particles per vertical level. Note that at 27.6 kg/m^3, about 31% of the released particles were not advected. On average, in the EXP-RSOW-SIGMA, the isopycnals in the release points are shallower by 50 m in relation to EXP-RSOW-SIGMA-93 and deeper by 100 m in summer.

Experiment		Release			Particles	
#	id	Position	Time	Vertical levels	Tracking period	Particles per level
01	EXP-RAFOS	REDSOX	REDSOX	541, 644, 763 m	REDSOX	49
02	EXP-RAFOS-SIGMA	REDSOX	REDSOX	27, 27.3, 27.6 kg/m^3	REDSOX	49
03	EXP-RAFOS-REP	REDSOX	every day for 2-years	763 m	1-year	35819
04	EXP-RSOW	outflow region	every 5-days for 1-year	541, 644, 763 m	100-year	13359
05	EXP-RSOW-SIGMA	outflow region	every 5-days for 1-year	27, 27.3, 27.6 kg/m^3	100-year	13359
06	EXP-RSOW-SIGMA-93	outflow region	every 5-days in 1993	27, 27.3, 27.6 kg/m^3	100-year	13359

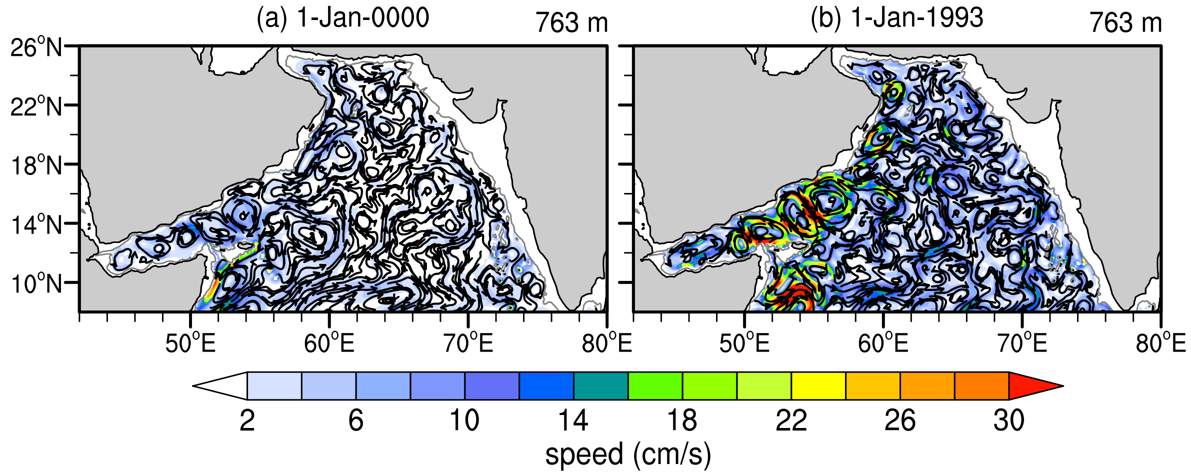

Fig. 3. Example of daily GLORYS12 velocity fields at 763 m used for the EXP-RSOW simulations. The left panel shows a long-term daily average over 25-years of the reanalysis, and the right, an instantaneous daily field in 1993. Both are rich in mesoscale eddies, although the eddies are weaker in the long-term average. The gray contour is the 700 m isobath from ETOPO2. (For interpretation of the references to color in this figure legend, the reader is referred to the web version of this article.)

velocity fields (w) available in GLORYS12, and w was estimated from u and v fields by integrating the continuity equation, assuming zero vertical velocity at the sea surface and the seafloor similar to Wang et al. (2019). However, these w fields were estimated from the already interpolated A-grid, which introduces numerical noise. Moreover, GLORYS12 assimilates observations using a 3D-VAR approach that disturb the ocean model's dynamical balance, and estimated vertical velocities must be interpreted with caution since errors can be substantial in eddy-rich areas for this kind of assimilation approach (e.g., Pilo et al., 2018). In the short-term experiment, there were a few outliers trajectories in which some particles sank to the seafloor in the Gulf of Aden, which may or not be correct. Because of the uncertainties associated with the w calculation and the fact that the observed RSOW mostly spreads along isopycnals (weak diapycnal mixing) within $27\text{–}27.6\sigma_\theta$ layer (Beal et al., 2000; Bower et al., 2000, 2005; Matt and Johns, 2007; L'Hégaret et al., 2021), out of caution, no vertical advection was considered for the 100-year simulations. Most results presented in the next sections are based on the isopycnal simulations, but the isobaric ones are briefly described to keep consistency with the EXP-RAFOS. Particles on isopycnal simulations go up and down in the water column as a result of isopycnic heaving.

Despite the limitation cited above, the synthetic trajectories reveal the preferred pathways of the RSOW spreading in the Arabian Sea in a similar way that trajectories computed from altimetry and drifter-derived velocity fields, which have non-zero horizontal divergence, also provide valuable diagnostic information about the surface flows (van Sebille et al., 2018). Similarly, Cedarholm et al. (2019) used isopycnal Lagrangian simulations to investigate the advective pathways in the North Pacific Ocean of the cesium released during Japan's Fukushima Daiichi Nuclear Power Plant disaster in 2011.

In all numerical experiments described here, an artificial boundary current was implemented to push away virtual particles that got stuck over the shelf break since velocity fields are not defined there at the RSOW layer (400–800 m). This artificial current, normal to shelf-break contour, had a value of 1 m/s exactly at the contour and zeroed everywhere else. With an integration time step of 10-min, this is equivalent to a displacement of about 0.6 km, just enough for particles to be advected again. This implementation is similar, for instance, to Onink et al. (2019) and Sterl et al. (2020), who showed that the results with or without an artificial boundary current are similar outside the boundaries, except that more synthetic trajectories are available for statistical analyses in the former case.

Advection of particles stopped when the particles exited the Arabian Sea (8° N–26° N; 42° E–78° E). In the 100-year simulations, 83.4% (EXP-RSOW-SIGMA), 98.0% (EXP-RSOW-SIGMA-93), and 96.3% (EXP-RSOW) of particles had left the Arabian Sea when the simulation ended, but none in the short-term EXP-RAFOS. The particles within the Arabian Sea were everywhere over the domain in the long-term simulations (not shown), without any defined spatial pattern.

3.2. Statistical analyses of virtual particles

Several statistics were computed based on the synthetic trajectories to assist the investigation of the preferred RSOW pathways and transit times. Mean quasi-Eulerian velocity and eddy kinetic energy (EKE) fields (Lankhorst and Zenk, 2006; Sparrow et al., 2002) were calculated into a regular grid with cells of 0.25° (EXP-RAFOS experiments) and 0.5° when the Arabian Sea domain was considered (EXP-RSOW experiments). The present study refers to these gridded fields as quasi-Eulerian to differentiate them from the GLORYS12 Eulerian fields, following the nomenclature adopted by Sparrow et al. (2002). To generate the gridded fields, for each grid cell, the mean velocity ($\bar{u}$ and $\bar{v}$) was computed by averaging all Lagrangian velocity data (u, v)

within the cell, and mean EKE as $0.5(\overline{u'}^2 + \overline{v'}^2)$, with $u' = u - \bar{u}$ and $v' = v - \bar{v}$. Because the regional circulation reverts direction seasonally, including the intermediate depths where the RSOW lies (e.g., Schott and McCreary, 2001), the mean EKE and velocity maps were also calculated separately for the winter (December–March) and summer (June–September) monsoons.

Two types of probability distribution maps were also calculated for each experiment (van Sebille et al., 2018). One map expresses the likelihood of a region being visited by particles. It is calculated by counting all particle positions crossing a grid cell (n_{cell}), which may include multiple visitations by a single particle, and dividing it by the total number of particle positions (over all grid cells) such that $P_{multi}(i,j) = n_{cell}(i,j)/n_{total}$. The other map expresses the probability of a region being visited by distinct particles. It is calculated by counting the number of unique particles that visited a grid cell and dividing it by the total number of distinct particles released in the experiment ($P_{unique}(i,j) = n_{unique}(i,j)/n_{released}$). These maps represent normalized particle density distributions. They were both computed using the entire particle datasets or subsets of them. For instance, maps were built for particles released at a specific depth/isopycnic or released at a particular season (winter and summer), as described in Section 4.2.

To estimate the advective timescales of the RSOW spreading in the Arabian Sea, for each particle i, the time interval between the releasing point (origin) and the first arrival in specific regions (destination) were calculated ($\Delta T_i = T_i(d) - T_i(o)$). Here, the destinations are the grid cells. For each grid cell, the ΔT_i set forms a transit time distribution (TTD), and several statistics can be estimated, such as modal value (most frequent), mean, and standard deviation (van Sebille et al., 2018). These statistical parameters were estimated for each cell into $0.5° \times 0.5°$ grid. To analyze whether the seasonal variability of the intermediate circulation in the Red Sea outflow area influences transit times, similar statistics were also computed separately based on particles released in winter and summer. Additionally, transit time statistics were computed for particles exported from the Gulf of Aden via the Socotra Passage and the Gulf's mouth (Fig. 2c, pink lines). For all statistical calculations, only the transit times of the first cross were taken into account.

Like TTD, the strength of salinity dilution in the Arabian Sea was inferred by calculating the salinity anomaly for each particle in relation to the salinity at the initial particle position: $\Delta S_i = S_i(d) - S_i(o)$. Then, statistics (mean, modal, and standard deviation) were computed for each bin in a 0.5° grid.

All statistics shown in the present study only consider particles that were advected of their initial positions. In the isopycnal simulations, the densest isopycnic ($27.6\sigma_\theta$) does no always exist in the outflow area.

4. Results

4.1. Climatological perspective of the RSOW in GLORYS12

Before analyzing the Lagrangian simulations based on GLORYS12 velocity fields, this section takes a brief look at how the reanalysis represents typical climatological characteristics of the RSOW in the Gulf of Aden. For that, monthly-mean climatological fields were computed for all variables over the 1993–2018 period. In addition, the velocity fields near the Strait of Bab al-Mandab were rotated into along- and across-strait directions similar to Murray and Johns (1997) aiming to capture the Red Sea outflow better.

Fig. 4a shows GLORYS12 along-strait velocity (color) and salinity (contours) averaged over a section at the strait (section B in Fig. 5a). It can be seen that GLORYS12 reproduces reasonably well the typical features and seasonal cycle of the circulation at the strait as described by Murray and Johns (1997), Sofianos et al. (2002), and Sofianos and Johns (2015). A two-layer system exists in winter (October–May), characterized by a relatively fresh (36–36.2) inflow at the surface (the Gulf of Aden Surface Water) and a saltier (37–39.8) outflow (the RSOW) at depth. In summer (June–September), a three-layer system develops, with a shallow surface outflow (top 30 m), an inflow of the fresher Gulf of Aden Intermediate Water (<35.8–36), and a diminished RSOW outflow (Fig. 4a). Also, velocities in GLORYS12 are comparable to in situ observations of Murray and Johns (1997) and Sofianos et al. (2002). They described currents up to 1.2 m/s at the RSOW layer in winter with a surface inflow of 40–60 cm/s, which GLORYS12 (Fig. 4a, color) is in agreement with.

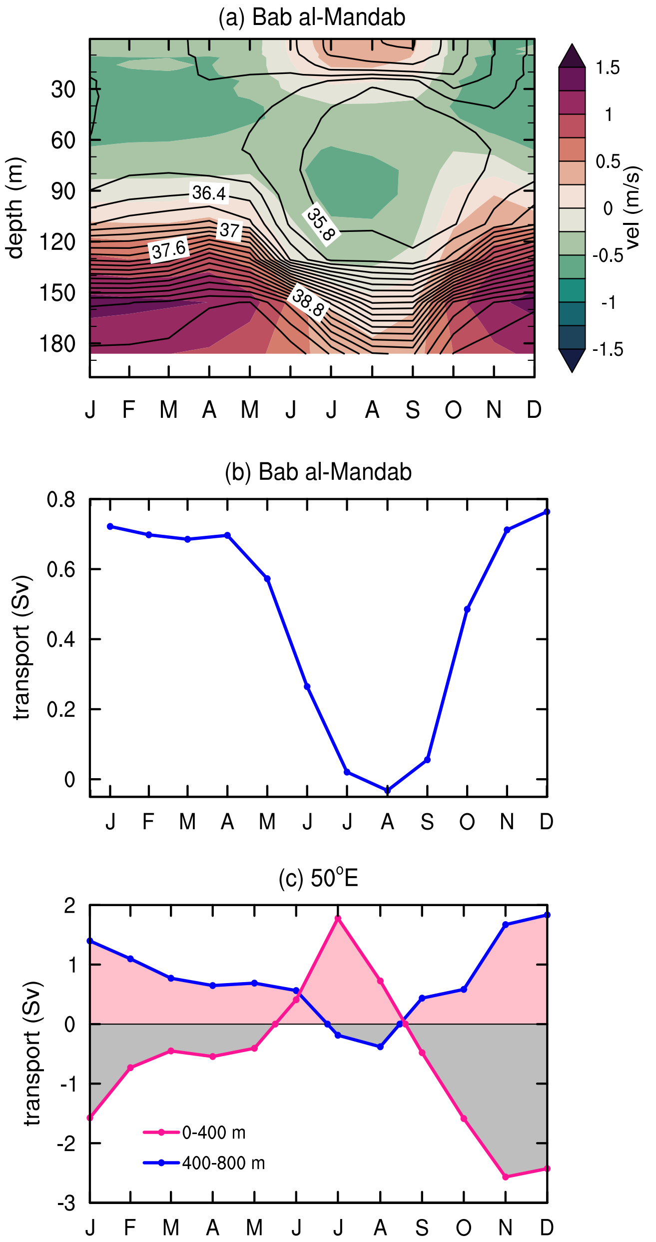

Fig. 4. GLORYS12 monthly-mean climatology (1993–2018). (a) averaged along-strait velocity (color) and salinity (contours) over section B in Fig. 5. Positive values indicate currents from the Red Sea to the Gulf of Aden (outflow) and negative values toward the Red Sea (inflow). (b) seasonal cycle of along-strait volume transport (100–220 m). 1 Sv = 10^6 m^3/s. Positive values indicate transport out of the Red Sea. (c) zonal transport at 50° E for the upper layer (0–400 m; pink curve) and RSOW layer (400–800 m; blue curve) (section M in Fig. 5). Positive values (toward the Arabian Sea) are highlighted in pink and negative in gray. (For interpretation of the references to color in this figure legend, the reader is referred to the web version of this article.)

Following Murray and Johns (1997), the outflow volume transport at the strait was calculated as:

$$V_{RSOW} = \int_{z1}^{z2} \int_{0}^{L(z)} v(x,z)\,dx\,dz \tag{2}$$

where $v(x,z)$ is the along-strait velocity component, $L(z)$ is the width of the strait at each depth, and z_1 and z_2 are the vertical limits of the RSOW layer defined here (based on Fig. 4a) as 100 and 200 m, respectively.

In the same range of observations made by Murray and Johns (1997), the RSOW transport in GLORYS12 varies from 0.76 Sv in winter to about zero in summer (0.02 in July), with a shut off in August. Specifically, in the measurements of Murray and Johns (1997) (1995–1996), transport peaks at mid-february (0.7 Sv) and is reduced to about 0.05 Sv in July to mid-September (essentially shut-offing briefly in early September).

While the RSOW transport into the Gulf of Aden is known from observations, the export from the Gulf to the Arabian Sea is not. Han and McCreary (2001), based on a back-of-the-envelope calculation, estimated an annual mean of 1.2 Sv of RSOW being transported out of the Gulf at 50° E (M section in Fig. 5a). They argue that the increased RSOW transport is due to the isopycnal mixing of the source RSOW with ambient waters. Here, the zonal transport at 50° E was computed for the 400–800 m layer. In GLORYS12, the annual transport is 0.8 Sv (±0.6), which is of order estimated by Han and McCreary (2001). Furthermore, in GLORYS12, there is a clear seasonal cycle in the RSOW export to the Arabian Sea (Fig. 4c, blue curve). Maximum transport occurs in December (1.8 Sv). In summer, the transport is reduced and even shut off in July and August. In GLORYS12, the RSOW transport to the Arabian Sea is in phase with the outflow transport at the Strait of Bab al-Mandab, and in opposite phase with the surface layer (0–400 m) (Fig. 4c, pink curve). At the surface, the Gulf of Aden imports water in winter (maximum of 2.57 Sv) and exports in summer (peak in July, 1.78 Sv), consistent with the seasonal cycle of evaporation in the Red Sea (Menezes et al., 2019) that drives the overturning circulation and the RSOW formation.

Fig. 5 shows the monthly mean climatology of salinity at $27\sigma_\theta$ (top of the RSOW). For comparison, other RSOW climatologies can be found in Bower et al. (2000) and Carton et al. (2012), and also in Figures S1–S3. Supplementary figures include the World Ocean Atlas 2018 (WOA18; Zweng et al., 2018), the (free-run) 1/10° OGCM for the Earth Simulator (OFES; Sasaki et al., 2008), and Estimating the Circulation and Climate of the Ocean (ECCO v4r4; Forget et al., 2015). In addition, there is Figure 10 of Bower and Furey (2012) who have produced salinity maps on three isopycnal surfaces (27, 27.2, and $27.48\sigma_\theta$) for REDSOX-1 and REDSOX-2 measurements.

Salinity at $27\sigma_\theta$ in GLORYS12 decreases from west to east, reflecting the isopycnal mixing of the RSOW with fresher ambient waters, such that in the Gulf's mouth, salinity is lower, around 35.8. The high saline tongue (≥36.6) originating at the Strait of Bab al-Mandab concentrates along the Gulf' southern boundary, which agrees with the climatological description of the RSOW given by Bower et al. (2000). This salty feature also appears in REDSOX maps of Bower et al. (2002) and Bower and Furey (2012), and in the numerical simulations of Ilicak et al. (2011). In GLORYS12, a seasonal cycle is apparent. The salty tongue is stronger in the first half of the year and is well defined west of 47° E in early winter. As the winter progresses, this feature extends more and more to the east. It reaches maximum extension in summer (June) when its fingerprint is seen as far as 52° E. This description is consistent with Bower et al. (2000), which found the greatest longitudinal extension of recently injected RSOW in June. It is also in agreement with Carton et al. (2012). The latter authors describe intensified zonal gradients of temperature and salinity in May, which is shifted eastward, and weaker in November. However, their low-spatial resolution climatology does not show structures within the Gulf, as seen in GLORYS12 or the REDSOX maps of Bower et al. (2002) and Bower and Furey (2012).

Compared with other climatologies (Figures S1–S3), GLORYS12 is more consistent with the accumulated knowledge in the literature about the RSOW (e.g., Bower et al., 2000, 2002; Bower and Furey, 2012). For instance, it is hard to identify the RSOW in WOA18 (Figure S1) because salinity in the Gulf is overall low (<35.8) and much more homogeneous in space (no clear signature of RSOW). This is likely due to the smoothing of the statistical interpolation used to produce the WOA18. Salinity is even much lower in OFES (<35.5; Figure S2), which also has reduced gradients. In ECCO, salinity is comparable with GLORYS12 as ECCO is also constrained by observations, but salinity decreases monotonically from east to west due to ECCO's low spatial resolution (≈100 km) to resolve Gulf's features.

4.2. Evaluation of GLORYS12 against REDSOX observations in the Gulf of Aden

Given that GLORYS12 represents relatively well typical climatological characteristics of the RSOW as shown in the previous section, the attention now turns to how the synthetic trajectories compare with the trajectories from RAFOS floats during the REDSOX experiment in the Gulf of Aden.

The Gulf of Aden is dominated by mesoscale eddies and submesoscale processes including the RSOW layer (e.g., Bower et al., 2002, 2005; Bower and Furey, 2012; Carton et al., 2012; Fratantoni et al., 2006; Morvan et al., 2020; Al Saafani et al., 2007). In such environments, synthetic trajectories are not expected to reproduce the observed ones but instead their statistical properties (e.g., van Sebille et al., 2009). Take, for example, the synthetic trajectories shown in Fig. 6a. The virtual particles and RAFOS floats were released at the same position (12° E; 45° E), at similar depths, and concurrent dates. The two sets are composed of convoluted trajectories, with a dominance of mesoscale eddies but distinct evolution. In general, the synthetic trajectories are characterized by loops with larger diameters, which is not a surprise given the horizontal and temporal resolutions of the Eulerian velocity fields used for the simulations (1/12° and daily-averages). In the most western part of the Gulf, these GLORYS12 trajectories at 763 m do not reproduce the presence of a small energetic cyclonic (counterclockwise) eddy between 44° E–45° E that was measured by floats and hydrography during REDSOX (Bower et al., 2002, 2005; Bower and Furey, 2012). In Fig. 6a, one virtual particle escaped the Gulf through the Socotra passage between Socotra Island and the Horn of Africa, which is consistent with Schott and Fischer (2000).

Unlike the synthetic trajectories, the RAFOS trajectories are not continuous east of 49° E, and (apparently) no float followed the Socotra Passage or escaped the Gulf in Fig. 6a. All RAFOS trajectories are limited to 50° E–52° E. This is not a fault of GLORYS12 simulations as it could be imagined but rather an observational issue. As previously mentioned, during the REDSOX, float tracking was limited because of the absence of sound sources that reached these far regions (see sound source locations in Fig. 6a; Furey et al., 2005). Argo floats have not such limitations. From the 32 Argo trajectories in the Gulf of Aden over the last 18 years, 17 have crossed the 50° E meridian (Fig. 6b).

Despite the differences discussed above, collectively, the statistical properties from the EXP-RAFOS and EXP-RAFOS-REP (731 realizations of EXP-RAFOS) are similar to RAFOS statistics. Statistics for RAFOS and synthetic trajectories were calculated within the Gulf until 52° E (and do not include the Socotra Passage). Bower and Furey (2012) described that mid-depth velocity based on the RAFOS is weakest in the western Gulf and fastest in the eastern (their Fig. 16). Similar description was given by Carton et al. (2012) based on Argo floats. This longitudinal pattern in velocity is robust and reproduced both by EXP-RAFOS and EXP-RAFOS-REP (Fig. 7a). Mean velocity and standard deviation increase from 6.5 ± 3.8 cm/s at 44.5° E to 14.3 ± 8.0 cm/s at 51.5° E (6.0 ± 4.0 to 14.7 ± 9.1 cm/s for EXP-RAFOS-REP). These statistics are of same order as RAFOS (8.1 ± 5.1 to 15.9 ± 7.9 cm/s; Fig. 7a). Not only the mean and standard deviation are consistent

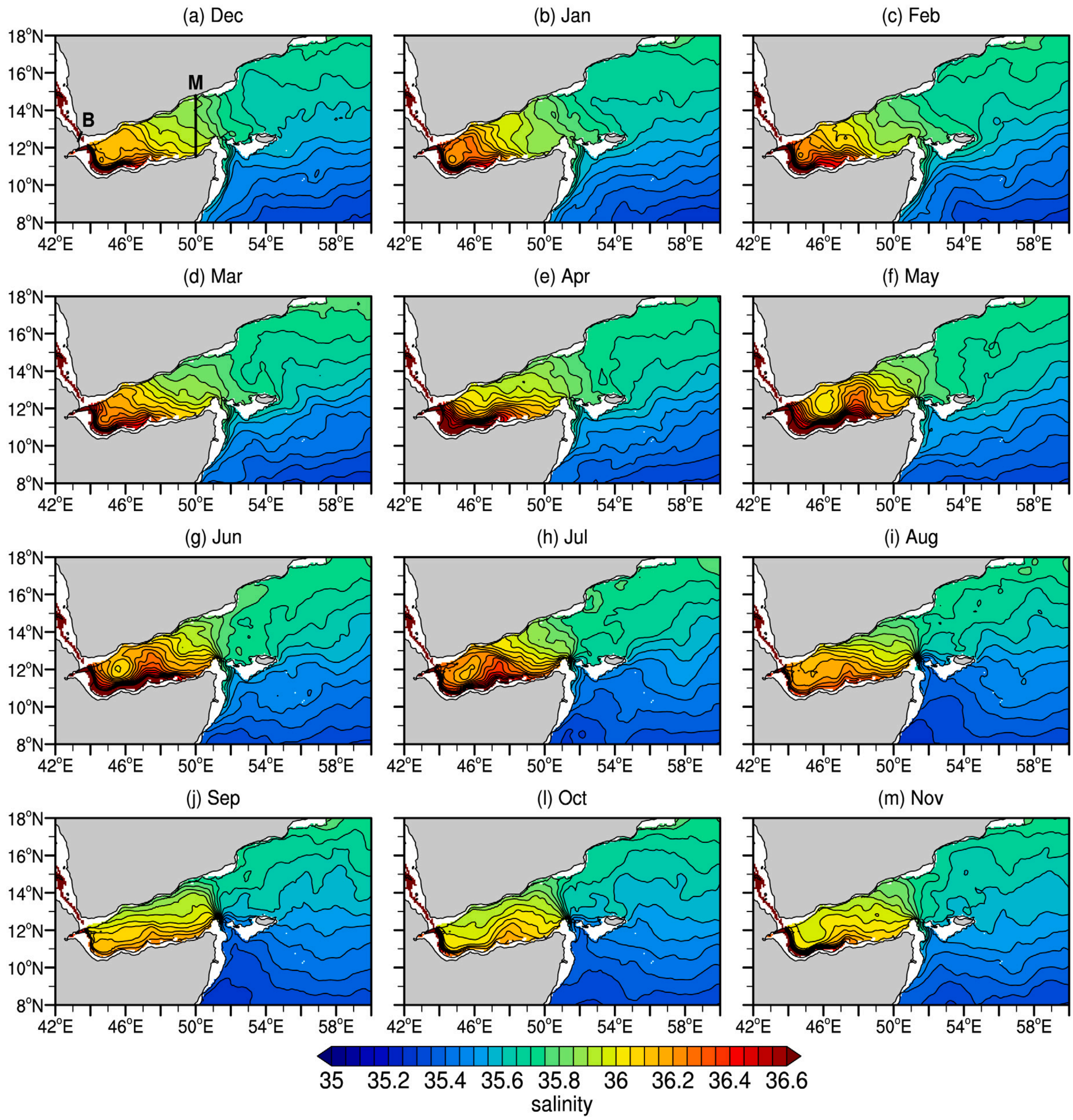

Fig. 5. GLORYS12 monthly mean climatology of salinity over the 1993–2018 period at $\sigma_\theta = 27$ kg/m^3. In (a): section B is at Strait of Bab al-Mandab, and section M is at 50° E (Gulf of Aden's mouth).

with RAFOS, but also the probability distributions of speed, u, and v velocities (Figs. 7c, 7e and 7f, respectively).

In contrast with velocity, temperature statistics are not entirely reproduced by GLORYS12 at 763 m (Fig. 7b). West of 46.5° E, the observed mean temperature decays by about 4 °C from the Tadjoura rift to 46° E, while in GLORYS12, there is no significant variation in temperature in this region. Neither a reduction in standard deviation is observed (Fig. 7b, dashed curves). Thus, the reanalysis does not capture the RSOW transformation in the western Gulf.

In both EXP-RAFOS and EXP-RAFOS-REP, warm water classes (>14 °C) that were measured by the floats are absent at 763 m as seen at the histogram shown in Fig. 7d. These differences are corroborated by the T–S diagrams based on independent CTD observations (Fig. 8). The modeled RSOW west of 45° E is lighter in the T–S diagrams, with the data tending to concentrate toward the $27\sigma_\theta$. In contrast, the observed RSOW is much saltier and spreads within the $27–27.6\sigma_\theta$ layer in this region. GLORYS12, however, captures the seasonality in the RSOW layer, with saltier/warmer water in winter as expected and consistent with the climatology shown in the previous section.

The disagreement between GLORYS12 and in situ observations in the western Gulf described above is likely due to excessive numerical mixing over the overflow sill in the oceanic model and the relaxation to the climatology applied to mitigate it (Lellouche et al., 2018), since, at the Strait of Bab al-Mandab, GLORYS12 reproduces relatively well the RSOW salinity and transport into the Gulf (Figs. 4a–b). As described in the Introduction, this is a common issue in OGCMs, especially models using z-level coordinates (Colombo et al., 2020; Legg et al., 2009) such as NEMO, the underlying model in GLORYS12. Additional evidence of excessive numerical mixing appears when the temperature distributions of EXP-RAFOS at 541 m and 644 m are contrasted with RAFOS. In this case, there are water classes with temperatures higher than 14 °C in the reanalysis (Figure S4d), and the change from warmer to colder water is apparent west of 46° E although weaker than in the observations (Figure S4b). Thus, the water properties in the western Gulf are closer to observed RSOW in these shallower depths. The shallowness of the

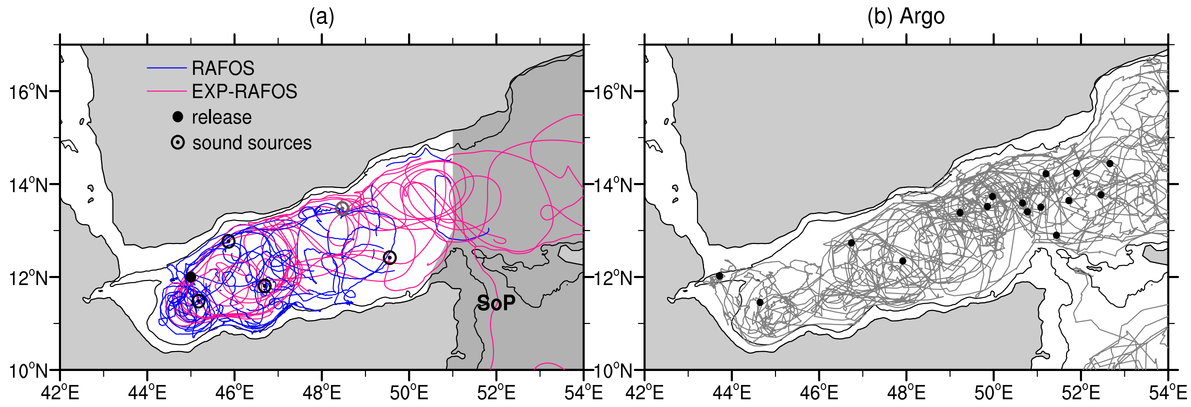

Fig. 6. Trajectories in the Gulf of Aden: (a) from six RAFOS floats (blue) deployed at 12° N-45° E (black dot) and respective synthetic trajectories at 763 m from EXP-RAFOS (pink). The release time and tracking period are the same for both datasets. In-situ floats could not be tracked east of 50° -52° E (gray shading) (Furey et al., 2005) due to limitations sound source coverage (circled dots). Note that four sources (black circled dot) were installed during REDSOX-1 and available for the entire project, and one during REDSOX-2 (gray circled dot). (b) Trajectories from all Argo floats released in the Gulf Aden and crossed the 50° E meridian. Black dots indicate the initial float position. In the maps, the black contour is the 700 m isobath from ETOPO2. SoP stands for Socotra Passage. (For interpretation of the references to color in this figure legend, the reader is referred to the web version of this article.)

modeled RSOW also appears in the T–S diagrams, especially in winter, in which water above 15 °C is closer to the $27\sigma_\theta$ in GLORYS12 and denser than that in the observations (Fig. 8). While in the western Gulf, the mean temperature and standard deviation are closer to observations at these shallow levels, in the eastern Gulf, the simulation at 763 m agrees better with RAFOS (compare Figs. 7b and S4b).

Nevertheless, the absence of salty/warm water classes west of 46° E is likely not to affect the modeled Arabian Sea water mass properties and the large scale mid-depth circulation since the Arabian Sea receives a diluted version of the RSOW after intense isopycnal transformation of this water mass in the Gulf of Aden. In the Gulf's mouth, the mean temperature and standard deviation at 763 m are close to the observations (Fig. 7b), as well as the T–S properties in the RSOW layer (Fig. 8). This is also because more Argo observations exist in the Arabian Sea to constrain GLORYS12.

For the sake of clarity, henceforth, the analyses focus on the 763 m simulations because, as a whole, their statistics better agree with RAFOS.

4.2.1. Mean and seasonal circulation/EKE patterns from RAFOS, EXP-RAFOS and EXP-RAFOS-REP

The mean circulation fields derived from EXP-RAFOS and EXP-RAFOS-REP at 763 m show weak mean currents (<10 cm/s) at 763 m, a basin-scale eastward flow in the central-southern portion of the Gulf, and a presence of a well-defined cyclonic eddy in the west between 44° E–47° E. At GLORYS12, this basin-scale geostrophic eastward flow is driven by a weak mean north–south density gradient at mid-depths (400–1000 m). Due to the RSOW presence, the mid-depth waters are, on average, slightly denser in the southern part in GLORYS12, similar to in situ observations (e.g., Bower et al., 2000; Schott and McCreary, 2001). The observed mean currents derived from RAFOS are also weak and overall eastward, but simulations and observations have different patterns (Fig. 9d–e). The observed cyclonic eddy in the western Gulf is weaker and has half of the diameter (44° E–45° E) than the simulated ones. Also, there is a distinct anti-cyclonic feature between 50° E–52° E that is not present in EXP-RAFOS, and EXP-RAFOS-REP mean fields. Visual inspection of individual trajectories (not shown) revealed four trajectories in EXP-RAFOS and three in RAFOS following an anti-cyclonic eddy in the region. However, the RAFOS has much fewer data east of 50° E due to tracking issues, and the anti-cyclonic became imprint in the mean fields.

A strong agreement exists between the mean circulation from EXP-RAFOS (based on 49 virtual particles) and EXP-RAFOS-REP calculated from a much larger number of particles (order 10^4). Also, EXP-RAFOS is consistent with the Eulerian mean computed directly from the GLORYS12 fields over the REDSOX years (Figure S5) and with other levels in the RSOW layer (Figure S6). If velocity data are binned by season, the winter (December to March) and summer (June–September) patterns are similar to the mean (not shown). In all cases, currents are weak, dominated by eddy features, but with an eastward background mean flow.

For the EKE, the EXP-RAFOS pattern at 763 m is also consistent with RAFOS (Fig. 9a–c). Both have similar amplitudes, maximum around 200 $\mathrm{cm}^2/\mathrm{s}^2$, with EKE increasing eastward. West of 46° E, the EKE tends to be slightly lower in the simulations than in the observations. In the seasonal timescale, maps are in agreement with observations. EKE is slightly higher in winter (Figure S7) when westward propagating eddies are known to enter the Gulf (e.g., Al Saafani et al., 2007). Seasonal Eulerian means based on GLORYS12 fields at 763 m over the REDSOX period are almost identical to EXP-RAFOS-REP (not shown).

In conclusion, GLORYS12 captures the fundamental characteristics of the mesoscale field in the Gulf of Aden, which is crucial because the spreading of the RSOW is strongly affected by eddies (Bower et al., 2002; Bower and Furey, 2012; Carton et al., 2012).

4.2.2. Simulated and observed particle probability distributions in the Gulf of Aden

Fig. 10 shows the probability distributions of particle positions based on RAFOS, EXP-RAFOS, and EXP-RAFOS-REP at 763 m. Two kinds of probability maps are plotted. The left side maps indicate the likelihood of a bin to be visited by a particle over the experiment period, which include multiple visitations by a single particle (P_{multi}), while the maps on the right side show the percentage of unique particles visiting a bin (P_{unique}). See Section 3.2 for details about these quantities.

Overall, simulated and observed probability maps are alike (Fig. 10). The P_{multi} maps show a high probability of particles staying in the western Gulf—where the velocities and EKE are weak—and a lower likelihood of reaching the Gulf's mouth even when year-round EXP-RAFOS-REP is considered. The probability in the western Gulf is lower in the simulations than in RAFOS (complementarily, Figure S8 shows differences), which is likely related to the cyclonic eddy previously described. The high differences in probability between observations and simulations at the Gulf's mouth are likely artifacts due to the REDSOX tracking limitation in this region.

There is strong connectivity within the Gulf. At least 35%–40% of the released particles/floats visited most regions, confirming the turbulent nature of the mid-depth circulation (Fig. 10, right column).

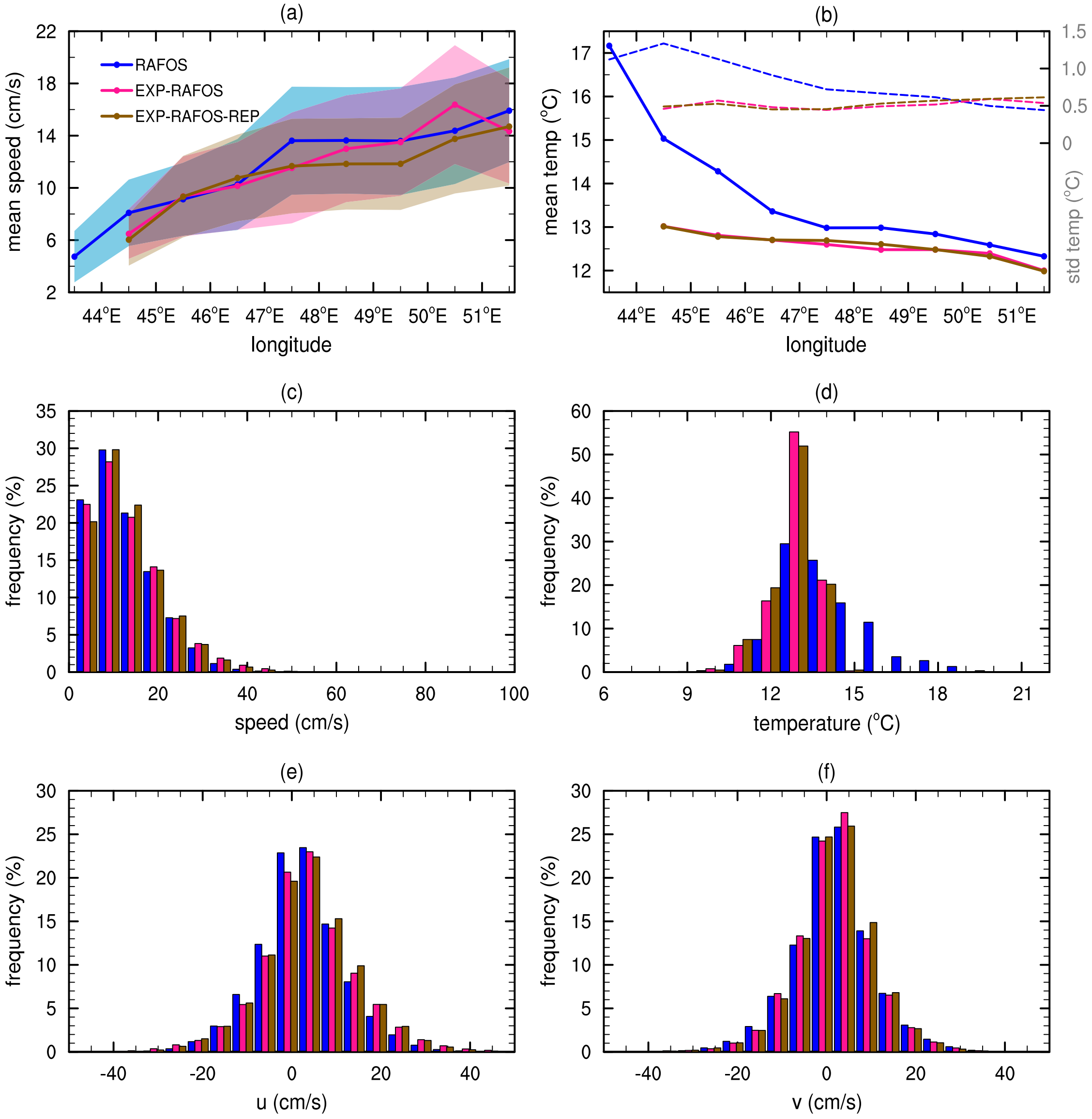

Fig. 7. Statistical comparison between particle tracking simulations at 763 m (EXP-RAFOS and EXP-RAFOS-REP) and in situ observations from the RAFOS floats. All plots use the same color scheme: RAFOS in blue, EXP-RAFOS in pink, and EXP-RAFOS-REP in brown. (a): mean speed versus longitude for data averaged in 1° longitudinal bins. Shading indicates the respective standard deviations for each bin. On the simulations, there is no data west of 44° E (Tadjoura Rift) at 763 m (see text for explanation). (b) similar to (a) but for (in situ) temperature. Dashed lines indicate the standard deviation that uses the right vertical axis. (c–f): histograms for current speed, (in situ) temperature, zonal (u) and meridional (v) velocities. Histograms were computed using bins of 5 m/s for speed, u, v, and 1 °C for temperature. (For interpretation of the references to color in this figure legend, the reader is referred to the web version of this article.)

In the simulations, P_{unique} is more homogeneous in space and reaches higher values, reflecting the meso-to-large scale nature of GLORYS12. In RAFOS, it is clear that the influence of the small energetic cyclonic eddy between 44° E–45° E.

On a side note, the probability maps for particles at 541 m and 644 m resemble the ones at 763 m (Figure S9), except that the particle density in the western Gulf is slightly lower in these shallow levels. A large portion of the released particles are likely to follow a pathway along the southern boundary west of 48° E (about 65% of the released particle followed this pathway at 541 m). Consequently, the differences between these shallow levels and RAFOS are larger than 763 m (Figure S10).

As previously stated, the RAFOS floats were only tracked within the Gulf to 52° E. Most floats (83.7%) remained in the Gulf for their entire 1-year mission. However, eight floats (16.3% of total) resurface to transmitted data in the Arabian Sea, with two on the southeast of Socotra. Similarly, eleven Argo floats released in the Gulf were exported to the Arabian Sea. The numerical simulations do not suffer from the sound source tracking limitation or reduced number of trajectories, which allows the calculation of statistics about the export of particles to the Arabian Sea. An in-depth analysis of the export of virtual particles as a proxy for the RSOW export will be presented in Section 4.3 based on the long-term simulations.

4.2.3. Isopycnal simulation in comparison with RAFOS

To evaluate the difference between isobaric particles, such as the floats used in the REDSOX, and isopycnal particles, which is best for capturing the RSOW advective spreading patterns, simulations using the same configuration as EXP-RAFOS were run except that at three isopycnal surfaces within the RSOW layer (Table 1). At = 27.6σ_θ (bottom of the RSOW layer), 38.8% of the released particles were not advected since this isopycnic does not always exist in GLORYS12 in the western Gulf, as shown in the previous sections.

Overall, the experiment at 27.3σ_θ (RSOW core) compares better with RAFOS (Figure S11). For this isopycnic, the statistical distributions

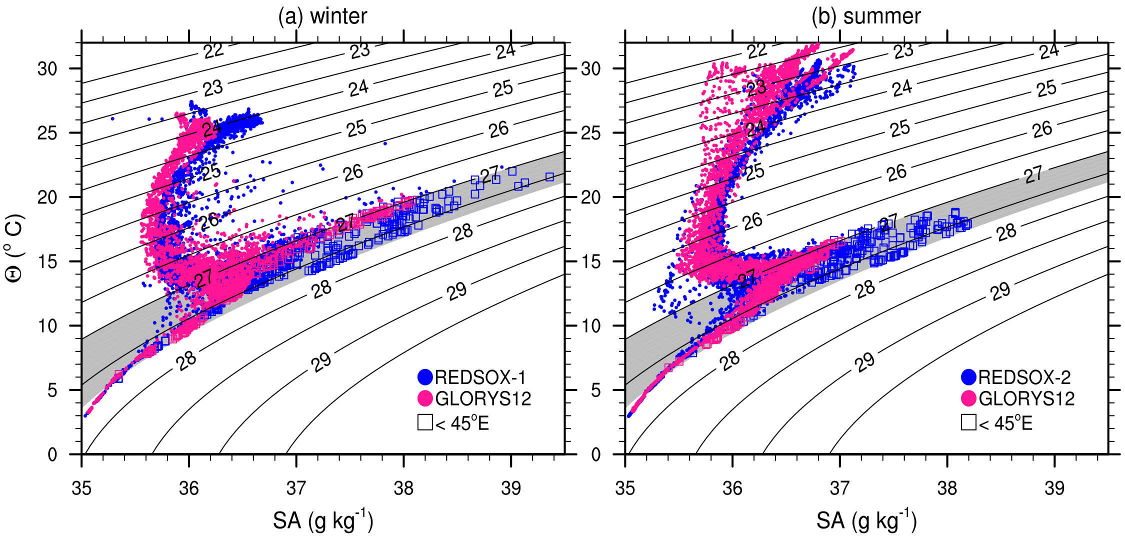

Fig. 8. T–S diagrams for the winter REDSOX-1 (a) and summer REDSOX-2 (b) from CTD observations (blue) and GLORYS12 data (pink) at same locations and dates. Contours are the potential density referenced to the sea surface (in kg/m^3). Empty square symbols are used to data west of 45° E, and solid circles to the east of this meridian. Gray shadings highlight the RSOW layer (27–27.6 kg/m^3). Θ is conservative temperature, and SA is absolute salinity. (For interpretation of the references to color in this figure legend, the reader is referred to the web version of this article.)

Table 2

Export of particles from the Gulf of Aden for different simulations. The first and second columns identify the experiments and the vertical level for which statistics were calculated. The third column shows % of advected particles that were in the Gulf of Aden (GA) and the Arabian Sea (AS) at the end of their life. The fourth column indicates the percentage of advected particles that visited the Arabian Sea at some point of their lifetime; the portion of particles that visited the Arabian Sea crossing the Socotra passage (SoP) or through the Gulf's mouth. The fifth column shows the respective transit time estimated from the transit time distributions. The first value is the modal value (the most frequent), the second value is the mean transit time, and the third the standard deviation.

id	Level	Last position		Exported particles			Transit time (days)	
		GA	AS	AS	SoP	Mouth	SoP	Mouth
EXP-RAFOS	763 m	65.3%	34.7%	40.8%	30.0%	70.0%	120–130 [199.0 ± 91.0]	300–310 [249.9 ± 89.2]
EXP-RAFOS-REP	763 m	60.3%	39.7%	46.0%	20.6%	79.4%	130–140 [201.6 ± 83.0]	250–260 [227.8 ± 81.6]
EXP-RAFOS-SIGMA	27.3 σ_0	57.1%	42.9%	46.9%	17.4%	82.6%	120–130 [215.6 ± 83.9]	280–290 [204.7 ± 87.7]
EXP-RSOW	541 m	0.1%	99.9%	100%	19.6%	80.4%	160–170 [576.8 ± 588.4]	200–210 [652.3 ± 575.3]
	644 m	0.1%	99.9%	100%	4.7%	95.3%	250–260 [633.4 ± 504.1]	220–230 [683.9 ± 538.6]
	763 m	0.1%	99.9%	100%	0.8%	99.2%	460–470 [1021 ± 553.4]	250–260 [830.8 ± 576.0]
EXP-RSOW-SIGMA	27.0 σ_0	0.1%	99.9%	100%	30.0%	70.0%	120–130 [611.5 ± 518.7]	180–190 [595.7 ± 522.5]
	27.3 σ_0	0.1%	99.9%	100%	1.2%	98.8%	450–460 [891.6 ± 563.2]	240–250 [776.7 ± 609.0]
	27.6 σ_0	41.5%	58.5%	68.6%	0%	100%		1010 [1090.3 ± 477.9]
EXP-RSOW-SIGMA-93	27.0 σ_0	0%	100%	100%	28.2%	71.8%	310–320 [333.3 ± 235.2]	100–110 [321.9 ± 277.9]
	27.3 σ_0	0%	100%	100%	15.2%	84.8%	250–260 [321.9 ± 198.1]	160–170 [437.2 ± 362.1]
	27.6 σ_0	6.7%	93.3%	93.3%	0%	100%		960 [3842.3 ± 3049.4]

of velocities are similar to the observed ones. Velocities and standard deviation are the same order as the observations, with a gradual increase in speed toward the east. In this case, slightly more particles were exported through the Gulf's mouth (47%) than in the isobaric experiment at 763 m (42%) (Table 2). However, the transit times are similar in both isobaric and isopycnic cases, showing that the Socotra Passage is the faster advective route to RSOW export to the open ocean. A detailed analysis of this route is presented in the next sections based on EXP-RSOW-SIGMA.

4.3. Spreading in the Arabian Sea of particles released in Red Sea outflow area from EXP-RSOW experiments

In the previous sections, it has been shown that GLORYS12 reproduces relatively well the climatological seasonal cycle of the RSOW and essential characteristics of the mid-depth circulation in the Gulf of Aden as measured during the REDSOX. Let us now look at the probability distributions (Section 4.3.1), spreading patterns (Section 4.3.2), and transit times (Section 4.3.3) of the outflow particles in the Arabian Sea based on the long-term simulations.

In the normal-year simulations (except at 27.6σ_θ), all advected particles visited the Arabian Sea at some point in their lifetime, and very few (0.1%) were in the Gulf when the simulation ended. In the EXP-RSOW-SIGMA-93, which is based on the 1993–2018 daily velocity fields and initial conditions of 1993, the results were similar (Table 2). In all long-term simulations, no particle arrived in the Arabian Sea through the Socotra Passage at 27.6σ_θ (Table 2).

4.3.1. Probability distributions

Fig. 11 shows probability distributions of particle positions for the normal-year isopycnic (a, d) and isobaric (b, e) simulations after 100 years. The patterns are similar. The outflow particles tend to concentrate along the western boundary south of 22° N. But, a considerable number (10%–20%) also reach the northern (Gulf of Oman) and the eastern side of the Arabian Sea (Fig. 11a–b). Despite fewer particles arriving on the east, the likelihood of the northeastern Arabian Sea (north of 14° N) to be visited by a particle originated in the outflow area is not much lower than the western boundary (Fig. 11d–e). Based on more energetic eddy field, EXP-RSOW-SIGMA-93 gives similar probability distributions (Fig. 11c, f). These facts taken together point to a robust recirculation in the eastern side of the basin (few particles visiting multiple times the same area). Indeed, the seasonal quasi-Eulerian mean circulation maps calculated from the virtual particles

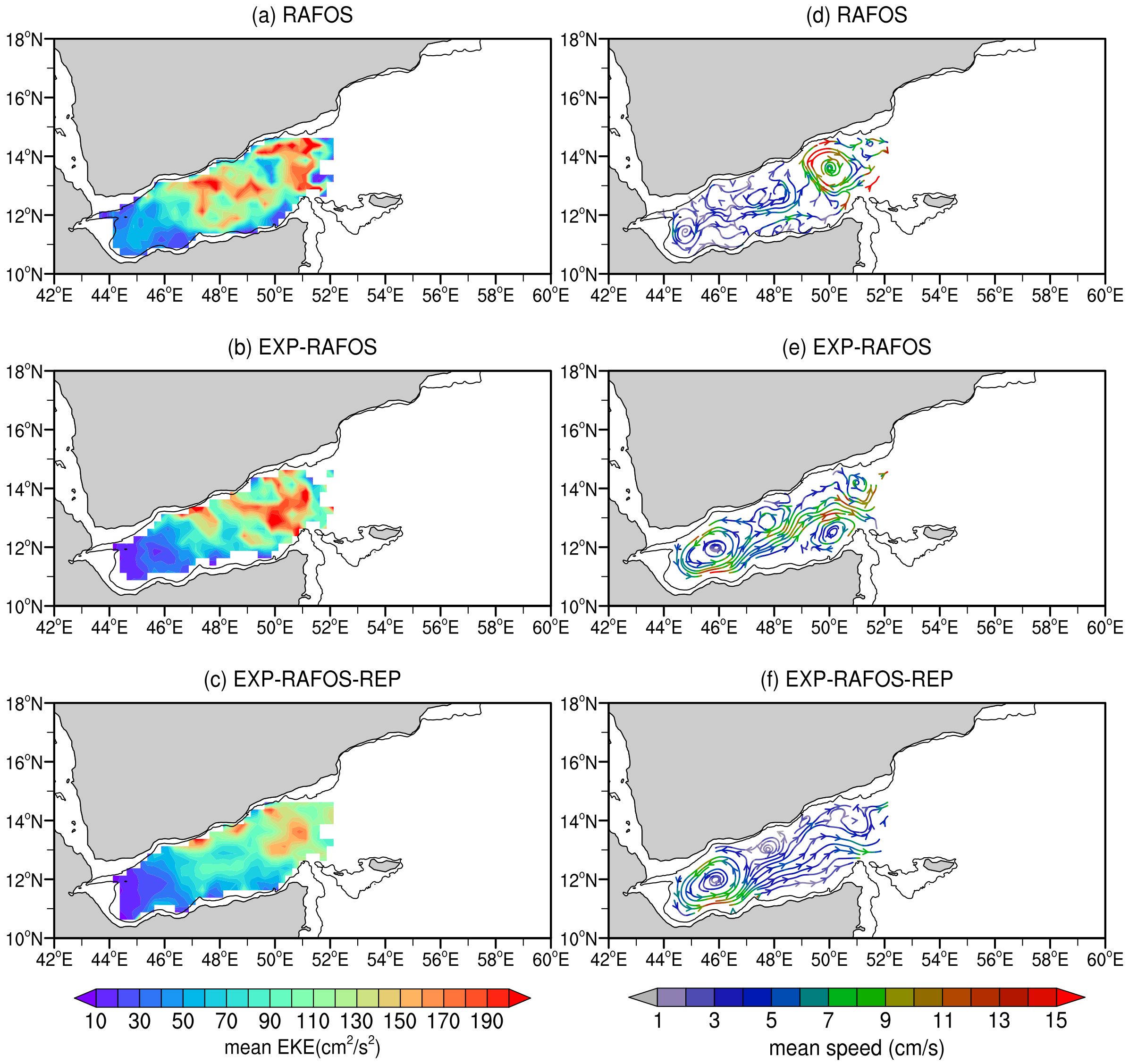

Fig. 9. Quasi-Eulerian mean eddy kinetic energy (EKE) (a–c) and mean current speeds (d–f) calculated from trajectories of the RAFOS and two isobaric simulations at 763 m (EXP-RAFOS and EXP-RAFOS-REP). Black contour is the 700 m isobath from ETOPO2. EXP-RAFOS and EXP-RAFOS-REP fields are only plotted where RAFOS is defined. (For interpretation of the references to color in this figure legend, the reader is referred to the web version of this article.)

show large-scale gyres on the eastern side. In winter, there is an anticyclonic (clockwise) gyre centered at about 14° N–66° E (Fig. 12a, c, e). In summer, there is a cyclonic gyre on the northeastern side (north of 14° N) with a northward current along the eastern boundary and another cyclonic gyre at about 10° N–64° E (Fig. 12b, d, f). These features also appear in the Eulerian mean velocity fields computed directly from GLORYS12 outputs (not shown). On the western side, mesoscale eddies dominate the mean circulation, and EKE is highest (not shown).

A diagonal line across the basin separates the areas of high (reddish) and low (green) probabilities in Figs. 11d–f. This line extends off Somalia from about 8° N–52° E to the eastern boundary at 14° N–74° E. Less than 5% of the particles reached the region south of this line (Figs. 11a–c). Consequently, most particles that visited the north and central-eastern basins exited the Arabian Sea off Somalia, not through India's southern tip.

Three areas of enhanced probability can be identified in the long-term simulations (Fig. 11a–c). The main area is along the eastern side of the Socotra toward the south and then along the western boundary (off Somalia). The second area is oriented northeastward along the Yemeni–Omani coast. The third area connects the western to the eastern basins in the central Arabian Sea between 14° N and 18° N. The latter is more evident in the normal-year isopycnic simulation. As a matter of fact, particles are more likely to reach east of 60° E (north of 12° N) along isopycnic than isobaric surfaces. In general, the isopycnic surfaces in the RSOW layer deepens from the Gulf of Aden to the Arabian Sea interior (Figure S12). For instance, the $27.3\sigma_\theta$ is around 650 m in the Gulf of Aden and deeper than 763 m (the deepest surface at the isobaric simulations) in the eastern Arabian Sea.

Compared with the other two long-term simulations, the EXP-RSOW-SIGMA-93 probability map has larger features. For instance, the northeastward path along the Yemeni–Omani coast is not narrow as in EXP-RSOW-SIGMA and EXP-RSOW. Also, the link between the western and eastern basins in the central Arabian Sea. Despite that, the probability maps for particles from the outflow area are qualitatively alike in the Arabian Sea for the three long-term simulations, even if a strong eddy field is considered as in EXP-RSOW-SIGMA-93.

No significant difference exists if probabilities are computed based only on particles released in winter (Figure S13) or summer (Figure S14). Consequently, the RSOW pathways in the Arabian Sea are not directly linked to the seasonal variability of the circulation in the outflow area. But, they are affected by the seasonal changes in mid-depth

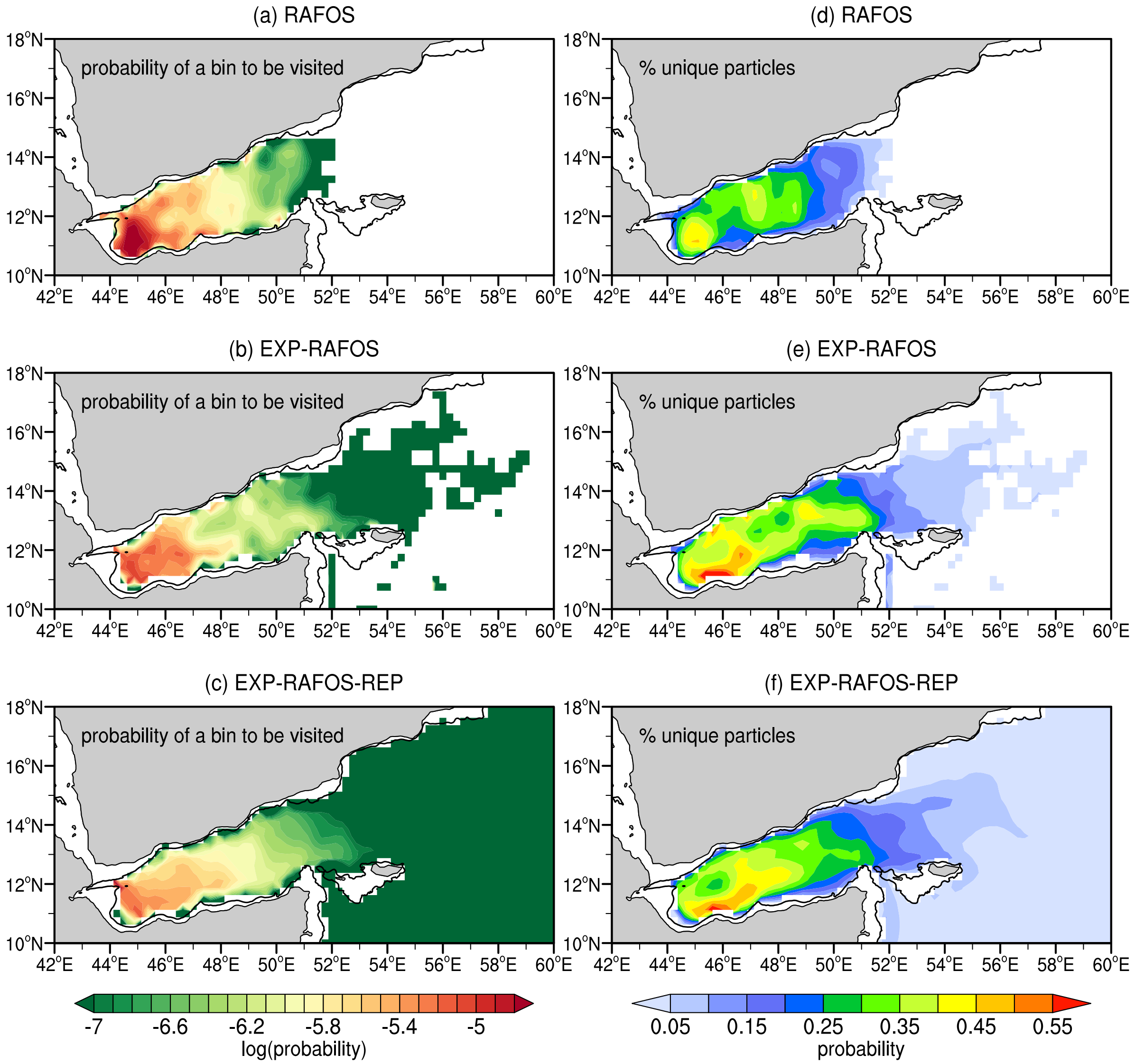

Fig. 10. Probability distributions (histograms) of particle positions based on the RAFOS observations and virtual particles from two isobaric simulations at 763 m (EXP-RAFOS and EXP-RAFOS-REP). (a–c): P_{multi} the probability of a bin to be visited by a virtual particle or float, including multiple visits. (d–f): P_{unique} the likelihood of an individual particle/float visits a specific bin (particles/floats are counted once). Black contour is the 700 m isobath from ETOPO2.

currents in the Arabian Sea. Fig. 13 shows the probability distributions of particle positions based on wintertime and summertime positions. These maps reflect the most probable areas where the particles are in each season, respectively. To highlight the differences, the probabilities are given in relation to the total number of particle positions. Particles are likely to be off Socotra-Somalia in winter (Fig. 13a, c; for the sake of conciseness, only isopycnic simulations are shown). In summer, particles tend to be off Yemen–Oman (Fig. 13b, d).

In addition to the three areas described above, the outflow particles also escape the Gulf of Aden via the Socotra Passage, as previously described. It is hard to see this path on the maps shown in Fig. 11 in which all particles are taken into account together. But, this path emerges when the probability maps are calculated individually for different vertical levels. The Socotra Passage pathway is constrained by the bathymetry and more common at 27 kg/m^3 (Figs. 14a and S15a) and 541 m (Fig. 14d). At these shallow levels, between 15%–30% of the outflow particles escape the Gulf of Aden via the Socotra Passage (Table 2). At the short-term EXP-RAFOS simulations, there were many more particles exported through this pathway. However, the particles in these simulations were released over the entire Gulf and not just within the outflow region as at EXP-RSOW experiments. As will be shown later, the Socotra Passage route is seasonal, occurring in winter.

In contrast with the Socotra Passage, the eastern Socotra route is more noticeable at 27.3σ_θ at the RSOW core (Figs. 14b, e, and S15b). Most of the outflow particles that contour eastern Socotra crossed the Gulf's mouth (southern side). Indeed, the Gulf's mouth is the main path for particles exiting the Gulf of Aden for all long-term simulations, independent of their destination in the Arabian Sea (Table 2).

In the deep RSOW levels (27.6 kg/m^3 and 763 m), the western–eastern connection at the central Arabian Sea is highlighted (Figs. 14c, f and S15c), particularly at EXP-RSOW-SIGMA-93. In the isopycnal case, it is visible a returning route south of 14° N (Figs. 14c, and S15c). Section 4.4 will discuss the individual pathways in detail.

For the sake of conciseness, hereafter, this study focuses on the isopycnal simulations, particularly the normal-year. The reason is twofold. First, the observed RSOW spreads along isopycnal surfaces within a well-defined layer in the Arabian Sea (and beyond) as described by several studies in the literature (e.g., Beal et al., 2000; L'Hégaret et al., 2021). Second, the derived pathways and transit times of the three simulations are not qualitatively different.

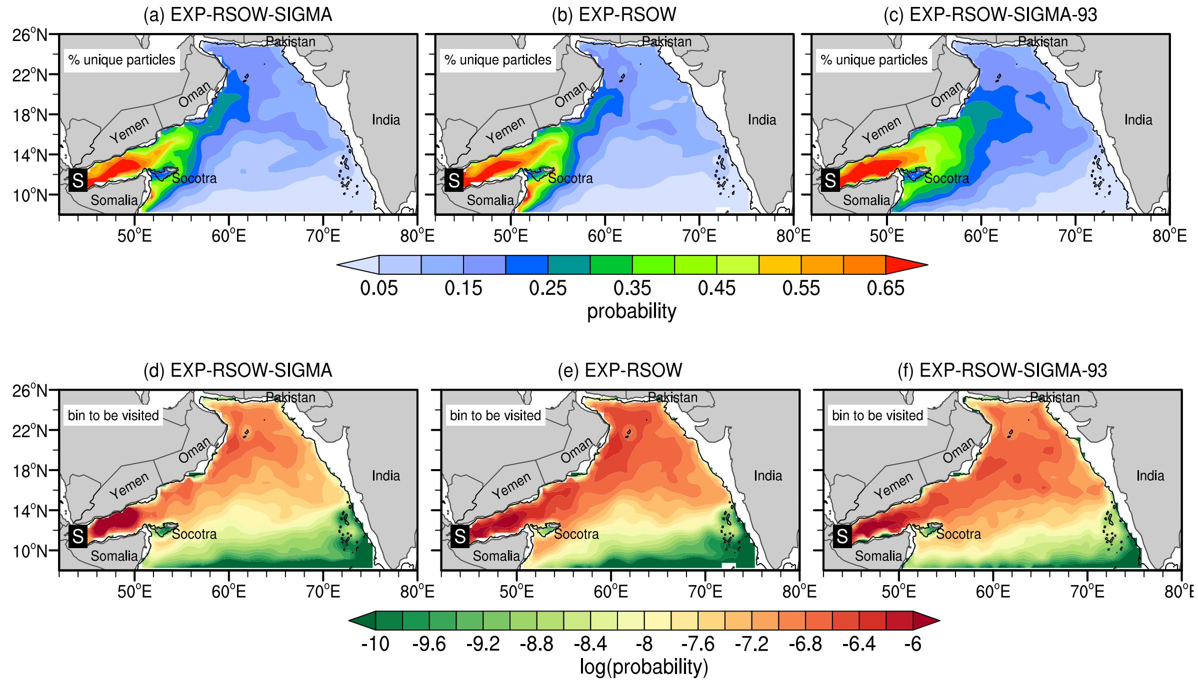

Fig. 11. Probability distributions of particle positions in the Arabian Sea based on the long-term simulations: (a, d) EXP-RSOW-SIGMA (σ_θ = 27, 27.3 and 27.6 kg/m^3); (b, e) EXP-RSOW (z = 541, 644 and 763 m), and (c, f) EXP-RSOW-SIGMA-93 (σ_θ = 27, 27.3 and 27.6 kg/m^3). (a–c): P_{unique} the likelihood of an individual particle visiting a specific bin during its lifetime (particles are counted once per bin). (d–f): P_{multi} the probability of a bin to be visited by a virtual particle, including multiple visitations. Black contour is the 700 m isobath from ETOPO2. The black rectangle shows the source region (S) where the particles were released (the outflow area). EXP-RSOW-SIGMA probabilities are based on 35,989 particles, and EXP-RSOW on 40,077 and EXP-RSOW-SIGMA-93 on 35,551 (see text for details). (For interpretation of the references to color in this figure legend, the reader is referred to the web version of this article.)

4.3.2. Spreading pattern

Fig. 15 shows the spreading pattern in the Arabian Sea for isopycnal particles released in winter in the outflow area for the EXP-RSOW-SIGMA experiment. After only one year, particles have spread over the entire Gulf of Aden, with many exported to the Arabian Sea. There are already clear pathways western and eastern Socotra toward the western boundary off Somalia. Some particles have followed northeastward off Yemen–Oman, but none have reached the Gulf of Oman or the eastern Arabian Sea. After two years, particles were advected further northeastward, reaching 22° N, but only after three years, they reached the Gulf of Oman, in the extreme north.

It took about 4–5 years for particles starting to move to the eastern boundary south of 22° N, with a pathway at the central Arabian Sea (14° N–18° N) emerging during this period. Also noticeable is the eastward spreading of particles south of 12° N up to 66° E. In the subsequent years, the particles spread southward very slowly along the eastern boundary. Even after nine years of release, very few particles reached the southeastern corner of the Arabian Sea (8–14° N; 60–76° E) in agreement with the low probability of particles reaching this region (Fig. 11). As time passes, the route through the Socotra Passage (western) fades, indicating that this path is the fastest way out of the Gulf of Aden for the outflow-originated particles.

If the particles released in summer are plotted, the overall spreading pattern is similar to those described above (Figure S16). Exceptions are observed off Somalia in the western boundary: the Socotra Passage route is not well defined for summer-released particles; and, the particles are much more dispersed in the western boundary (off Somalia), especially for the first two years of releasing. As will be shown later, the Socotra Passage route is seasonal. In short, on the western side, the particles are advected fast because mid-depth currents and EKE are relatively strong and slowly advected in the eastern Arabian Sea, where currents and EKE are weak and well-defined recirculation gyres are present (Fig. 12).

In the EXP-RSOW-SIGMA-93 (not shown), particles tend to disperse faster than in the normal-year simulation, such that particles cover most of the Arabian Sea in three years. As before, the Socotra Passage pathway fades off after two years, and few particles reach the southeastern corner in nine years.

4.3.3. Transit times

The transit time statistics obtained from TTD at each grid point quantify the assessments above. In the normal-year isopycnal simulation, it takes about six months for outflow-originated particles to spread over the entire Gulf of Aden and one to two years to be exported along the western boundary both southward toward Somalia and northeastward, off the Yemeni–Omani coast (Fig. 16a). The most frequent transit times are not significantly different for particles released in winter and summer (Fig. 16d–g). In contrast, reaching the eastern boundary takes longer. North of 14° N, the most frequent time is around 10–15 years, and at the southeastern side (8–14° N; 60–76° E) about 20–25 years (with mean of 35–40 years). Thus, it is no surprise that the latter region is mostly empty on the dispersion sequence shown in Fig. 15.

Depending on the pathway, particles can arrive much faster or take longer to reach the same destinations. In consequence, the mean transit times are larger than the most frequent (Fig. 16a–b). Despite that, the spatial distributions of both statistics are similar.

The fastest advective time and the smallest standard deviation are on the Arabian Sea's western side, in the Gulf of Aden, and off the Yemeni–Omani coast (Fig. 16c–i). In the Arabian Sea interior, the standard deviation is large, around 20–25 years. Hence, the RSOW can often ventilate (bring oxygen) to the western Arabian Sea but not the eastern. The RSOW holds higher oxygen concentrations as it has been more recently in contact with the atmosphere (in the northern Red Sea) than the oxygen-depleted mid-depth waters of the Arabian Sea.

If the TTD statistics are calculated based on EXP-RSOW-SIGMA-93, the spatial patterns are similar to EXP-RSOW-SIGMA. The fastest arrival times are in the western basin: the Gulf of Aden, off Yemen–Oman, and Somalia. The slowest arrivals are found in the southeastern corner near India's southern tip. The differences between TTD statistics from

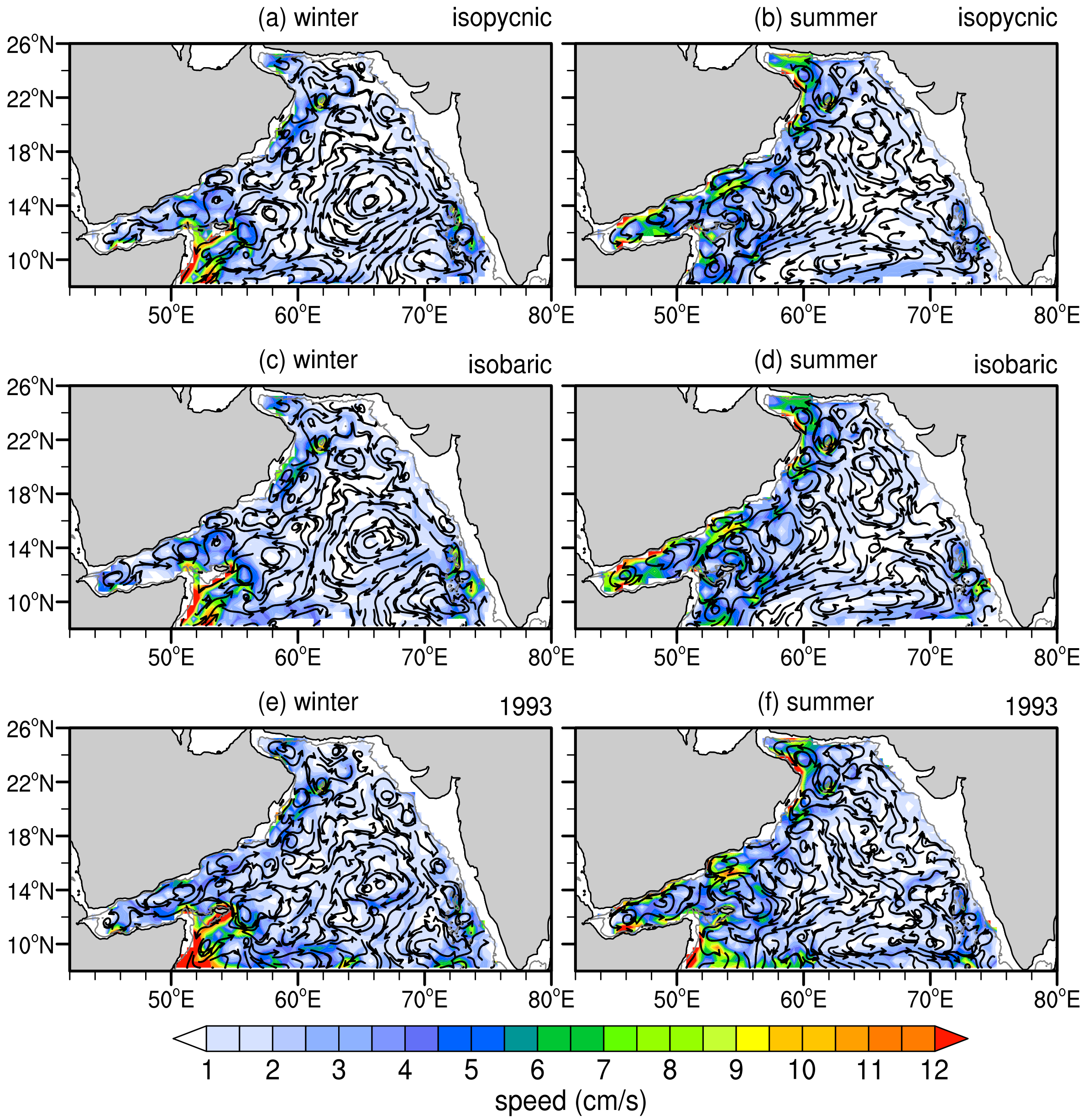

Fig. 12. Quasi-Eulerian mean circulation at the RSOW layer in winter (December to March) and summer (June to September) based on: (a–b): EXP-RSOW-SIGMA simulation; (c–d) EXP-RSOW; (e–f): EXP-RSOW-SIGMA-93. Black contour is the 700 m isobath from ETOPO2.

EXP-RSOW-SIGMA-93 and EXP-RSOW-SIGMA indicate similar transit times in the western basin south of 18° N, although mesoscale eddies are more energetic at the former. The differences in transit times (most frequent and mean) in this region are less than one year (Fig. 17a–b). However, for EXP-RSOW-SIGMA-93, particles take more time to reach north of 18° N along the western boundary (about 5–10 years more). It also takes much more time for particles to arrive at the southeastern corner near the Indian southern tip (Fig. 17a).

Overall, EXP-RSOW-SIGMA-93 presents lower mean transit times and standard deviations (Fig. 17a). These results suggest that mesoscale eddies are important for spreading RSOW to the Arabian Sea interior given shorter timescales, but interannual variability cannot be dismissed in this experiment.

4.4. Outflow originated particles in the Arabian Sea: connectivity and preferential pathways

Fig. 18 summarizes the connectivity of the outflow originated particles in the Arabian Sea for the long-term isopycnal simulations. From the total, 8% (EXP-RSOW-SIGMA) and 2% (EXP-RSOW-SIMGA-93) of particles were never exported out of the Gulf of Aden. These Gulf resident particles occurred at $27.6\sigma_\theta$.

In both simulations, more than half of the outflow-originated particles spent their lifetime within the western basin domain (west of 63° E). However, a significant portion of particles (more than one-third) visited the central-eastern Arabian Sea (east of 63° E), indicating advective pathways toward the eastern boundary. Moreover, about 20%–25% of the outflow particles were advected to the extreme north along the Yemeni–Omani coast. They reached the Iranian–Pakistani slope in the eastern boundary through this northward route.

The main export route for RSOW out of the Gulf of Aden was via the Gulf's mouth. This route accounted for 80%–82% of the particles. In contrast, only 12%–16% of the outflow particles were exported through the Socotra Passage, and mostly at $27\sigma_\theta$ (Table 2). Indeed, much more particles reached the Somali continental slope crossing the Gulf's mouth, and then through eastern Socotra—about half of the particles followed this route on their way to the south.

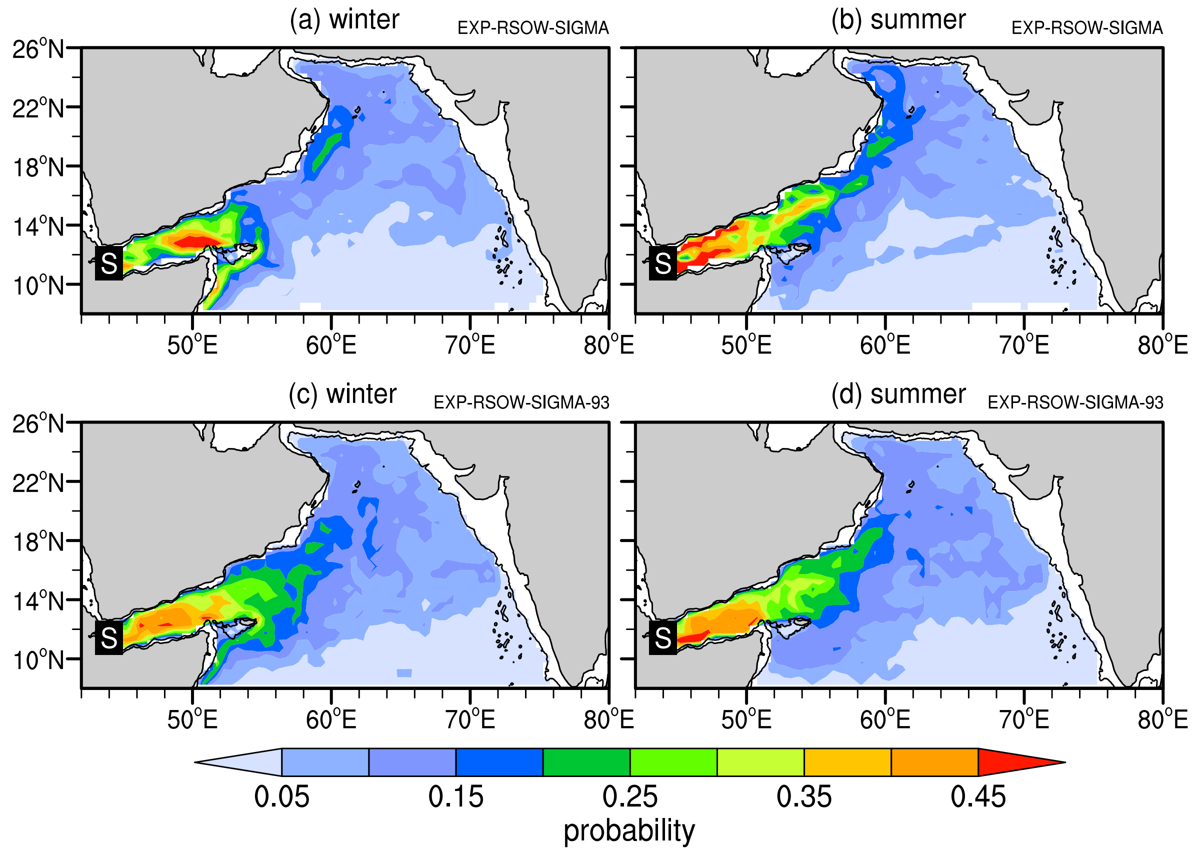

Fig. 13. Probability distributions of particle positions (P_{unique}) in the Arabian Sea based on the long-term isopycnal simulations for winter (December to March) and summer (June to September). The maps express the likelihood of an individual particle to be at a specific bin in winter and summer, respectively (particles are counted once per bin). Black contour is the 700 m isobath from ETOPO2, and black rectangle shows the source region (S) where the particles were released (the outflow area). Probabilities are given in relation to the total advected particles in each experiment (35,989 for EXP-RSOW-SIGMA and 35,551 for EXP-RSOW-SIGMA-93).

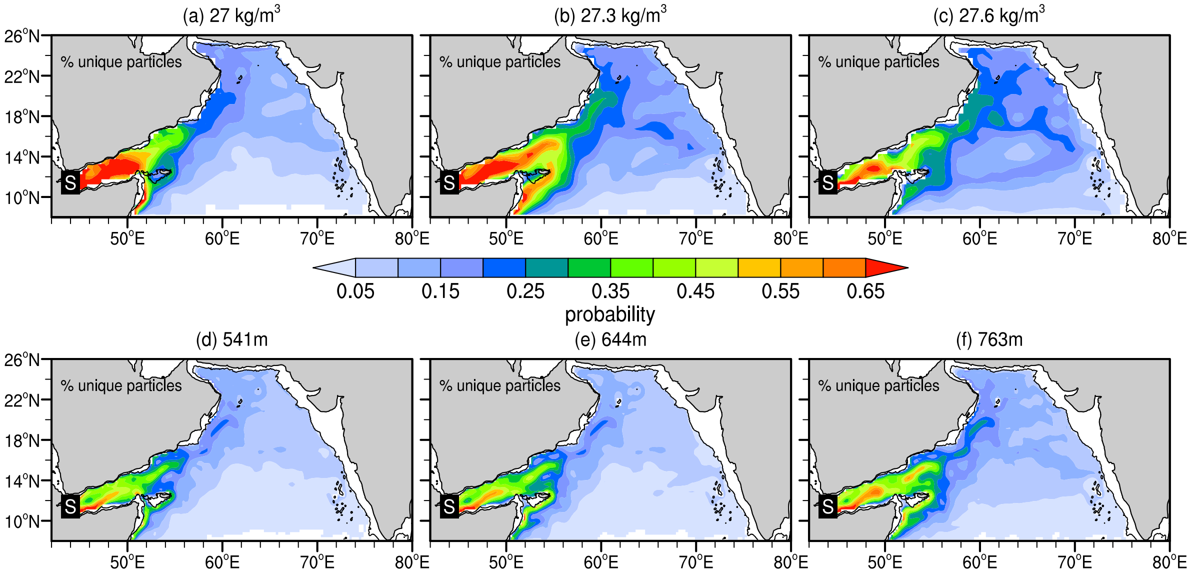

Fig. 14. Probability distributions of particle positions in the Arabian Sea at different isopycnics (a–c) and depth levels (d–f) within the RSOW layer from EXP-RSOW-SIGMA and EXP-RSOW, respectively. The colors express the fraction of individual particles visiting a particular bin (particles are counted once per bin). Black contour is the 700 m isobath from ETOPO2, and the black rectangle shows the source region (S) where the particles were released (the outflow area). (For interpretation of the references to color in this figure legend, the reader is referred to the web version of this article.)

In GLORYS12, the preferred route for outflow particles in the Arabian Sea was off Somalia. About 70%–80% of the particles reached the Somali Undercurrent domain (8° N–9° N; 50° E–54° E), while only 3%–4% reached the southern tip of India (8° N–9° N; 72° E–78° E).

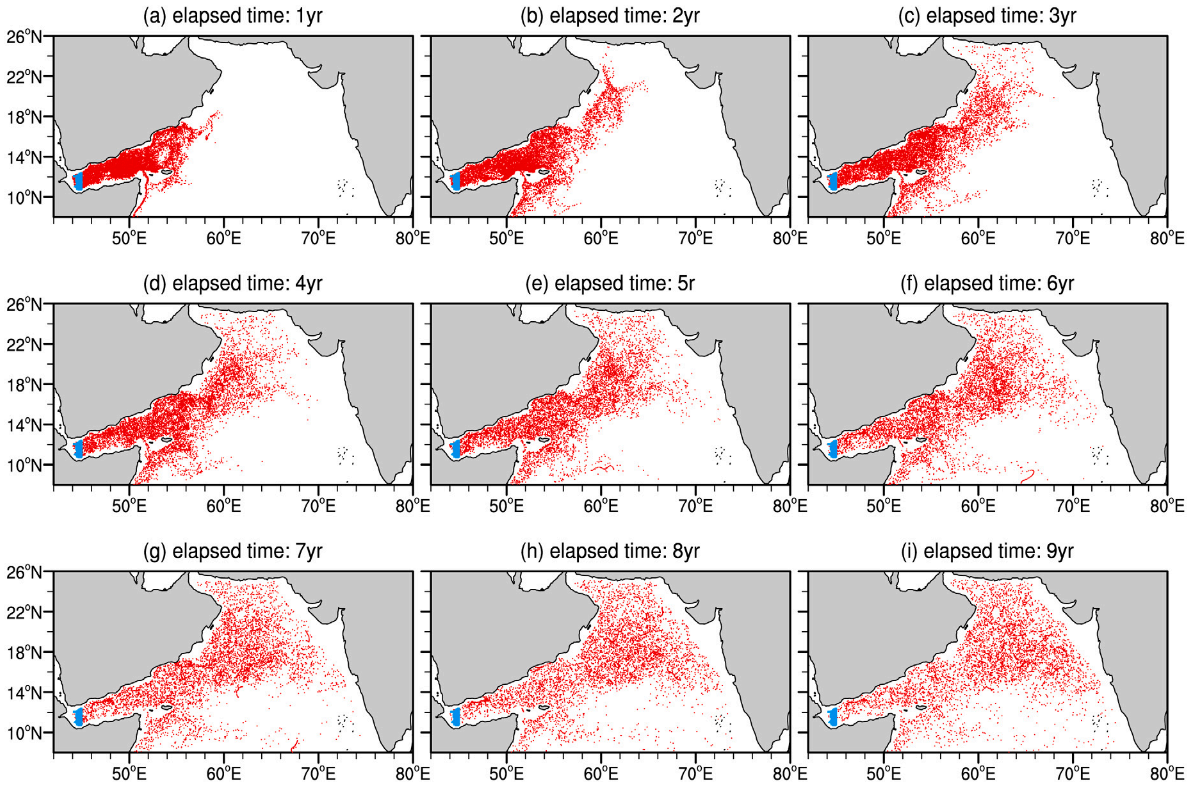

Fig. 15. Time evolution of outflow-originated particles in the Arabian Sea for the first ten years based on the EXP-RSOW-SIGMA simulation. The particles were released in winter (December–March). Blue dots show the particles' positions at the initial times, and red dots after (a) one to (i) nine years, respectively. (For interpretation of the references to color in this figure legend, the reader is referred to the web version of this article.)

For characterizing the different pathways in the Arabian Sea, disjoint subsets of particle trajectories were selected based on the analyses above. The formed subsets accounted for 81% of all simulated EXP-RSOW-SIGMA trajectories (73% in EXP-RSOW-SIGMA-93) and were defined as follow:

(a) Crossed the Socotra Passage and reached the Somali Undercurrent domain (8°–9° N; 50°–54° E) [11.6% of all trajectories in EXP-RSOW-SIGMA and 12.0% in EXP-RSOW-SIGMA-93]. Hereafter, the Socotra Passage Pathway

(b) Crossed the Gulf's mouth, stayed during the entire simulation in the southwestern Arabian Sea (<23° N; <63° E) and reached the Somali Undercurrent domain [42.8% of all trajectories in EXP-RSOW-SIGMA and 33.6% in EXP-RSOW-SIGMA-93]. Hereafter, the Southwest Pathway

(c) Crossed the Gulf's mouth, visited the northwestern Arabian Sea (23°–26° N; 56°–63° E) and reached the Somali Undercurrent domain [14.9% in EXP-RSOW-SIGMA and 12.5% in EXP-RSOW-SIGMA-93]. Hereafter, the Northwest Pathway

(d) Crossed the Gulf's mouth, visited the southeastern Arabian Sea (<23° N; > 63° E), but not the tip of India, and reached the Somali Undercurrent domain [8% in EXP-RSOW-SIGMA and 11.2% in EXP-RSOW-SIGMA-93]. Hereafter, the Central Pathway

(e) Crossed the Gulf's mouth, did not visit the Somali Undercurrent domain, and reached the southern tip of India (8°–9°; 72°–78° E) [1.9% and 2.0% in EXP-RSOW-SIGMA-93]. Hereafter, the Eastern Pathway

(f) Crossed the Gulf's mouth, reached the Somali Undercurrent domain, and visited the southern tip of India (8°–9°; 72°–78° E) [1.8% and 1.3% in EXP-RSOW-SIGMA-93]. Hereafter, the Southern Pathway

Fig. 19 gives an overview of these pathways for the EXP-RSOW-SIGMA simulation. Maps for EXP-RSOW-SIGMA-93 are very similar for the Southwest and Northwest pathways, but the Southern pathway is not well defined in EXP-RSOW-SIGMA-93 (not shown). Hereafter, the focus is on the EXP-RSOW-SIGMA for the sake of conciseness. This choice was dictated by the main objective of this study—to draw a clear picture of the preferred advective RSOW pathways with reduced influence of interannual variability.

4.4.1. Socotra Passage pathway

The Socotra Passage is constrained by bathymetry (maximum depth ≤1200 m) and is very narrow in the RSOW layer (≈50 km). This export pathway out of the Gulf of Aden is more prominent for the upper RSOW (Table 1). While 30% of the exported particles crossed through the Socotra Passage at $27\sigma_\theta$ in EXP-RSOW-SIGMA, none crossed at $27.6\sigma_\theta$. A similar pattern was observed for EXP-RSOW-SIGMA-93.

In EXP-RSOW-SIGMA, the Socotra Passage is also the fastest way out of the Gulf of Aden, with the most frequent transit time being only four months at $27\sigma_\theta$ (Table 1), although the mean value is around two years (Fig. 20d). If only particles released in winter are taken into account, the most frequent time (1.5 years) is closer to the mean value (Fig. 20d, gray bars). In both cases, about 50% of particles took less than two years to reach the passage and 65% less than three years. Only 5% of the particles took more than five years to reach the Socotra Passage.

After crossing the Socotra Passage, almost all particles (99.7%) in EXP-RSOW-SIGMA followed to 8° N attached to the continental slope (Fig. 20a, blue trajectories). They were advected southward by the Socotra and Somalia Undercurrents. The particle density map shown in Fig. 20b reflects this behavior with more than 95% of the Socotra particles hugging the continental slope. Few particles (0.3%), however, followed a more convoluted pathway (Fig. 20a, gray trajectories). They were first southward advected by the Socotra and Somalia Undercurrents but recirculated back to the Socotra Passage into the Gulf of Aden to be finally exported east of Socotra. This recirculation is associated with the seasonal reversion of the mid-depth currents (Fig. 21c–d).

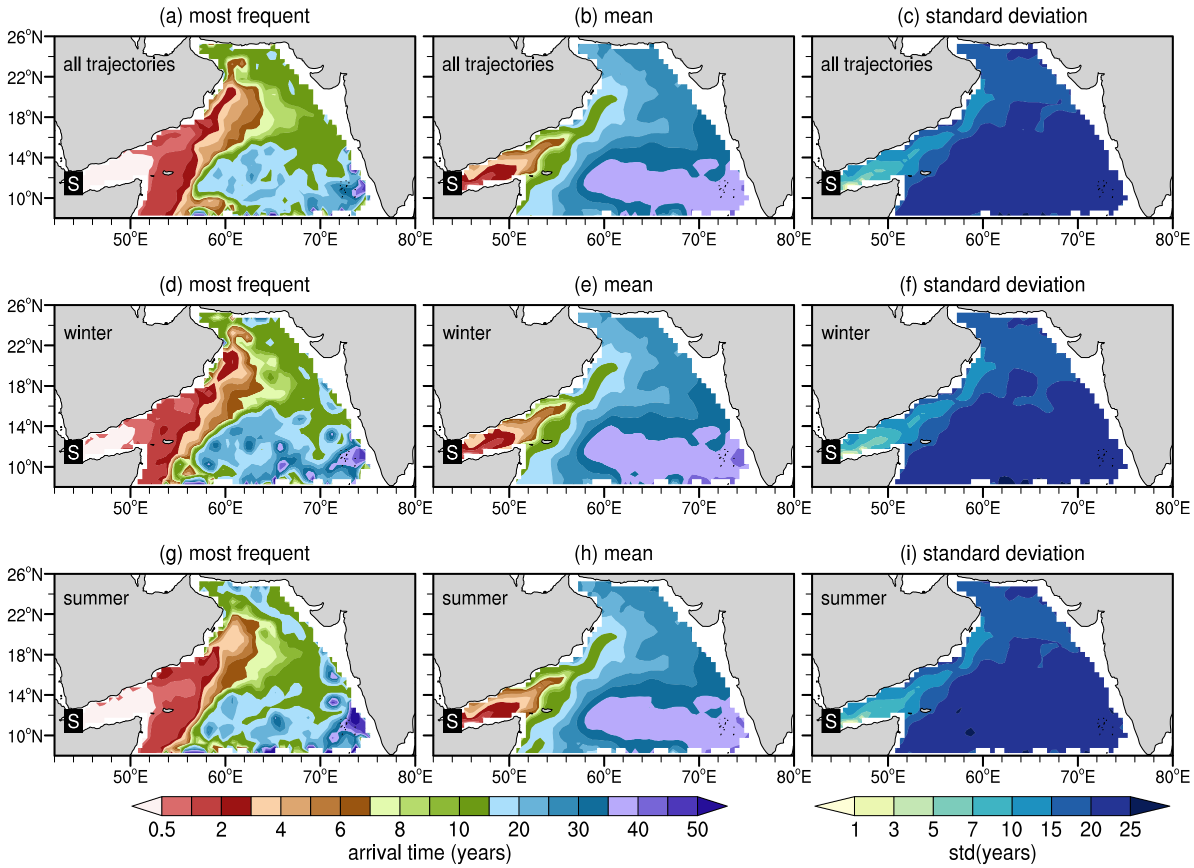

Fig. 16. Transit times in the Arabian Sea for outflow-originated particles based on the EXP-RSOW-SIGMA simulation. The first column shows the most frequent transit time in years (modal value), second column the mean transit time, and the third column the respective standard deviation. The top row is based on all synthetic trajectories, second and third rows in particles released in the winter (December–March) and summer (June–September). The black rectangle shows the source (S) region of released particles.

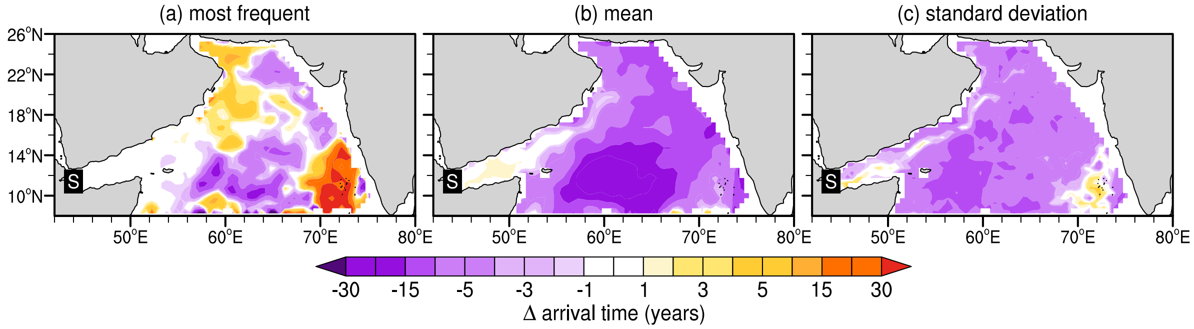

Fig. 17. Transit time differences between EXP-RSOW-SIGMA-93 and EXP-RSOW-SIGMA simulations for (a) most frequent transit time in years (modal value), (b) mean transit time, and (c) standard deviation. The black rectangle is the source (S) region of released particles. Differences were calculated as EXP-RSOW-SIGMA-93 minus EXP-RSOW-SIGMA. Negative values mean EXP-RSOW-SIGMA-93 is faster than EXP-RSOW-SIGMA and positive otherwise.

In summer, the circulation is toward the Gulf of Aden in the Socotra Passage, with a relatively strong northward current (maximum of 35 cm/s). Northeastward currents are also observed in eastern Socotra. In winter, the main undercurrents reverse in the Arabian Sea. In the Socotra Passage, mid-depth flow is out of the Gulf of Aden, flowing into a strong southwestward Somali Undercurrent.

The particles with convoluted trajectories cross the Socotra Passage in late winter/spring and reach the Somali Undercurrent in early summer. This period is when the regional circulation reverts from predominantly southwestward to northeastward. Fig. 21a shows an example of this kind of trajectory. The particle, released in March, arrived in the Socotra Passage one year later. Then, it was advected southward by the Socotra and Somali Undercurrents. By the end of spring, the large-scale mid-depth circulation reversed, and the particle detached from the continental slope to form an anticyclonic (clockwise) loop centered at 8.75° N–52.5° E. After looping, the particle was advected northwestward, back toward Socotra Passage, crossing the passage in late summer (September). The particle was then advected out of the Gulf of Aden, reaching eastern Socotra in February when the circulation reverted again to southwestward. Other particles followed a similar pattern, with more/less convoluted trajectories (Fig. 20a, gray trajectories).

In contrast, the particles with straightforward trajectories along the Somali continental slope arrive in the Socotra Passage in winter when the currents are predominantly southwestward (independent of releasing time). Fig. 20b shows a two-dimensional histogram of the seasonal distribution of particles that crossed Socotra Passage in relation to the releasing and (first) crossing months. Almost all particles crossed

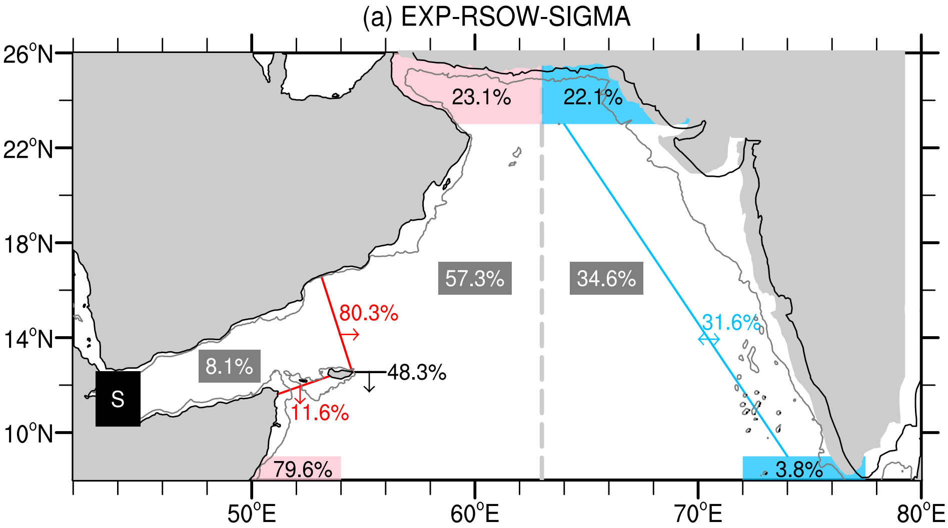

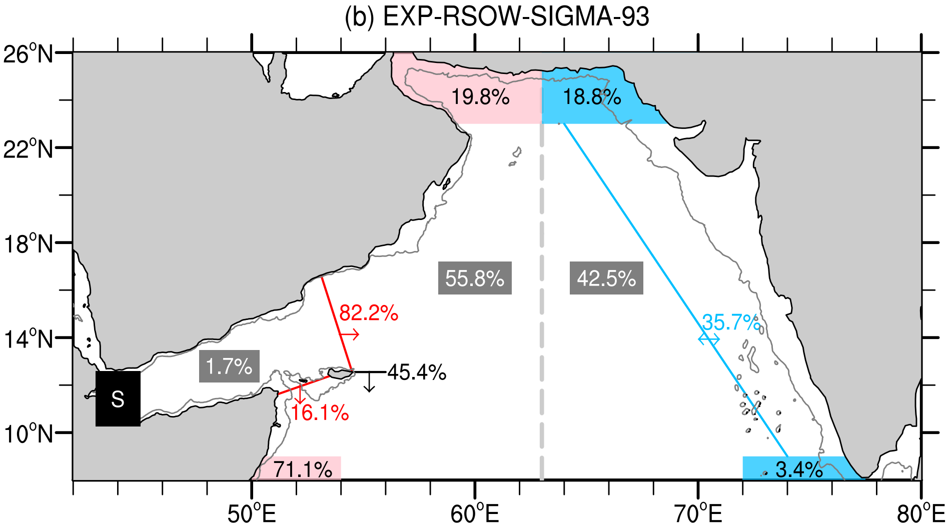

Fig. 18. RSOW connectivity in the Arabian Sea from the EXP-RSOW-SIGMA and EXP-RSOW-SIGMA-93 simulations. All percentages are reported to the total of particles advected from the source region (35,989 and 35,551 respectively; black box). The three gray rectangles show, respectively, the percentage of particles that never went out of the Gulf of Aden in 100 years, the exported Gulf of Aden particles that stayed in the western Arabian Sea (west of 63° E), and particles that reached the eastern Arabian Sea crossing the gray dashed line in the mid-basin. The two red lines in the Gulf of Aden outflow indicate the percentage of particles that (first) crossed the respective lines (Gulf of Aden's mouth and the Socotra Passage). The black line, eastern of Socotra, indicates the particles that crossed that line and reached the Somali Undercurrent region (8° N–9° N; 50° E–54° E). The four boxes (red and blue) show the number of particles that crossed the respective box. The blue line in the eastern Arabian Sea indicates the number of particles that reached the eastern boundary crossing the line. Gray contour is the 700 m isobath from ETOPO2. (For interpretation of the references to color in this figure legend, the reader is referred to the web version of this article.)

the Socotra passage in winter (November–March), predominately in January–February. The few particles that crossed in April and June are the ones with the convoluted trajectories described above.

4.4.2. Export via the Gulf's mouth and pathways

Unlike the export via the Socotra Passage, in which almost all particles follow southward off Somalia in winter, the export through the Gulf of Aden's mouth happens year-round based on the EXP-RSOW-SIGMA simulation, but with a preference for spring to late summer (Fig. 22a). These preferences agree with the probability maps shown in Fig. 13 in which particles are more likely to be off Yemen–Oman in summer than winter.

While the Gulf's mouth is the main advective export route for the outflow particles, it is the only route at the 27.6σ_θ (Table 2). The most frequent advective transit time —from the particle's initial positions to the Gulf's mouth—increase with isopycnal deepening within the RSOW layer, from six months to about three years (Table 2).

The particles crossing the Gulf's mouth follow different pathways in the Arabian Sea, albeit most particles will end up in the Somali Undercurrent domain (8° N–9° N; 50° E–54° E). Fig. 19 shows five advective pathways calculated from the adjoining subsets previously described. The most common is the Southwest Pathway (about 43% of all trajectories). Particles, in this case, are advected through eastern Socotra and then southward off Somalia until 8° N (Fig. 19a). This route was followed by particles crossing the Gulf's mouth year-round, but it was more frequent for particles that arrived there in April and August (Fig. 22b). Most particles that follow the Southwest Pathway route were at 27 and 27.3σ_θ (Fig. 19a, inset).

The second most common pathway for particles crossing the Gulf's mouth is the Northwest Pathway (15% of the trajectories), mostly at 27σ_θ and 27.3σ_θ. In this case, particles are advected northeastward along the Yemeni–Omani coast, reaching the Gulf of Oman north of 23° N. A large fraction of these particles cross to the eastern boundary off Iran and Pakistan, but return to the western Arabian Sea, to follow southward also off Yemeni–Omani coast. They are then advected eastern Socotra and southward off Somalia to 8° N (Fig. 19b). The particles

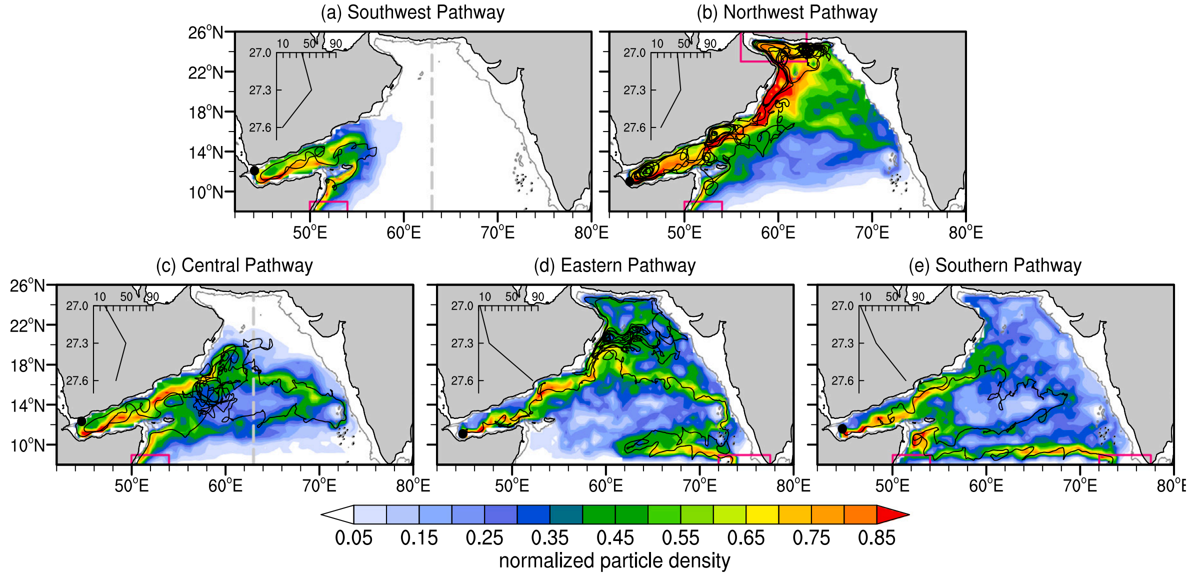

Fig. 19. Main pathways in the Arabian Sea for particles exported through the Gulf of Aden's mouth based on the EXP-RSOW-SIGMA simulation. Color shows the normalized particle density (fraction) at 0.5° grid. The number of particles at each bin (only the first visit is counted) is normalized by the number of particles following the specific pathway. Inset vertical profiles over the Arabian Peninsula indicate the percentage of particles (horizontal axis) per isopycnal level (vertical axis in kg/m^3). Dashed gray line marks the 63° E meridian and pink boxes indicate the western, northern, and southern regions used to select the subsets (see text for details). Black curves show a typical trajectory for the respective subset. The gray contour is the 700 m isobath from ETOPO2. (For interpretation of the references to color in this figure legend, the reader is referred to the web version of this article.)

following the Northwest Pathway crossed the Gulf's mouth mainly in April–May and August (Fig. 22c).

In the Central Pathway (Fig. 19c), particles follow an anticyclonic circulation in the central Arabian Sea. First, they flow northeastward off Yemen–Oman up to 18°–20° N. Particles, then, turn to the eastern Arabian Sea in a slanted route (from 18° to 14° N), which correspond to the enhanced probability area in Figs. 11a–b and 14a–c. South of 14° N, they return to the western boundary, east and south of Socotra, where they flow southward off Somalia to 8° N. Particles in this pathway are most likely to cross the Gulf's mouth on spring (Fig. 22d), and there is a significant contribution (34%) of particles at $27.6\sigma_\theta$ (Fig. 19c, inset).

The two less common pathways are the Eastern (Fig. 19d) and the Southern (Fig. 19e) that account for 1.9% and 1.8% of the total trajectories, respectively. Predominantly, they occur at $27.6\sigma_\theta$. Very few particles followed these pathways at $27\sigma_\theta$ (Fig. 19d–e, inset).

After crossing the Gulf's mouth, particles in the Eastern Pathway are advected northeastward along the Yemeni–Omani coast until 20° N, where a bifurcation exists. Near this latitude, many particles flow eastward in the central Arabian Sea (14°–18° N), similar to the Central Pathway described above. The remaining particles continue northward off the Omani coast, reaching the Gulf of Oman, north of 23° N. They form an anticyclonic gyre with particles advected southward along the Pakistani slope. These particles return to the western boundary at 20° N, where they follow the same eastward route in the central Arabian Sea (14°–18° N). When reaching the eastern, at 14° N, the particles flow southward, hugging the Indian slope until 12° N. Then, particles do a cyclonic offshore excursion (up to 62° E) before reaching the southern tip of India at 8° N. Particles that followed the Eastern Pathway did not return to the Somali Undercurrent domain in 100 years. They preferentially crossed the Gulf's mouth in January and August (Fig. 22e), but the histogram of seasonal distribution is much nosier than for the other pathways.

In the Southern Pathway, the particles crossing the Gulf's mouth are first advected southward or northeastward along the Yemeni–Omani coast. Particles following northeastward, veer at 18° N to the east, and follow an anticyclonic gyre like in the Central Pathway (Fig. 19e). In the present case, however, the particles do not often reach the Indian continental slope. From the eastern Arabian Sea, particles are transported back to the west, toward the south of Socotra. Once south of Socotra, particles follow southward off Somalia independent of the route taken after crossing the Gulf's mouth.

Contrasting with the previous pathways, the particles in the Southern Pathway are much dispersed off Somalia and not attached to the slope. In reaching the southwestern boundary at 8°–9° N, particles are then advected eastward across the basin to India's southern tip. In the Southern Pathway, particles are more likely to cross the Gulf's mouth in April and August (Fig. 22f).

A common characteristic for all pathways described above is that particles follow them independently of the releasing time in the outflow area (Fig. 19).

4.4.3. Freshening along the pathways

Fig. 23 shows the salinity dilution for the main pathways described above (also based on the EXP-RSOW-SIGMA simulation). The along-trajectory anomalies used to generate those maps are relative to the salinity at the particle's initial positions. However, the reanalysis does not capture the high salinity in the westernmost Gulf of Aden (<46° E). Thus, the maps underestimate the freshening strength there —anomalies are near zero, or even slightly positive in Fig. 23. Therefore, it is more accurate to take the salinity differences in Fig. 23 as the freshening relative to about 46° E rather than in relation to the RSOW input into the Gulf of Aden. Despite this limitation, the salinity anomaly maps give a zero-order description of the RSOW dilution in the Arabian Sea.

In addition to being the fastest export route out of the Gulf of Aden, the Socotra Pathway is also the pathway with the lowest freshening in the region off Socotra and Somalia (Fig. 23a). Modal values indicate a reduction of 0.5 in salinity in the Socotra Passage relative to the outflow area and 0.6–0.7 off Somalia, with freshening increasing southward. Mean salinity anomalies have similar values and spatial distribution (Figures S17). The standard deviation at each bin in the Socotra Pathway is low (Figure S18).

For the Southwest, Northwest, and Central Pathways, the freshening is slightly higher off Somalia (0.65–0.75) than for particles following the Socotra Pathway (Fig. 23b–d). There are a few regions with freshening anomalies around 0.8–0.85 in the Northwest and Central

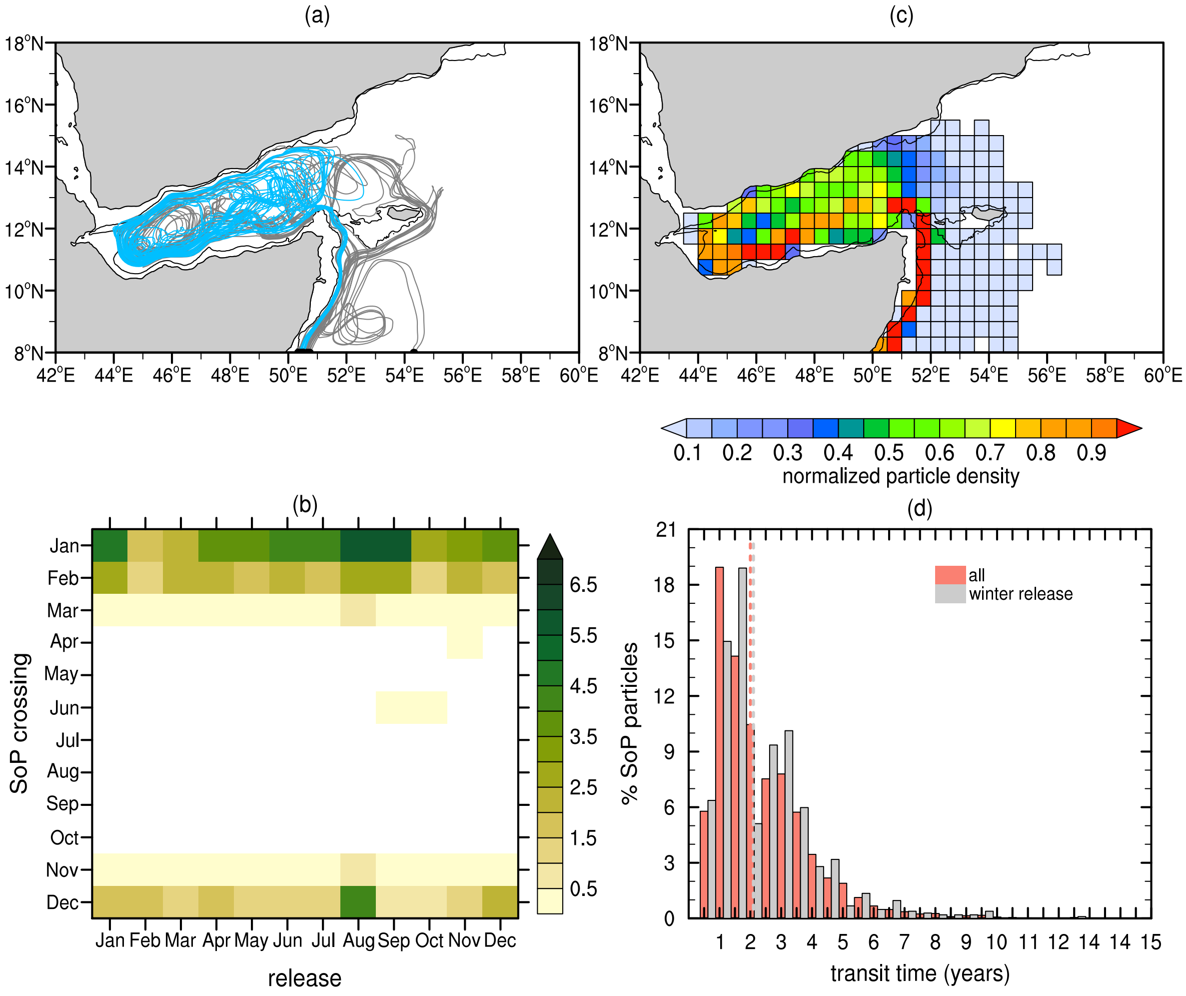

Fig. 20. The Socotra Passage pathway at EXP-RSOW-SIGMA simulation. (a) Examples of trajectories that follow this route. Gray is used for particles that recirculate eastern Socotra after being exported through the Socotra Passage into the western boundary. Blue is used for non-recirculating particles. In the map, there are 21 blue and 13 gray trajectories plotted. (b) Seasonal distribution of particles in function of releasing month and Socotra Passage first-cross. Color shows the percentage of particles in relation to the total number of particles that crossed the Socotra Passage (4170). White indicates no particle. (c) Normalized particle density (fraction) at 0.5° grid computed for the subset of particles that crossed the Socotra Passage. The number of particles at each bin (only the first visit is counted) is normalized by the total number of particles that crossed the Socotra Passage. (d) Transit time distribution for crossing the Socotra Passage. Pink is used for all particles and gray for particles released in winter (December–March). Dashed lines show the respective mean values. Black contour in the maps is the 700 m isobath from ETOPO2. (For interpretation of the references to color in this figure legend, the reader is referred to the web version of this article.)

Pathways. The standard deviation offshore Somalia is also much higher, with values as high as 1.5–2 in the Southwest Pathway (Figure S18).

In the Northwest Pathway, particles following northeastward off Yemen–Oman to the Gulf of Oman present a spatially homogeneous freshening, with a modal value of 0.65 (Fig. 23c) and a mean of 0.5–0.55. However, in the mean, some spatial structure is noted (Figure S17c).

As the particles are advected eastward, mixing with fresher Arabian Sea ambient waters is more likely to occur. Therefore, the largest freshening is found in the eastern basin for particles following the Central, Eastern, and Southern Pathways (Fig. 23d–f; Figure S17d–f). The latter two have the highest standard deviations (1.8–2.9; Figure S18e–f), indicating that isopycnal mixing along these pathways is variable.

If particles are separated into released in winter and summer, the (modal and mean) salinity anomaly maps for these seasons are similar to the ones shown in Fig. 23, except that the overall freshening is slightly reduced in summer than winter (0.05–0.1). Also, the standard deviation is enhanced for particles released in summer (Figure S19) than in winter (Figure S20).

4.5. Observational evidence from Argo trajectories

The previous sections have described the preferential advective pathways for the outflow particles in the Arabian Sea based on three long-term Lagrangian simulations. A pertinent question is whether there is observational evidence for these paths. The trajectories derived from Argo floats provide an insight into this matter. One should keep in mind that the Argo trajectories dataset in the Arabian Sea is still insufficient to calculate unbiased statistics such as the seasonal-mean velocity fields. The float positions on a monthly basis are relatively small, and their spatial distribution is skewed to the eastern Arabian Sea (see, e.g., figures in L'Hégaret et al., 2021; de Marez et al., 2019). The latter has received most floats in the last few years as access to the western Arabian Sea is challenging due to piracy and other geopolitical issues. In the Somali Current System, the Argo deployments have been sparse.

Also, in this study, there was no attempt to calculate probability distributions from Argo displacements. The reason was to avoid confusion with the results of the Lagrangian simulations. By definition, Argo-based probability maps would not reflect the preferential paths of outflow originated particles as the Argo initial positions are scattered over the basin and skewed to the eastern Arabian Sea. Instead, the

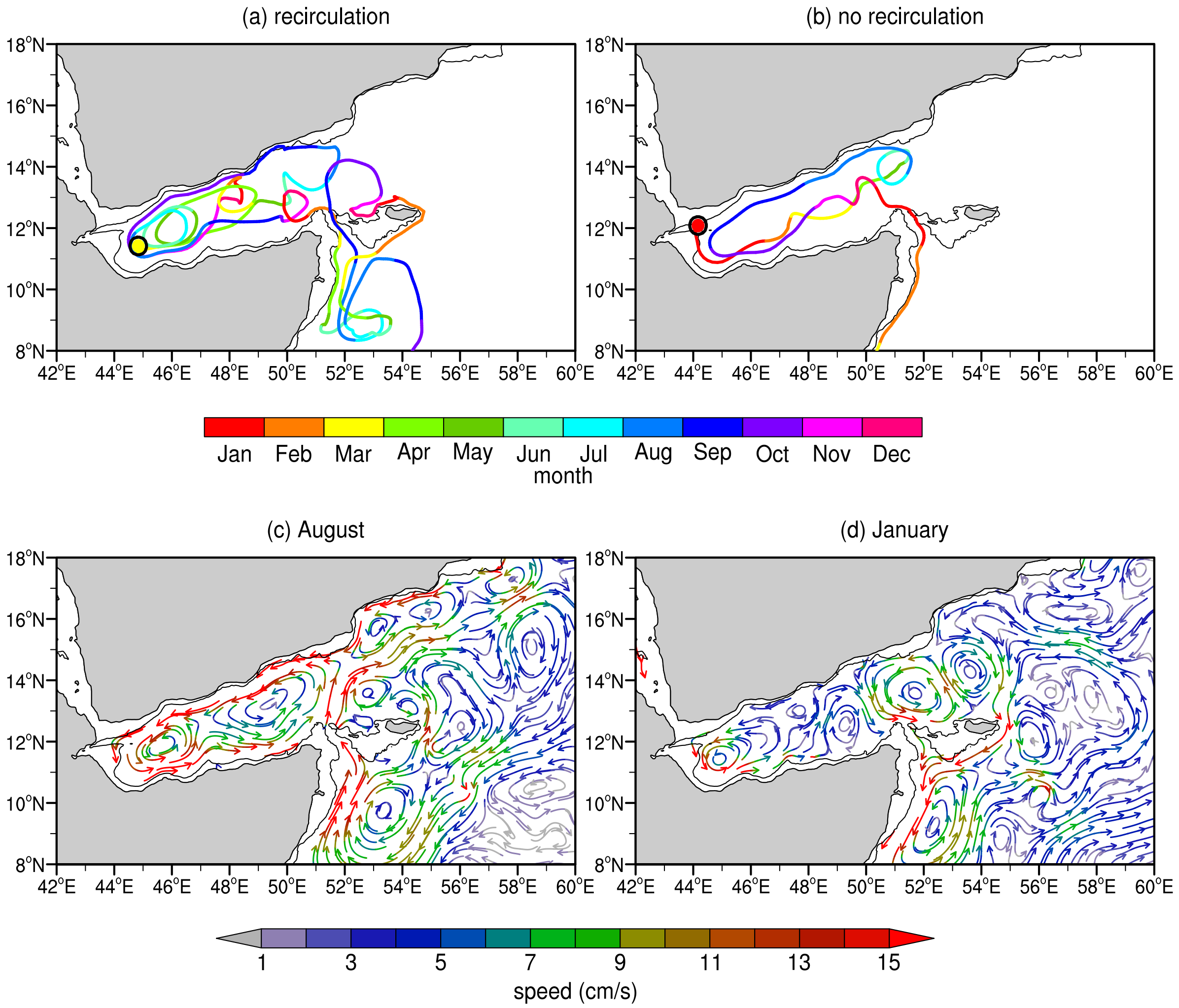

Fig. 21. Trajectories of two particles released at σ_θ 27 kg/m^3 in the outflow area for the EXP-RSOW-SIGMA simulation (a–b) and GLORYS12 climatological circulation (Eulerian mean) at the same isopycnal for August (summer) and January (winter). In (a–b): dot shows the initial position, dot's color the releasing month, and trajectories are colored by time progression (months). In (c–d): vectors indicate the direction and color the speed velocity. Black contour is the 700 m isobath from ETOPO2. (For interpretation of the references to color in this figure legend, the reader is referred to the web version of this article.)

Argo trajectories over the last 18 years were visually inspected to find examples of the pathways revealed by the Lagrangian simulations.

Fig. 24 shows a subset of 30 Argo trajectories that follow some of the pathways described in the previous sections. Individual float information can be found in the supplementary material. For the sake of clarity, only this subset is shown, but there are more examples found in the Argo database. From the 32 floats deployed in the Gulf of Aden with more than 100 days, eleven have been exported to the Arabian Sea (about 34%). Their trajectories are displayed in Figs. 24a–d. Two of these floats are still active as in early August 2021 –the pink in Fig. 24a and the purple in Fig. 24b. These floats have been collecting data over the last 2.4 yr (March 2019-to present), consistent with time scales determined from the Lagrangian simulations.

All the eleven floats deployed within the Gulf of Aden were exported through the Gulf's mouth, agreeing with the Lagrangian simulations that revealed that Gulf's mouth rather than the Socotra Passage is the main export route to the Arabian Sea at intermediate-depths. Several floats, without doubt, followed the Southwest Pathway, contouring eastern Socotra and reaching the Somali Undercurrent domain. Figs. 24c–d show five of such trajectories, but there are many other examples in the Argo database. In contrast, the inspection of all Argo trajectories did not disclose any float advected southward through the Socotra Passage (Socotra Passage Pathway). Possibly because the southward Socotra route is phase-locked and the number of floats released in the Gulf over 18 years was small.

However, several examples of floats deployed in the Somali Undercurrent and crossing the Socotra Passage toward the Gulf of Aden were found. Fig. 24h show two of these trajectories (dark red and yellow, respectively). Both floats were deployed in the Somali Undercurrent in summer (July–August) when the regional mid-depth circulation is predominantly northward. Their trajectories agree with the Eulerian mean circulation for August (Fig. 20c). Another example is the purple trajectory in Fig. 24d. The float deployed in the Gulf's mouth followed the Southwest Pathway toward the Somali Undercurrent domain. But, as the circulation reverses direction, the float was advected northwestward to the Socotra Passage, much like the simulated trajectory shown in Fig. 20a.

The Lagrangian simulations indicated that it takes more than seven years for outflow-originated particles to reach the northwestern and the eastern Arabian Sea (Fig. 16a–b). These transit times are more than the typical lifetime of an Argo float (about 3–5 years). Thus, it was not surprising that none of the floats deployed in the Gulf of Aden have made these far areas following the four longer pathways (Northwest, Central, Eastern, and Southern). However, several Argo trajectories deployed outside the Gulf have displacements that bear a resemblance to some portion of these pathways. Take, for example, the pink and orange eastward trajectories plotted in Fig. 24g. They seem to have

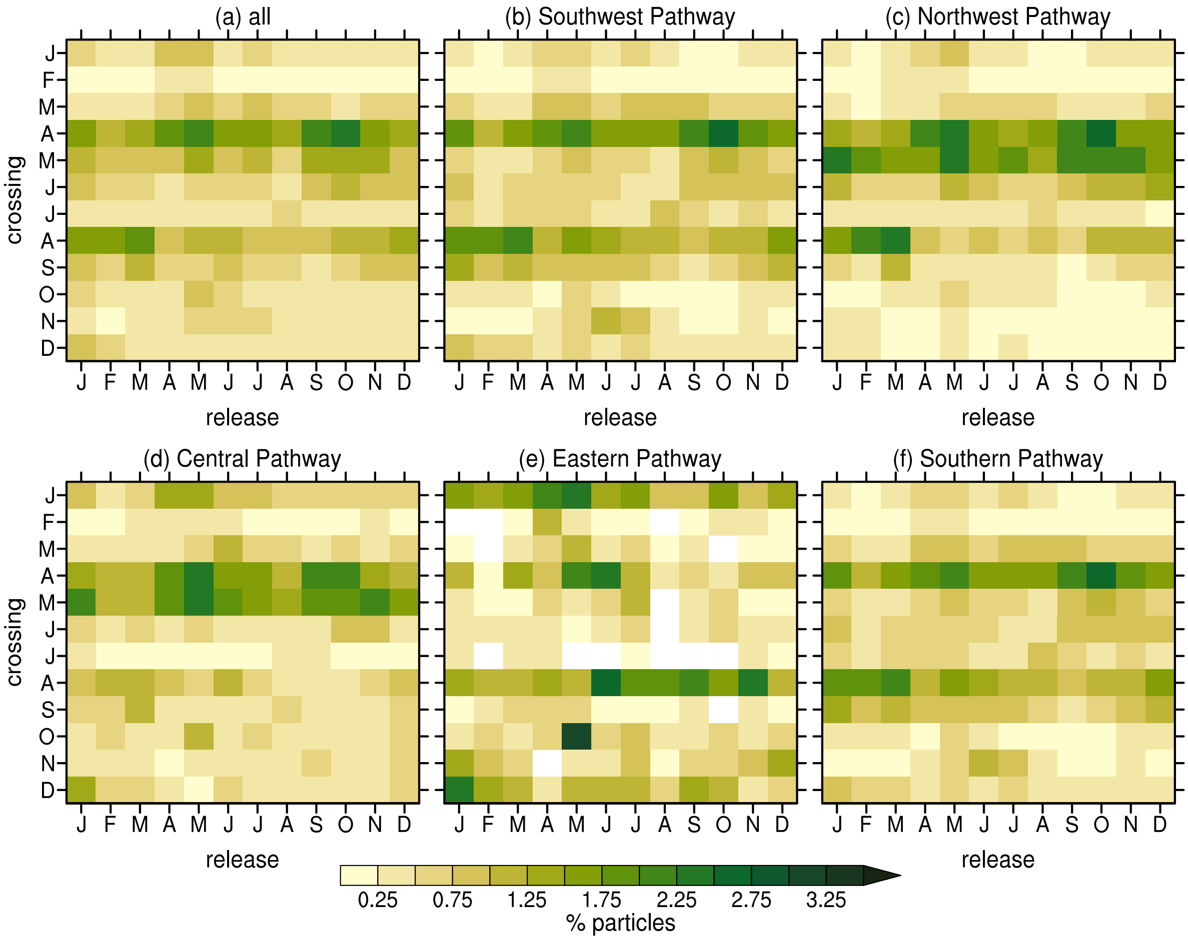

Fig. 22. Seasonal distribution of particles in function of releasing month and Gulf of Aden's mouth first-cross: (a) all particles and (c–f) main RSOW pathways in the Arabian Sea (see Fig. 19). Color shows the percentage of particles in relation to the respective total subset. White indicates no particle. (For interpretation of the references to color in this figure legend, the reader is referred to the web version of this article.)

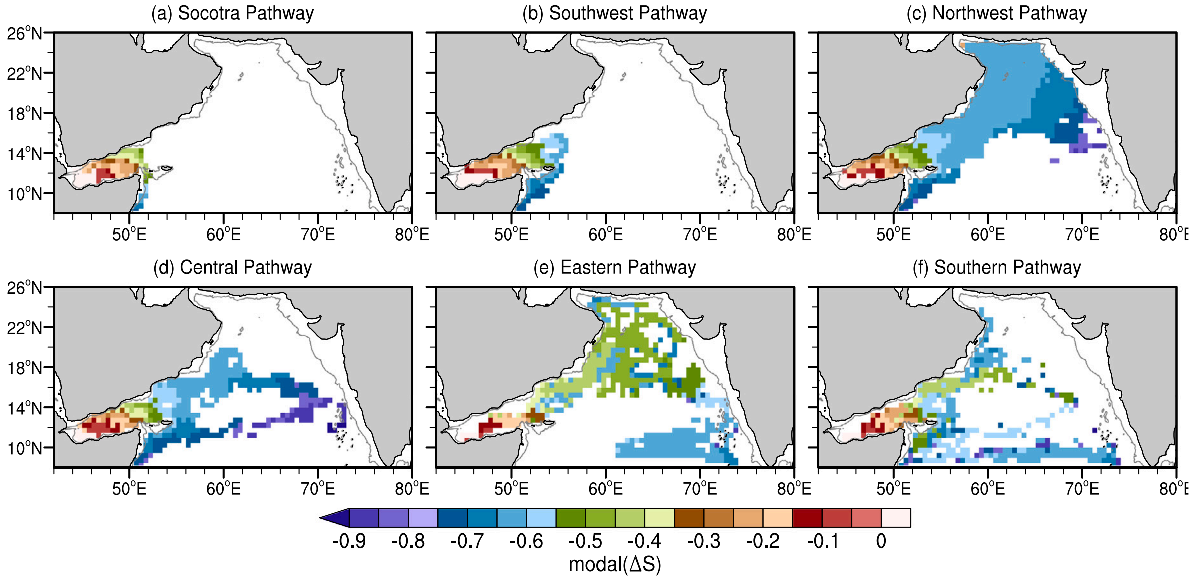

Fig. 23. Salinity dilution at the main RSOW pathways based on the EXP-RSOW-SIGMA simulation. Color indicates the most frequent salinity anomalies (modal value) at each 0.5° bin for bins with probability larger than 0.35 (see Fig. 19). Anomalies are relative to the salinity at the particle's initial positions. The gray contour is the 700 m isobath from ETOPO2. (For interpretation of the references to color in this figure legend, the reader is referred to the web version of this article.)

traced the southern limb of the Eastern or Southern Pathways shown in Figs. 19d–e, respectively.

Collectively, trajectories in Figs. 24b, 24f (blue and purple), and 24g (purple and blue) are likely a fingerprint of the Northwest Pathway.

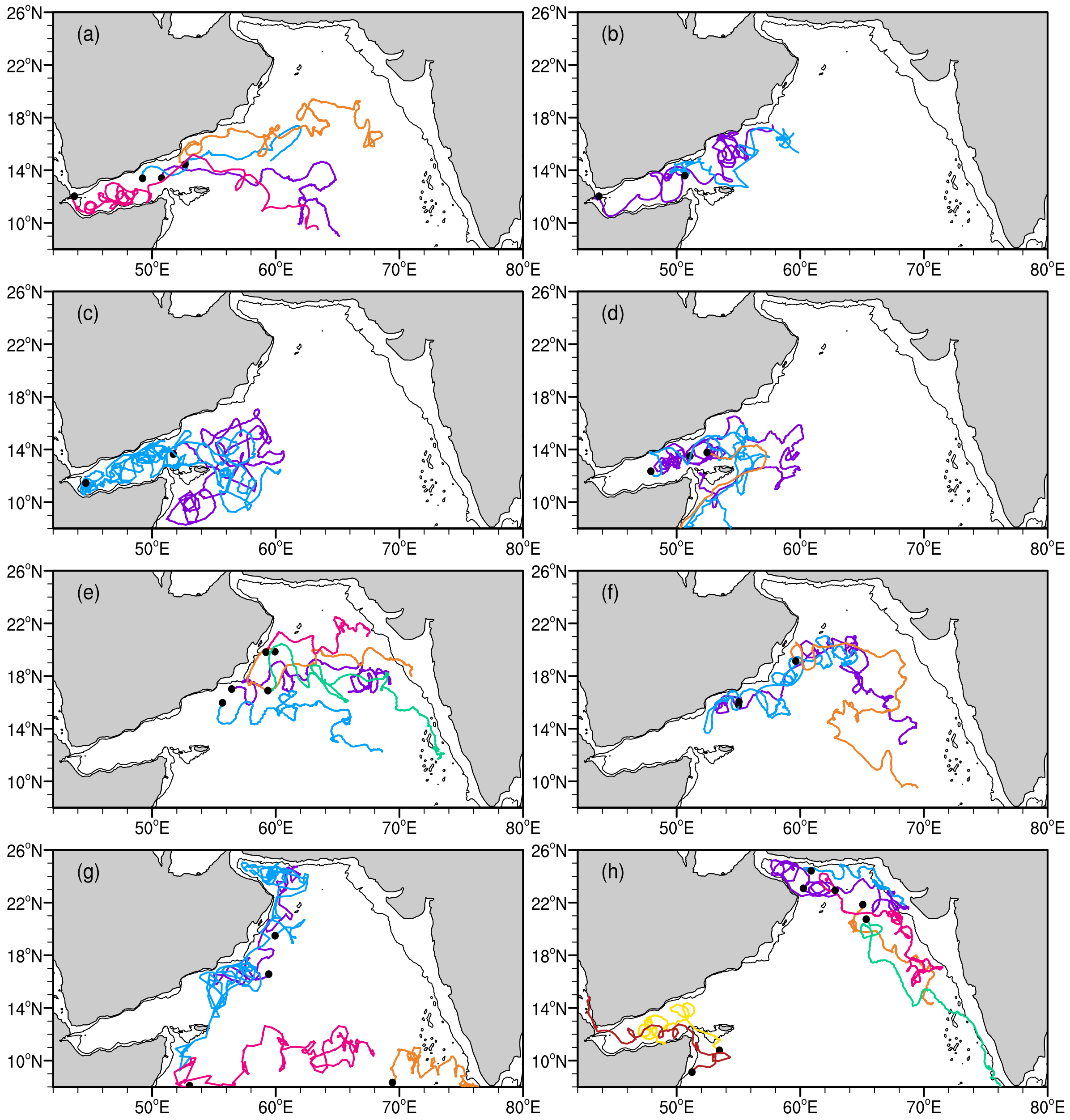

Fig. 24. Thirty Argo trajectories in the Arabian Sea. (a–d) shows the eleven floats deployed in the Gulf of Aden between 2004 and 2019 and exported to the Arabian Sea. (e-f) shows trajectories that follow an eastward path, which can be a fingerprint of the Central, Eastern and/or Southern Pathways. (g) shows trajectories that can be part of the Northwest Pathway (blue and purple) and the Southern Pathway (pink and orange). (h) shows trajectories (brown and yellow) that followed northward within the Socotra Passage (similar to the simulated trajectory of Fig. 21a) and several floats advected southward along the eastern boundary (blue, purple, pink, orange and green). Dots indicate the initial float position. Black contour is the 700 m isobath from ETOPO2. (For interpretation of the references to color in this figure legend, the reader is referred to the web version of this article.)

All floats were advected northeastward, parallel to the Yemeni–Omani coast. One of the floats (Fig. 24g, blue trajectory) after reaching the northernmost position (Gulf of Oman) have been advected southward to the Somali Undercurrent domain, similar to the Northwest Pathway in which there is a high probability of particles making this loop.

As in the Lagrangian simulations, a significative connection between the western and eastern basins at the central latitudes of the Arabian Sea can be seen in Argo trajectories (e.g., Figs. 24a, 24e and 24f). These floats may have followed the Central, Eastern, or Southern Pathways (Fig. 19). Similar to these pathways, some of the Argo deployed on the western side were advected southward after reaching the eastern basin (e.g., green trajectory in Fig. 24e). The southward advection along Pakistan–Indian continental slope is a robust feature of the intermediate-circulation and captured by many other Argo floats deployed in the eastern basin. Fig. 24h shows a few examples.

5. Discussion

The Lagrangian simulations uncovered six main advective pathways in the Arabian Sea for particles originating in the Red Sea outflow region. Fig. 25 summarizes these pathways schematically. As shown in the previous section, Argo trajectories offer some observational evidence for these pathways.

Compare the new picture with the schematics shown in Fig. 1, which is based on the occurrence of RSOW reported in the literature. There are many more paths to the Arabian Sea interior and the eastern boundary than previously described. This fact may be the root of why it is hard to infer the RSOW spreading pathways in the Arabian Sea, based solely on in situ hydrographic observations as in, e.g., Beal et al. (2000) and more recently L'Hégaret et al. (2021). The updated schematics based on the simulations reconcile the conflicting accounts of the RSOW in the Arabian Sea, as discussed below.

The simulations support the Socotra Passage as an important route for the RSOW export out of the Gulf of Aden in winter as directly measured by Schott and Fischer (2000). In the simulations and real ocean, the wintertime Socotra and Somali Undercurrents advect RSOW southward along the Somali continental slope in this route. In agreement with the measurements of Fischer et al. (1996) (weak RSOW signature within the Socotra Passage in summer) and Schott and Fischer (2000) (strong signature in winter), the simulations confirm that the Socotra Passage is mostly a wintertime pathway for the RSOW (e.g., Fig. 20b). Also, similar to the description of Schott and Fischer (2000) in which the southward flow of RSOW concentrated on the western part of the Socotra Passage, most particles were attached to the 700 m isobath on the western side of the passage.

Unlike the hypothesis of Schott and Fischer (2000), the Socotra Pathway was not the preferred route out of the Gulf of Aden for the particles originating in the outflow region in all simulations. Instead, the preferred route was the Southwest Pathway. In this route, particles are exported through the Gulf's mouth, contour the eastern Socotra, and then are advected southward along the Somali slope. Schott and Fischer (2000) also inferred this route, which appears in their schematics (their Fig. 13b), although they did not consider it the most important. High-salinity anomalies associated with the RSOW have been observed eastern of Socotra (e.g., Fischer et al., 1996; Carton et al., 2012), and the Southwest Pathway can explain these measurements. Several Argo trajectories follow this path.

Together, the Socotra and Southwest Pathways carried more than half of the outflow particles to the Somali slope. Particles were advected in these pathways independently of the season they were released. However, particles are more likely to arrive off Somalia in winter (e.g., Fig. 13) when the mid-depth regional circulation is predominantly southward. These findings agree with the previous analysis of Gamsakhurdiya et al. (1991) that found the seasonal cycle of currents rather than the outflow volume transport control the distribution of RSOW in the northwest Indian Ocean. Also, it is consistent with Beal et al. (2000) in which salinity off Somalia in the RSOW layer is higher in winter than summer. Although particles are more likely to reach the southwestern Arabian Sea in winter, about 15% of the released particles are there in summer, which can account for several summertime measurements reported in the literature (e.g., Beal et al., 2003; He et al., 2020; Chowdary et al., 2005). Here, as in Durgadoo et al. (2017), particles off Somalia in summer were affected by the formation of the deep-reaching Great Whirl. The particles were transported northward, explaining the north-oriented RSOW high-salinity signature off Somalia described by Quadfasel and Schott (1982). This summertime northward advection was also seen in many Argo floats.

Two main differences exist in the simulations for particles following the Socotra and Southwest Pathways. The former is the fastest way out of the Gulf of Aden (four months to about one year depending on the isopycnal) and has the weakest freshening (compared to the outflow area). These facts may explain why Schott and Fischer (2000) inferred the Socotra Passage is the main route since the T–S signature there is closer to the non-diluted RSOW.

There is no evidence that the RSOW splits into multiple branches after crossing the Socotra Passage as suggested by Rochford (1964) and Shapiro and Meschanov (1991). The time evolution of the particles' cloud in Figs. 15 and S12 show particles advected via the Socotra Passage, eastern Socotra, and flowing northward along the Yemeni–Omani coast; but, no branches emerge in the Somali Basin. Neither the probabilities maps have any indication of multiple branches in this region (Figs. 11, 14 and 19). In the Somali Basin, most particles tend to hug the continental slope in all simulations.

The simulations, instead, revealed a third essential route supplying RSOW to the Somali slope —the Northwest Pathway. In this path, particles follow a slanted anticyclonic circulation centered in the northwest Arabian Sea. The particles are exported via the Gulf's mouth and advected off the Yemeni–Omani coast toward the Gulf of Oman (north of 23° N). They then return southward, offshore in the same area, to the eastern Socotra. From there, they are advected southward to the Somali slope. Hence, none of the GLORYS12-based simulations support the idea that the RSOW is geographically limited south of 17°–18° N in the western boundary as stated in some studies (e.g., Chowdary et al., 2005; Premchand et al., 1986; Rochford, 1964; Sastry and D'Souza, 1972; Shenoi et al., 1993; Varma et al., 1980).

The large anticyclonic cell that forms the Northwest Pathway also appears on the geostrophic circulation map at 1000 dbar from Reid (2003) who suggested that this route brings RSOW northward. A northeastward path off Yemen–Oman also emerged in the simulations by Schmidt et al. (2020). Therefore, the Northwest Pathway seems robust and explain RSOW observations off Yemen–Oman reported in several studies (e.g. Al Saafani and Shenoi, 2007; Beal et al., 2000; Carton et al., 2012; de Marez et al., 2019, 2020). It also explains how six RAFOS floats from the REDSOX experiments resurfaced along the Yemeni coast (Furey et al., 2005; Bower and Furey, 2012). Argo floats trajectories offer additional support for this route off Yemen–Oman and the large-anticyclonic cell.

In the Northwest Pathway, the most frequent transit time is around 2–3 years (Fig. 16), and salinity dilution is moderate (Fig. 23). These timescales may directly impact the mid-depth salinity and oxygen budgets in the northwestern region and contribute to the eastern shift of the ASOMZ (e.g., McCreary et al., 2013), subjects that deserve investigation.

Historically, the path of the RSOW to the eastern Arabian Sea has been poorly understood (e.g., Babu et al., 1980; Beal et al., 2003; Shankar et al., 2005; Shenoi et al., 2005; Varkey et al., 1979; Vimal Kumar et al., 2008; You, 1998). Shankar et al. (2005) proposed two possible routes. The first —northward off Yemen–Oman, westward off Iran–Pakistan, and southward off India —fits well within the Northwest Pathway. The second possibility was an open ocean, cross-basin flow from the western Arabian Sea to India's west coast at its northern end. Although the Lagrangian simulations reveal two open ocean, cross-basin routes, none directly connects the western boundary to the northeastern. One route in the simulations runs from about 18° N in the western boundary to 14° N in the eastern boundary and is part of the Central and Eastern Pathways (there were several examples of Argo floats following a similar path). The other is at about 8° N as part of the Southern Pathway. The cross-basin routes from the Lagrangian simulations also do not support the one proposed earlier by Rochford (1964) from the north of Socotra to India's southern tip. Instead, in the simulations, the Southern Pathway advects particles to India's southern tip at the latitude of 8° N. This cross-basin flow resembles one of the branches proposed by Shapiro and Meschanov (1991). However, it does not originate from a split of the RSOW flow at the Socotra Passage as proposed by the latter authors. Hydrographic measurements around 8° N near 60° E and 73° E (e.g., Beal et al., 2003; He et al., 2020; Stramma et al., 2002) support the existence of the Southern Pathway at this latitude.

From the six identified advective pathways, only two (Eastern and Southern) bring outflow particles to the Arabian Sea's southeastern corner, which explains the low likelihood of outflow particles to be found in this region, as shown in Fig. 11d–f. These pathways together account only for 4% of the total particles. They are long pathways. It takes a couple of decades for particles departing from the Red Sea outflow area to arrive in the Arabian Sea's southeastern corner. As particles have more chance to mix (along isopycnal) with the fresher ambient waters, they lose their salty signature (Figs. 23e–f and S13e–f). This fact makes it hard to identify the RSOW in the T–S space alone.

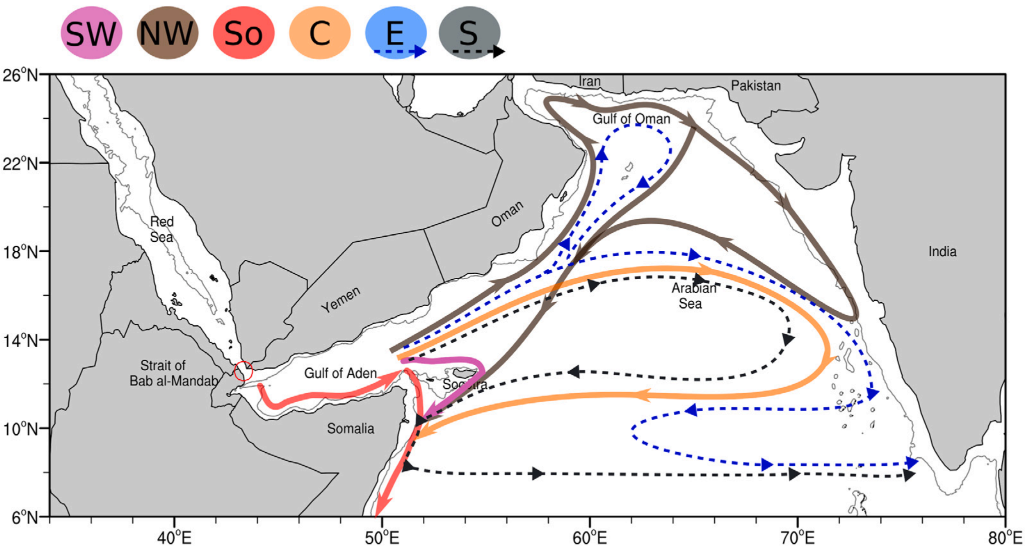

Fig. 25. Main RSOW advective pathways in the Arabian Sea based on isopycnic Lagrangian simulations. Solid curves are used for pathways mostly at upper and core RSOW ($27\sigma_\theta$ and $27.3\sigma_\theta$) and dashed curves for RSOW bottom ($27.6\sigma_\theta$). Pathways displayed are: Southwest Pathway, Northwest Pathway, Socotra Passage Pathway, Central Pathway, Eastern Pathway and Southern Pathway. The gray contour is the 700 m isobath from ETOPO2.

Thus, it is not a surprise that the occurrence of RSOW based on T–S observations in the southeastern Arabian Sea has been debatable in the literature. However, the Lagrangian simulations show that particles originating in the Red Sea outflow area can be advected to India's southern tip. This pathway may explain how RSOW reaches the Bay of Bengal, as reported in Jain et al. (2017).

The pathways carrying particles to the southeastern Arabian Sea are deeper than to the southwestern and are prominent at $27.6\sigma_\theta$ (e.g., Fig. 19, insets). Schmidt et al. (2020) also cite that their interior RSOW pathway to the ASOMZ is more pronounced on the isopycnal surface of $27.4\sigma_\theta$ than $27\sigma_\theta$. These results suggest that the densest RSOW part supplies the eastern side while the western side is by the upper RSOW. These isopycnals correspond to two primary equilibrium levels of the RSOW in the outflow area in the Gulf of Aden (Bower et al., 2000, 2005). Nonetheless, a thorough investigation of the vertical structure of the RSOW pathways is still to be done. For that, the Lagrangian simulations should consider vertical velocities, a limitation of the present study.

In contradiction with Schott and Fischer (2000) that suggested the export of RSOW via the Gulf's mouth is occasional, in all six Lagrangian experiments executed here, the mouth was the main export route out of the Gulf. It was also for the Argo floats deployed within the Gulf. The maximum that Socotra Passage accounted for was 30% of exported particles. Additionally, the export route was via the Gulf's mouth for all pathways except the Socotra. Export via the Gulf's mouth occurred year-round.

The mechanisms (e.g., currents, eddies, waves) behind the six advective pathways described above have not been investigated in the present study. Still, in the Gulf of Aden, it was noticeable that mesoscale eddies dominate the particle trajectories (Fig. 6a) as previously found in RAFOS and Argo observations (Bower and Furey, 2012; Carton et al., 2012). Off Somalia, the trajectories indicate that the southward transport of RSOW is by the Socotra and Somali Undercurrents (Fig. 20a), but the signature of mesoscale eddies also appears in the synthetic trajectories (e.g., Fig. 21a) and Argo floats (Fig. 24). Moreover, the mean transit time was overall lower in EXP-RSOW-SIGMA-93, which was based on more energetic eddy fields than the normal-year simulations. This suggests that mesoscale eddies can help to quickly disperse RSOW to the Arabian Sea interior. In the literature, there is evidence that meso- and sub-mesoscale eddies advect RSOW to the Arabian Sea interior (e.g., Carton et al., 2012; de Marez et al., 2019, 2020), but further investigation is required. A Lagrangian perspective may offer some light on this problem.

Until the present study, the RSOW transit time in the Gulf of Aden and the Arabian Sea was much less known than the pathways. Little information exists in the literature. For instance, Mecking and Warner (1999) used CFCs (chlorofluorocarbons) measurements and a simple box model to estimate the advective timescale of the RSOW in the Gulf of Aden as 2.4–3 years. Bower and Furey (2012) found that most RAFOS floats stayed in the Gulf of Aden for their entire one-year mission. The mean and most frequent transit times estimated from the Lagrangian simulations shown here are of the same order as these few observations.

Also, based on CFCs measurements, Fine et al. (2008) calculated the water-mass age in the Arabian Sea at $27.3\sigma_\theta$ as less than 22 years in the Gulf of Aden to more than 28 years in the northeastern Arabian Sea. However, CFC-based estimations reflect the last time a water parcel was in contact with the atmosphere, which in the case of the RSOW was in the northern Red Sea, not the advective transit times as defined in Section 3.2 (transit times relative to the releasing point, which is the westernmost part of the Gulf of Aden). Nevertheless, taking the difference between the eastern and the western, it would take more than six years for RSOW to arrive in the northeastern from the Gulf. In the Lagrangian simulations, the most frequent time for the particles to reach the northeastern is ten years, which is the same order. More recently, Schmidt et al. (2020) calculated a transit time of 5.2–6.4 years for virtual particles released at 13.04° N–49.04° E, near the mouth of the Gulf of Aden, to reach the ASOMZ at 19° N and 62° –66.6° E.

6. Summary and conclusion

The present study investigated the advective pathways and transit times of virtual particles released in the Red Sea outflow area as a proxy for the poorly understood spreading of the RSOW in the Arabian Sea. It used the Parcels toolbox, a Lagrangian framework, that allowed simulations of tens of thousands of trajectories under different initial conditions within the RSOW layer. The Lagrangian simulations were based on the eddy-rich GLORYS12 reanalysis that merges almost all in-situ (temperature–salinity) and satellite observations collected over the last two decades into the NEMO OGCM. A limitation of the present study was that the Lagrangian simulations did not consider vertical motions. Exploratory experiments using vertical velocities estimated from the continuity equation —native vertical velocity fields are not available in GLORYS12—resulted in few particles sinking to the ocean floor in the Gulf of Aden, which seemed unrealistic. Out of caution, isobaric and isopycnic simulations were used, mainly because the RSOW is known to spread along isopycnals (27–27.6 kg/m^3) over thousands of kilometers in the Indian Ocean (e.g., Beal et al., 2000; L'Hégaret et al., 2021). Although this study did not consider vertical velocity, the statistics presented were based on particles released over the entire RSOW layer, which captures a large fraction of possible pathways, and particles on the isopycnal simulations went up and down in the water column as a result of isopycnic heaving.

Comparisons between GLORYS12 and in-situ observations from the REDSOX experiment (Bower and Furey, 2012; Furey et al., 2005) in the Gulf of Aden show that GLORYS12 reproduces relatively well the statistical properties of the Gulf's mid-depth circulation, a region dominated by mesoscale turbulence (including the RSOW layer). These comparisons corroborate the quality of GLORYS12 velocity fields used for the Lagrangian simulations. However, the comparisons also pointed out a dilution of the modeled RSOW in the western Gulf, likely due to GLORYS12 excessive numerical mixing over the Strait of Bab al-Mandab and the relaxation to the climatology applied to mitigate it (Lellouche et al., 2018). Nevertheless, the fresher and colder RSOW properties west of 46° E in GLORYS12 do not appear to have affected the Arabian Sea mid-depth circulation and water mass properties. The RSOW T–S properties in the reanalysis are close to the observations near the Gulf's mouth.

Furthermore, at the Strait of Bab al-Mandab, the RSOW volume transport in GLORYS is in the same range and seasonality as observations (Murray and Johns, 1997). The vertical structure of velocity at the strait (two-layer system in winter and three-layer summer) is also reproduced by the reanalysis, and the RSOW export from the Gulf of Aden to the Arabian Sea in GLORYS12 is of the same order as estimated by Han and McCreary (2001). Compared with other climatologies, GLORYS12 is more consistent with the RSOW literature.

A quantitative analysis of the virtual particles confirms the previous results of Beal et al. (2000) based on in situ observations of temperature and salinity, i.e., the main RSOW advective route out of the Arabian Sea is off Somalia. More importantly, it revealed robust connectivity of the RSOW to the Arabian Sea interior, which is supported by Argo trajectories at mid-depth. Many particles follow interior pathways before returning to the Somali basin to be exported out of the Arabian Sea. The fact that particles have long trajectories in the interior increases the potential of RSOW mixing with the fresher and oxygen-poor Arabian Sea ambient waters, losing its spiciness and oxygen. Thus, these differences in pathways may have profound implications for the salt and oxygen budgets in the Arabian Sea and beyond since the RSOW is also part of the global overturning circulation and exported out of the Indian Ocean via the Agulhas Current (Beal et al., 2000; Durgadoo et al., 2017).

This study can be seen as a baseline for future investigations. The focus here was on preferred pathways and seasonal variability. The next steps are to evaluate the dilution of RSOW along the ARGO trajectories identified in Fig. 24 and understand the interannual variability of the pathways and the RSOW export out of the Gulf of Aden and how these affect the mid-depth salinity in the Arabian Sea. There is observational evidence that the intermediate layer in the Arabian Sea is becoming saltier (e.g., Durack and Wijffels, 2010; Helm et al., 2010), and the RSOW may be a contributor to that. Since the Indian Ocean circulation is fundamentally affected by the Indian Ocean Dipole and El Niño-Southern Oscillation (Schott et al., 2009), substantial interannual variability of RSOW export out of the Gulf of Aden is expected. Further investigations are also crucial to understanding the mechanism behind the identified advective pathways (e.g., currents, eddies, and waves).

Acknowledgments

I would like to thank the four anonymous reviewers who provided valuable comments that improved the present paper, particularly the suggestion to look at the Argo database. I am grateful to Amy Bower and Heather Furey for the REDSOX data and questions that inspired many of the avenues I took in this study. Thanks to Sijia Zou and Thomas Meunier for all suggestions during Bower's lab group meetings that help better interpret the simulation results and Marcio Vianna for patiently reading this long article and suggesting changes to improve its readability. I thank the E. U. Copernicus Marine Environment Monitoring Service project for the GLORYS12 reanalysis data, freely available at their portal. The Coriolis project for the Argo dataset. These data were collected and made freely available by the International Argo Project and the national programs that contribute to it (http://www.argo.net). Also, the OceanParcels project for making Parcels available, an open-source and easy-to-use Python toolbox. Without GLORYS12 data and Parcels, this study would not be possible. RAFOS float data are available at the AOML website https://www.aoml.noaa.gov/phod/float_traj/. I also wish to acknowledge the use of the NCL program (https://doi.org/10.5065/D6WD3XH5) for analysis and graphics in this paper. This research was supported by the National Science Foundation (NSF) grant number OCE-1736823.

Appendix A. Supplementary data

Supplementary material related to this article can be found online at https://doi.org/10.1016/j.pocean.2021.102697.

References

Al Saafani, M., Shenoi, S., 2007. Water masses in the Gulf of Aden. J. Oceanogr. 63, 1–14. http://dx.doi.org/10.1007/s10872-007-0001-1.

Al Saafani, M.A., Shenoi, S.S.C., Shankar, D., Aparna, M., Kurian, J., Durand, F., Vinayachandran, P.N., 2007. Westward movement of eddies into the Gulf of Aden from the Arabian Sea. J. Geophys. Res. 112, C11004. http://dx.doi.org/10.1029/2006JC004020.

Artana, C., Ferrari, R., Bricaud, C., Lellouche, J.M., Garric, G., Sennéchael, N., Lee, J., Park, Y.H., Provost, C., 2019. Twenty-five years of mercator ocean reanalysis GLORYS12 at Drake passage: velocity assessment and total volume transport. Adv. Space Res. http://dx.doi.org/10.1016/j.asr.2019.11.033.

Babu, V.R., Varkey, M.J., Das, V.K., Gouveia, A.D., 1980. Water masses and general hydrography along the west coast of India during early march. Indian J. Mar. Sci. 9, 82–89, http://nopr.niscair.res.in/handle/123456789/39186.

Beal, L.M., Chereskin, T.K., Bryden, H.L., Ffield, A., 2003. Variability of water properties, heat and salt fluxes in the Arabian Sea, between the onset and wane of the 1995 southwest monsoon. Deep-Sea Res. II 50, 2049–2075. http://dx.doi.org/10.1016/S0967-0645(03)00045-6.

Beal, L.M., Donohue, K.A., 2013. The Great Whirl: Observations of its seasonal development and interannual variability. J. Geophys. Res. Oceans 118, 1–13. http://dx.doi.org/10.1029/2012JC008198.

Beal, L.M., Ffield, A., Gordon, A.L., 2000. Spreading of Red Sea overflow waters in the Indian Ocean. J. Geophys. Res. 105, 8549–8564. http://dx.doi.org/10.1029/1999JC900306.

Bower, A.S., Fratantoni, D.M., Johns, W.E., Peters, H., 2002. Gulf of Aden eddies and their impact on Red Sea Water. Geophys. Res. Lett. 29, 2025. http://dx.doi.org/10.1029/2002GL015342.

Bower, A.S., Furey, H.H., 2012. Mesoscale eddies in the Gulf of Aden and their impact on the spreading of Red Sea Outflow Water. Progr. Oceanogr. 96, 14–39. http://dx.doi.org/10.1016/j.pocean.2011.09.003.

Bower, A.S., Hunt, H.D., Price, J.F., 2000. Character and dynamics of the Red Sea and Persian Gulf outflows. J. Geophys. Res. 105, 6387–6414. http://dx.doi.org/10.1029/1999JC900297.

Bower, A.S., Johns, W.E., Fratantoni, D.M., Peters, H., 2005. Equilibration and circulation of Red Sea outflow water in the western Gulf of Aden. J. Phys. Oceanogr. 35, 1963–1985. http://dx.doi.org/10.1175/JPO2787.1.

Bruce, J.G., Volkmann, G.H., 1969. Some measurements of current off the Somali coast during the northeast monsoon. J. Geophys. Res. 74, 1958–1967. http://dx.doi.org/10.1029/JB074i008p01958.

Burkholder, K.C., Lozier, S.M., 2011. Mid-depth Lagrangian pathways in the North Atlantic and their impact on the salinity of the eastern subpolar gyre. Deep-Sea Res. I 58, 1196–1204. http://dx.doi.org/10.1016/j.dsr.2011.08.007.

Carton, X., L'Hegaret, P., Baraille, R., 2012. Mesoscale variability of water masses in the Arabian Sea as revealed by ARGO floats. Ocean Sci. 8, 227–248. http://dx.doi.org/10.5194/os-8-227-2012.

Cedarholm, E.R., Rypina, I.I., Macdonald, A.M., Yoshida, S., 2019. Investigating subsurface pathways of Fukushima cesium in the northwest Pacific. Geophys. Res. Lett. 46, 6821–6829. http://dx.doi.org/10.1029/2019GL082500.

Chowdary, J.S., Gnanaseelan, C., Thompson, B., Salvekar, P.S., 2005. Water mass properties and transports in the Arabian Sea from Argo observations. J. Atmos. Ocean. Sci. 10, 235–260. http://dx.doi.org/10.1080/17417530600752825.

Clowes, A.J., Deacon, G.E.R., 1935. The deep-water circulation of the Indian ocean. Nature 136, 936–938. http://dx.doi.org/10.1038/136936a0.

Colombo, P., Barnier, B., Penduff, T., Chanut, J., Deshayes, J., Molines, J.M., Le Sommer, J., Verezemskaya, P., Gulev, S., Treguier, A.M., 2020. Representation of the Denmark strait overflow in a z-coordinate eddying configuration of the NEMO (v3.6) ocean model: resolution and parameter impacts. Geosci. Model Dev. 13, 3347–3371. http://dx.doi.org/10.5194/gmd-13-3347-2020.

de Marez, C., Carton, X., Corréard, S., L'Hégaret, P., Morvan, M., 2020. Observations of a deep submesoscale cyclonic vortex in the Arabian Sea. Geophys. Res. Lett. 47, http://dx.doi.org/10.1029/2020GL087881, e2020GL087881.

de Marez, C., L'Hégaret, P., Morvan, M., Carton, X., 2019. On the 3D structure of eddies in the Arabian Sea. Deep-Sea Res. I 150, 103057. http://dx.doi.org/10.1016/j.dsr.2019.06.003.

Delandmeter, P., van Sebille, E., 2019. The Parcels v2.0 Lagrangian framework: new field interpolation schemes. Geosci. Model Dev. 12, 3571–3584. http://dx.doi.org/10.5194/gmd-12-3571-2019.

Drévillon, M., Régnier, C., Lellouche, J.M., Garric, G., Bricaud, C., Hernandez, O., 2018. Quality Information Document for Global Ocean Reanalysis Products GLOBAL-REANALYSIS-PHY-001-030. Technical Report, EU Copernicus Marine Service.

Durack, P.J., Wijffels, S.E., 2010. Fifty-year trends in global ocean salinities and their relationship to broad-scale warming. J. Clim. 23, 4342–4362. http://dx.doi.org/10.1175/2010JCLI3377.1.

Durgadoo, J.V., Ruhs, S., Biastoch, A., Boning, C.W.B., 2017. Indian ocean sources of Agulhas leakage. J. Geophys. Res. Oceans 122, 3481–3499. http://dx.doi.org/10.1002/2016JC012676.

Esenkov, O.E., Olson, D.B., 2002. A numerical study of the Somali coastal undercurrents. Deep-Sea Res. II 49, 1253–1277. http://dx.doi.org/10.1016/S0967-0645(01)00152-7.

Fernandez, E., Lellouche, J.M., 2018. Product User Manual for the Global Ocean Physical Reanalysis Product GLOBAL-REANALYSIS- PHY-001-030. Technical Report, EU Copernicus Marine Service.

Fine, R.A., Smethie, W.M., Bullister, J., Rhein, M., Min, D.H., Warner, M.J., Poisson, A., Weiss, R.F., 2008. Decadal ventilation and mixing of Indian ocean waters. Deep-Sea Res. I 55, 20–37. http://dx.doi.org/10.1016/j.dsr.2007.doi:10.002.

Fischer, J., Schott, F., Stramma, L., 1996. Currents and transports of the Great Whirl-Socotra Gyre system during the summer monsoon, August 1993. J. Geophys. Res. 101, 3573–3587. http://dx.doi.org/10.1029/95JC03617.

Forget, G., Campin, J.M., Heimbach, P., Hill, C.N., Ponte, R.M., Wunsch, C., 2015. ECCO version 4: an integrated framework for non-linear inverse modeling and global ocean state estimation. Geosci. Model Dev. 8, 3071–3104. http://dx.doi.org/10.5194/gmd-8-3071-2015.

Fox-Kemper, B., Alistair, A., BÃűning, C.W., Chassignet, E.P., Curchitser, E., Danabasoglu, G., Eden, C., England, M.H., Gerdes, R., Greatbatch, R.J., Griffies, S.M., Hallberg, R.W., Hanert, E., Heimbach, P., Hewitt, H.T., Hill, C.N., Komuro, Y., Legg, S., L. Sommer, J., Masina, S., Marsland, S.J., Penny, S.G., Qiao, F., Ringler, T.D., Treguier, A.M., Tsujino, H., Uotila, P., Yeager, S.G., 2019. Challenges and prospects in ocean circulation models. Front. Mar. Sci. 6 (65), http://dx.doi.org/10.3389/fmars.2019.00065.

Fratantoni, D.M., Bower, A.S., Johns, W.E., Peters, H., 2006. Somali current rings in the eastern Gulf of Aden. J. Geophys. Res. 111, C09039. http://dx.doi.org/10.1029/2005JC003338.

Furey, H.H., Bower, A.S., Fratantoni, D.M., 2005. Red Sea Outflow Experiment (REDSOX): DLD2 RAFOS Float Data Report, February 2001-March 2003. Technical Report, Woods Hole Oceanographic Institution, Woods Hole, Mass.

Gamsakhurdiya, G.R., Meschanov, S.L., Shapiro, G.K., 1991. Seasonal variations in the distribution of Red Sea waters in the northwestern Indian Ocean. Oceanology 31, 32–37.

Gary, S.F., Lozier, M.S., Kwon, Y.O., Park, J.J., 2014. The fate of North Atlantic subtropical mode water in the FLAME models. J. Phys. Oceanogr. 44, 1354–1371. http://dx.doi.org/10.1175/JPO-D-13-0202.1.

Han, W., McCreary, J., 2001. Modeling salinity distributions in the Indian ocean. J. Geophys. Res. 206, 859–877. http://dx.doi.org/10.1029/2000JC000316.

He, H., Wang, Y., Han, X., Wei, Y., Lin, P., Qiu, Z., Wang, Y., 2020. Anomalous distribution of distinctive water masses over the Carlsberg Ridge in May 2012. Ocean Sci. 16, 895–906. http://dx.doi.org/10.5194/os-16-895-2020.

Helm, K.P., Bindoff, N.L., Church, J.A., 2010. Changes in the global hydrological-cycle inferred from ocean salinity. Geophys. Res. Lett. 37, L18701. http://dx.doi.org/10.1029/2010GL044222.

Ilicak, M., Özgökmena, T.M., Johns, W.E., 2011. How does the Red Sea outflow water interact with Gulf of Aden eddies? Ocean Model 36, 133–148.

Ilicak, M., Özgökmena, T.M., Peters, H., Baumert, H.Z., Iskandarani, M., 2008. Very large eddy simulation of the Red Sea overflow. Ocean Model 20, 183–206. http://dx.doi.org/10.1016/j.ocemod.2007.08.002.

IOC, SCOR, IAPSO, 2010. The international thermodynamic equation of seawater - 2010: Calculation and use of thermodynamic properties. In: Intergovernmental Oceanographic Commission, Manuals and Guides 56. UNESCO, p. 196.

Jain, V., Shankar, D., Vinayachandran, P.N., Kankonkar, A., Chatterjee, A., Amol, P., Almeida, A.M., Michael, G.S., Mukherjee, A., Chatterjee, M., Fernandes, R., Luis, R., Kamble, A., Hegde, A.K., Chatterjee, S., Das, U., Neema, C.P., 2017. Evidence for the existence of Persian Gulf Water and Red Sea Water in the Bay of Bengal. Clim. Dyn. 48, 3207–3226. http://dx.doi.org/10.1007/s00382-016-3259-4.

Lange, M., van Sebille, E., 2017. Parcels v0.9: prototyping a Lagrangian ocean analysis framework for the petascale age. Geosci. Model Dev. 10, 4175–4186. http://dx.doi.org/10.5194/gmd-10-4175-2017.

Lankhorst, M., Zenk, W., 2006. Lagrangian observations of the middepth and deep velocity fields of the Northeastern Atlantic Ocean. J. Phys. Oceanogr. 36, 43–63. http://dx.doi.org/10.1175/JPO2869.1.

Large, W., Yeager, S., 2004. Diurnal to decadal global forcing for ocean and sea-ice models: the datasets and flux climatologies. Technical Report, NCAR Technical Note: NCAR/TN-460 + STR, CGD Division of the National Centre for Atmospheric Research.

Large, W., Yeager, S., 2009. The global climatology of an interannually varying air-sea flux data set. Clim. Dynam. 33, 341–364. http://dx.doi.org/10.1007/s00382-008-0441-3.

Legg, S., Briegleb, B., Chang, Y., Chassignet, E.P., Danabasoglu, G., Ezer, T., Gordon, A.L., Griffies, S., Hallberg, R., Jackson, L., Large, W., Özgökmen, T.M., abd Peters, H., Price, J., Riemenschneider, U., Wu, W., Xu, X., Yang, J., 2009. Improving oceanic overflow representation in climate models: The gravity current entrainment climate process team. Bull. Am. Meteorol. Soc. 90, 657–670. http://dx.doi.org/10.1175/2008BAMS2667.1.

Lellouche, J.M., Greiner, E., Le Galloudec, O., Garric, G., Regnier, C., Drevillon, M., Benkiran, M., Testut, C.E., Bourdalle-Badie, R., Gasparin, F., Hernandez, O., Levier, B., Drillet, Y., Remy, E., Le Traon, P.Y., 2018. Recent updates to the Copernicus Marine Service global ocean monitoring and forecasting real-time $1/12^{o}$ high-resolution system. Ocean Sci 14, 1093–1126. http://dx.doi.org/10.5194/os-14-1093-2018.

L'Hégaret, P., d. Marez, C., Morvan, M., Meunier, T., Carton, X., 2021. Spreading and vertical structure of the Persian Gulf and Red Sea outflows in the Northwestern Indian Ocean. J. Geophys. Res. Oceans 126, http://dx.doi.org/10.1029/2019JC015983, e2019JC015983.

Lozier, S.M., Gary, S.F., Bower, A.S., 2012. Simulated pathways of the overflow waters in the North Atlantic: Subpolar to subtropical export. Deep-Sea Res. II 85, 147–153. http://dx.doi.org/10.1016/j.dsr2.2012.07.037.

Marzocchi, A., Hirschi, J.J.M., Holliday, N.P., Cunningham, S.A., Blaker, A.T., Coward, A.C., 2015. The North Atlantic subpolar circulation in an eddy-resolving global ocean model. J. Mar. Syst. 142, 126–143. http://dx.doi.org/10.1016/j.jmarsys.2014.doi:10.007.

Matt, S., Johns, W.E., 2007. Transport and entrainment in the Red Sea outflow plume. J. Phys. Oceanogr. 37, 819–836. http://dx.doi.org/10.1175/JPO2993.1.

McCreary, J.P., Yua, A., Hood, R.R., Vinaychandranc, P.N., Furue, R., Ishida, A., Richards, K.J., 2013. Dynamics of the Indian-ocean oxygen minimum zones. Progr. Oceanogr. 112–113, 15–37. http://dx.doi.org/10.1016/j.pocean.2013.03.002.

McDougall, T.J., Barker, P.M., 2011. Getting started with TEOS-10 and the Gibbs seawater (GSW) oceanographic toolbox. ISBN: 978-0-646-55621-5, p. 28, SCOR/IAPSO WG127.

Mecking, S., Warner, M.J., 1999. Ventilation of Red Sea Water with respect to chlorofluorocarbons. J. Geophys. Res. 104, 11087–11097. http://dx.doi.org/10.1029/1999JC900027.

Menezes, V.V., Farrar, J., Bower, A., 2019. Evaporative implications of dry-air outbreaks over the northern Red Sea. J. Geophys. Res. Atmos 124, 4829–4861. http://dx.doi.org/10.1029/2018JD028853.

Meschanov, S.L., Shapiro, G.I., 1998. A young lens of Red Sea Water in the Arabian Sea. Deep-Sea Res. I 45, 1–13. http://dx.doi.org/10.1016/S0967-0637(97)00018-6.

Morvan, M., Carton, X., Corréard, S., Baraille, R., 2020. Submesoscale dynamics in the Gulf of Aden and the Gulf of Oman. Fluids 5, 146. http://dx.doi.org/10.3390/fluids5030146.

Murray, S.P., Johns, W., 1997. Direct observations of seasonal exchange through the Bab el Mandab Strait. Geophys. Res. Lett. 24, 2557–2560. http://dx.doi.org/10.1029/97GL02741.

NGDC, National Geophysical Data Center, 2006. 2-Minute Gridded Global Relief Data (ETOPO2) V2. National Geophysical Data Center, NOAA, http://dx.doi.org/10.7289/V5J1012Q.

Olson, D.B., Hitchcock, G.L., Fine, R.A., Warren, B.A., 1993. Maintenance of the low-oxygen layer in the central Arabian Sea. Deep-Sea Res. II 40, 673–685. http://dx.doi.org/10.1016/09670645(93)90051-N.

Onink, V., Wichmann, D., Delandmeter, P., van Sebille, E., 2019. The role of Ekman currents, geostrophy, and stokes drift in the accumulation of floating microplastic. J. Geophys. Res. Oceans 124, 1474–1490. http://dx.doi.org/10.1029/2018JC014547.

Pilo, G.S., Oke, P.R., Coleman, R., Rykova, T., Ridgway, K., 2018. Impact of data assimilation on vertical velocities in an eddy resolving ocean model. Ocean Model. 131, 71–85. http://dx.doi.org/10.1016/j.ocemod.2018.09.003.

Premchand, K., Sastry, J.S., Murty, C.S., 1986. Watermass structure in the western Indian ocean-part III: The spreading and transformation of Red Sea watermass. Mausam 31, 317–324.

Quadfasel, D., Schott, F., 1982. Water-mass distributions at intermediate layers off the Somali coast during the onset of the southwest monsoon, 1979. J. Phys. Oceanogr. 12, 1358–1372. http://dx.doi.org/10.1175/1520-0485(1982)012 < 1358:WMDAIL > 2.0.CO;2.

Quadfasel, D.R., Schott, F., 1983. Southward subsurface flow below the Somali current. J. Geophys. Res. 88, 5973–5979. http://dx.doi.org/10.1029/JC088iC10p05973.

Reid, J.L., 2003. On the total geostrophic circulation of the Indian Ocean: flow patterns, tracers, and transports. Progr. Oceanogr. 56, 137–186. http://dx.doi.org/10.1016/S0079-6611(02)00141-6.

Rochford, D.J., 1964. Salinity maxima in the upper 1000 metres of the north Indian ocean. Aust. J. Mar. Freshw. Res. 15, 1–24. http://dx.doi.org/10.1071/MF9640001.

Rossby, T., Dorson, D., Fontaine, J., 1986. The RAFOS system. J. Atmos. Ocean. Technol. 3, 672–679. http://dx.doi.org/10.1175/1520-0426(1986)003 < 0672:TRS > 2.0.CO;2.

Saberi, A., Haine, T.W.N., Gelderloos, R., Femke de Jong, M., Furey, H., Bower, A., 2020. Lagrangian perspective on the origins of Denmark strait overflow. J. Phys. Oceanogr. 50, 2393–2414. http://dx.doi.org/10.1175/JPO-D-19-02doi:10.1.

Sarma, V.V.S.S, 2002. An evaluation of physical and biogeochemical processes regulating perennial suboxic conditions in the water column of the Arabian Sea. Global Biogeochem. Cycles 16, 1082. http://dx.doi.org/10.1029/2001GB001461.

Sasaki, H., Nonaka, M., Masumoto, Y., Sasai, Y., Uehara, H., Sakuma, H., 2008. An eddy-resolving hindcast simulation of the quasiglobal ocean from 1950 to 2003 on the Earth Simulator. In: Hamilton, K., Ohfuchi, W. (Eds.), High Resolution Numerical Modelling of the Atmosphere and Ocean. Springer, pp. 157–185.

Sastry, J.S., D'Souza, R.S., 1972. Oceanography of the Arabian Sea during southwest monsoon season, Part III: salinity. Ind. J. Meteorol. Geophys. 23, 479–490.

Schmidt, H., Czeschel, R., Visbeck, M., 2020. Seasonal variability of the circulation in the Arabian Sea at intermediate depth and its link to the Oxygen Minimum Zone. Ocean Sci. Discuss. http://dx.doi.org/10.5194/os-2020-9, in review.

Schott, F.A., Fischer, J., 2000. Winter monsoon circulation of the northern Arabian Sea and Somali Current. J. Geophys. Res. 105, 6359–6376. http://dx.doi.org/10.1029/1999JC900312.

Schott, F., McCreary, J.P., 2001. The monsoon circulation of the Indian ocean. Progr. Oceanogr. 51, 1–123. http://dx.doi.org/10.1016/S0079-6611(01)00083-0.

Schott, F.A., Xie, S.P., McCrear Jr., J.P., 2009. Indian ocean circulation and climate variability. Rev. Geophys. 47, RG1002. http://dx.doi.org/10.1029/2007RG000245.

Shankar, D., Shenoi, S., Nayak, R., Vinayachandran, P.N., Nampoothiri, G., Almeida, A.M., Michael, G.S., Ramesh Kumar, M.R., Sundar, D., Sreejith, O.P., 2005. Hydrography of the eastern Arabian Sea during summer monsoon 2002. J. Earth Syst. Sci. 114, 459–474. http://dx.doi.org/10.1007/BF02702023.

Shapiro, G.I., Meschanov, S.L., 1991. Distribution and spreading of Red Sea Water and salt lens formation in the northwest Indian Ocean. Deep-Sea Res. A 38, 21–34. http://dx.doi.org/10.1016/0198-0149(91)90052-H.

Shapiro, G.L., Meschanov, S.L., Polonsky, A.B., 1994. Red sea water lens formation in Arabian Sea. Oceanology 36, 24–31.

Sheehan, P.M.F., Webber, B.G.M., SanchezâĂŘFranks, A., Matthews, A.J., Heywood, K.J., Vinayachandran, P.N., 2020. Injection of oxygenated Persian Gulf Water into the southern Bay of Bengal. Geophys. Res. Lett. 47, http://dx.doi.org/10.1029/2020GL087773, e2020GL087773.

Shenoi, S.S.C., Shankar, D., Michael, G.S., Kurian, J., Varma, K.K., Rames. Kumar, M.R., Almeida, A.M., Unnikrishnan, A.S., Fernandes, W., Barreto, N., Gnanaseelan, C., Mathew, R., Praju, K.V., Mahale, V., 2005. Hydrography and water masses in the southeastern Arabian Sea during March-June 2003. J. Earth Syst. Sci. 114, 475–491. http://dx.doi.org/10.1007/BF02702024.

Shenoi, S., Shetye, S., Gouveia, A., Michael, G., 1993. Salinity extrema in the Arabian Sea. Geologisch-Palaontologisches Inst, Hamburg. 37–49.

Sofianos, S.S., Johns, W.E., 2015. Water mass formation, overturning circulation, and the exchange of the Red Sea with the adjacent basins. In: Rasul, N.M.A., Stewart, I.C.F. (Eds.), The Red Sea. Springer Berlin Heidelberg, pp. 343–354. http://dx.doi.org/10.1007/978-3-662-45201-1_20.

Sofianos, S.S., Johns, W.E., Murray, S.P., 2002. Heat and freshwater budgets in the Red Sea from direct observations at Bab el Mandeb. Deep-Sea Res. II 49, 1323–1340. http://dx.doi.org/10.1016/S0967-0645(01)00164-3.

Sparrow, M., Boebel, O., Zervakis, V., Zenk, W., Cantos-Figuerola, A., Gould, W.J., 2002. Two circulation regimes of the Mediterranean outflow revealed by Lagrangian measurements. J. Phys. Oceanogr. 32, 1322–1330. http://dx.doi.org/10.1175/1520-0485(2002)032 < 1322:TCROTM > 2.0.CO;2.

Sterl, M.F., Delandmeter, P., van Sebille, E., 2020. Influence of barotropic tidal currents on transport and accumulation of floating microplastics in the globalopen ocean. J. Geophys. Res. Oceans 125, http://dx.doi.org/10.1029/2019JC015583, e2019JC015583.

Stramma, L., Brandt, P., Schott, F., Quadfasel, D., Fischer, J., 2002. Winter and summer monsoon water mass, heat and freshwater transport changes in the Arabian Sea near 8^o n. Deep-Sea Res. II 49, 1173–1195. http://dx.doi.org/10.1016/S0967-0645(01)00169-2.

Swallow, J.C., Bruce, J.G., 1966. Current measurements off the Somali coast during the southwest monsoon of 1964. Deep-Sea Res. Oceanogr. Abstr. 13, 861–888. http://dx.doi.org/10.1016/0011-7471(76)90908-6.

van Sebille, E., Biastoch, A., van Leeuween, P.J., d. Ruijter, W.P.M., 2009. A weaker agulhas current leads to more agulhas leakage. Geophys. Res. Lett. 36, http://dx.doi.org/10.1029/2008GL036614.

van Sebille, E., England, M.H., Zika, J.D., Sloyan, B.M., 2012. Tasman leakage in a fine-resolution ocean model. Geophys. Res. Lett. 39, L06601. http://dx.doi.org/10.1029/2012GL051004.

van Sebille, E., Griffies, E.S.M., Abernathey, R., Adams, T.P., Berloff, P., et al., 2018. Lagrangian ocean analysis: Fundamentals and practices. Ocean Model 121, 49–75. http://dx.doi.org/10.1016/j.ocemod.2017.11.008.

Varkey, M.J., Das, V., RamaRaju, D., 1979. Physical characteristics of the Laccadive Sea (Lakshadweep). Indian J. Mar. Sci 8, 203–210.

Varma, K.K., Kesavadas, V., Gouveia, A.D., 1980. Thermohaline structure & watermasses in the Northern Arabian Sea during february-april. Ind. J. Mar. Sci. 9, 148–155.

Vimal Kumar, K.G., Dinesh Kumar, P.K., Smitha, B.R., Habeeb Rahman, H., Josia, J., Muraleedharan, K.R., Sanjeevan, V.N., Achuthankutty, C.T., 2008. Hydrographic characterization of southeast Arabian Sea during the wane of southwest monsoon and spring intermonsoon. Environ. Monit. Assess 143, 231–247. http://dx.doi.org/10.1007/s10661-007-9863-3.

Wang, Y., Raitsos, E.D., Krokos, G., Gittings, J.A., Zhan, P., Hoteit, I., 2019. Physical connectivity simulations reveal dynamic linkages between coral reefs in the southern Red Sea and the Indian Ocean. Sci. Rep. 9, 16598. http://dx.doi.org/10.1038/s41598-019-53126-0.

Warren, B., Stommel, H., Swallow, J.C., 1966. Water masses and patterns of flow in the Somali Basin during the southwest monsoon of 1964. Deep-Sea Res. Oceanogr. Abstr. 13, 825–860. http://dx.doi.org/10.1016/0011-7471(76)90907-4.

Wooding, C.M., Furey, H.H., Pacheco, M.A., 2005. RAFOS Float Processing at Woods Hole Oceanographic Institution. Technical Report, Woods Hole Oceanographic Institution, Woods Hole, Mass.

Wyrtki, K., 1971. Oceanographic Atlas of the International Indian Ocean Expedition. U.S. Govt. Printing Office, Washington, D.C.

You, Y., 1998. Intermediate water circulation and ventilation of the Indian ocean derived from water-mass contributions. J. Mar. Res. 56, 1029–1067. http://dx.doi.org/10.1357/002224098765173455.

Zou, S., Bower, A., Furey, H., Lozier, M.S., Xu, X., 2020. Redrawing the Iceland-Scotland Overflow Water pathways in the North Atlantic. Nature Commun. 11, 1890. http://dx.doi.org/10.1038/s41467-020-15513-4.

Zou, S., Lozier, S., Zenk, W., Bower, A., Johns, W., 2017. Observed and modeled pathways of the Iceland Scotland Overflow Water in the eastern North Atlantic. Prog. Oceanogr. 159, 211–222. http://dx.doi.org/10.1016/j.pocean.2017.doi:10.003.

Zweng, M.M., Reagan, J.R., Seidov, D., Boyer, T.P., Locarnini, R.A., Garcia, H.E., Mishonov, A.V., Baranova, O.K., Weathers, K., Paver, C.R., Smolyar, I., 2018. World Ocean Atlas 2018, Volume 2: Salinity. Technical Report, A. Mishonov Technical Ed. NOAA Atlas NESDIS 82.